Spin-Orbit effect in ferrimagnetic thin film

Thai Ha Pham

THÈSE

Pour l'obtention du titre de:

Docteur de l'Université de Lorraine

Spécialité : *Physique*

Présentée par :

Thai Ha PHAM

Spin-Orbit effect in ferrimagnetic thin film

Thèse soutenue publiquement le 5 Mai 2020 à Nancy devant le jury suivant:

Mme Liza Herrera Diez	Chargée de Recherche, C2N Paris Saclay	Rapportrice
M. Dafiné Ravélosona	Directeur de recherche, C2N Paris Saclay	Rapporteur
Mme Stefania Pizzini	Directrice de Recherche, Institut Néel (CNRS & Université Grenoble Alpes)	Examinatrice
M. Jean Marie George	Directeur de recherche, UMR CNRS-Thales	Examinateur
M. Juan-Carlos ROJAS-SÁNCHEZ	Chargé de recherche, Université de Lorraine	Co-directeur de thèse
M. Stéphane MANGIN	Professeur, Université de Lorraine	Directeur de thèse

Institut Jean Lamour
Université de Lorraine
C2MP - Chimie Mécanique matériaux physique
Nanomagnetism and Spintronics team

Table of contents

Chapter I - Basics of magnetism and spin orbit torque

1.1 Origin of magnetization 15
1.2 Magnetic interactions 16
1.2a) Zeeman interaction 16
1.2b) Dipolar interaction 16
1.2c) Magnetocrystalline and effective anisotropy 18
1.2d) Exchange interaction 19
1.2e) DMI interaction 19
1.3 Magnetic orders 20
1.4 Spintronics 22
1.5 Spin Hall effect (SHE) - Spin Orbit Torque (SOT) 27
1.5.1 Spin Hall effect (SHE) 27
1.5.2 Mechanism of the SHE 28
1.5.3 Efficiency of SHE 29
1.5.4 Spin Orbit Torque 30
1.5.4 Damping-like (DL) and field-like (FL) torques 31
1.6 All Optical Switching 32
References 34

Chapter II - Experimental methods and samples

2.1 Thin film deposition by DC magnetron sputtering 40
2.2 Vibrating Sample Magnetometry (VSM) 43
2.3 Lithography process 44
2.4 Magneto-transport (spin-orbit torque) setup 52

Chapter III - Spin-orbit torque induced switching in ferrimagnetic alloys: Experiments and modeling

3.1 Introduction 57
3.2 Samples and magnetic properties 58
3.3 Theoretical model 61
3.4 Results of transport measurements 65
3.5 Analytical model 69
3.6 Conclusion 70
References 72

Chapter IV - The effect of temperature on magnetization switching by spin-orbit torque in metal/ferrimagnetic system

4.1 Introduction 76
4.2 Samples and magnetic properties 77
4.2.1 Magnetic compensation point x_{Mcomp} 79
4.2.2 Compensation temperature T_{Mcomp} 80
4.2.3 Angular momentum compensation temperature T_{Acomp} 82
4.2.4 Field - induced magnetization switching 84
4.2.5 Determination of Hall angle θ_{AHE} in Co_xTb_{1-x} (3.5nm) 85
4.3 Current - induced spin orbit torque switching 88
4.4 Characteristic temperatures of switching 93
4.5 T-x switching phase diagram 99
4.6 Conclusions 102
References 104

Acknowledgements

I would like to express my deep and sincere gratitude to my research supervisors, Prof. Stéphan Mangin, Professor at Université de Lorraine and Dr. Juan Carlos Rojas Sánchez, Research Scientist at Institut Jean Lamour CNRS. Deep from my heart, I am thankful for their invaluable guidance throughout this research. My completion of this work could not have been accomplished without the great support from them. I am greatful for their patience, motivation and encouragement during my PhD journey.

I would like to thank my PhD committee Mme. Liza Herrera Diez, M. Dafiné Ravélosona, Mme. Stefania Pizzini, M. Jean Marie George for accepting to be members of the jury. It is my pleasure to present my thesis to them.

I would like to thank my colleagues for their big support during my years in Nancy. I am thankful to Laurent Badie, Crosby Chang and Stéphane Suire who taught me a lot of techniques and always support me with technical problems. I would like to thank professor Michel Hehn and Je Soong Geun who helped me a lot in the project.

I would like to thank my fellow lab mates - my friends in Nanomagnetism and Spintronics group who make my time in Nancy so joyful and memorable. To Thibaud and Huyền, I cannot express enough thanks to you for all your help.

I am extremely grateful to my special teacher for many years caring and continuing support since the first day I came to France. She makes me get a new perspective on the world around, have re-awaken moments about the beauty of life and want to strive for better.

I would like to thank my parents, my husband and my dear little sister. When the time got rough, their sleepless nights discussions to solve problems and their encouragements gave me strength.

Résumé

Introduction

Dans l'électronique conventionnelle, le fonctionnement des dispositifs repose sur les propriétés essentielles de l'électron, sa charge et sa marche. L'électron possède également une propriété supplémentaire : le moment cinétique de spin. L'électronique de spin est donc le domaine qui étudie spécifiquement les propriétés de spin ce qui donne un nouveau degré de liberté pour les électrons. Ces études jouent un rôle important dans les technologies de l'information émergentes d'aujourd'hui en fournissant de nouvelles fonctions aux dispositifs électroniques conventionnels. L'électronique de Spin permet donc d'envisager la prochaine génération de dispositifs plus petits, plus rapides, non volatil tout en réduisant la forte consommation d'énergie.

Le début de l'ère de l'électronique de spin remonte à la fin des années 1980 depuis la découverte de la magnétorésistance géante (GMR) et de la magnétorésistance tunnel (TMR). L'idée de base de la GMR/TMR est que la résistance d'un système composé de deux couches ferromagnétiques peut varier considérablement en fonction de l'orientation relative de leurs aimantations. L'utilisation de l'effet GMR et TMR sur les têtes de lecture magnétiques a conduit à une amélioration considérable de l'industrie du stockage de données. Cependant, dans les têtes de lecture GMR / TMR, l'aimantation est manipulée en utilisant un champ magnétique externe.

Un autre phénomène important lié au spin, est le couple de transfert de spin (STT), qui a été découvert en 1996 par L. Berger et J. Slonczewski. L'idée est que si un courant polarisé en spin est dirigé vers une couche magnétique, une partie du moment cinétique de spin peut être transféré vers cette couche magnétique. Le couple de transfer de spin permet de manipuler l'orientation de l'aimantation. Cet effet a été utilisé pour la manipulation de l'aimantation par courant électrique pour construire une mémoire magnétique à accès aléatoire (MRAM). Le composant central d'un dispositif STT est la jonction tunnel magnétique (MTJ) qui se compose de deux ferromagnétiques séparés par un mince isolant servant de barrière tunnel. La STT-MRAM est une mémoire non volatile ce qui est un avantage majeur par rapport aux mémoires conventionnelles basées sur la charge. La STT-MRAM présente également les avantages d'avoir une consommation d'énergie plus faible et une taille plus faible par rapport à la MRAM conventionnelle qui utilise un champ magnétique pour commuter l'aimantation. Cependant, la

quantité élevée de courant nécessaire pour contrôler l'aimantation dans le dispositif STT reste un défi. De plus, lorsque le courant de charge passe à travers la couche isolante, une densité de courant d'écriture très - trop importante peut entraîner la rupture de l'isolant. Ainsi, la réduction de la densité de courant de commutation dans le dispositif STT nécessite encore des recherches supplémentaires.

Au cours de la dernière décennie, un autre type de couple permettant la manipulation d'aimantation a attiré de plus en plus l'attention, il s'agit du couple spin-orbit (SOT). Un dispositif SOT typique est constitué d'une couche ferromagnétique (FM) et d'une couche de métal lourd (HM) coiffée d'un oxyde. Lors de l'injection d'un courant de charge dans le plan de la bicouche, un courant de spin transversal est généré en raison du couplage spin-orbite (SOC). L'accumulation de spin à l'interface FM/HM exerce le couple SOT sur la couche FM, qui peut commuter l'aimantation. Les dispositifs SOT ont le potentiel de surmonter les difficultés qui apparaissent dans les dispositifs STT avec un intérêt supplémentaire en termes de consommation d'énergie et de fonctionnement plus rapide des appareils. Une communauté importante a travaillé sur la compréhension de la physique fondamental du SOT ainsi que sur les applications pratiques liées au SOT.

Jusqu'à présent, pour la recherche SOT, les couches utilisées sont principalement ferromagnétiques. Cependant, plus récemment, des systèmes magnétiques composés de deux sous réseaux à couplage d'échange antiparallèle, tels que les matériaux ferrimagnétiques, sont également devenus des candidats prometteurs pour la commutation d'aimantation par SOT. Les alliages ferrimagnétiques (FiM), combinant les terres rares (RE) et les métaux de transition (TM) offrent de nombreux avantages car l'aimantation totale du système peut être ajuster en faisant varier les compositions de l'alliage RE-TM ou la température. Le fait que le couple spin orbite peut-être fort ainsi que le fait que les propriétés magnétiques peuvent être aisément modifier rendent ce type de matériaux attrayants pour de futurs applications.

L'objectif principal de ma thèse est d'étudier l'effet du couple spin-orbite sur une couche mince ferrimagnétique. Nous voulons donc explorer la possibilité d'utiliser un matériau ferrimagnetique (FiM) pour l'électronique de spin et savoir si le courant critique permettant de commuter une aimantation perpendiculaire peut être fortement réduit. Pour ce faire, deux études principales ont été réalisées. L'une concerne le calcul du courant critique dans les systèmes FiM / HM, et l'autre concerne l'effet de la composition de l'alliage et de la température sur la

manipulation de l'aimantation induite par le courant. Pour ces études, nous avons choisi le système W / CoTb.

Le manuscrit est divisé en quatre chapitres.

Chapitre I: Généralités: Nanomagnétisme et électronique de spin

Ce chapitre présente les concepts de base nécessaires à mes recherches sur la manipulation de l'aimantation de couches minces ferrimagnétiques par couple spin-orbite. Je définis d'abord l'aimantation et les interactions magnétiques à l'intérieur d'un film mince ferromagnétique (FM) puis ferrimagnétique (FiM). Je définis également les nouveaux concepts en électronique de spin tels que le courant de spin, la conversion courant de charge- courant de spin résultant du couplage spin-orbite, à savoir l'effet Hall de spin. Enfin, le couple spin-orbite dû à l'effet Hall de spin est discuté. En résumé, un courant de spin pur dans les métaux est simplement défini comme des électrons avec des spins opposés se déplaçant dans des directions opposées. L'effet Hall de spin (SHE) peut être compris comme la diffusion asymétrique dépendante du spin électronique due au couplage en orbite de spin. Dans le SHE direct, un courant électrique traversant un matériau avec un couplage spin-orbite relativiste va générer un courant de spin transversal. L'effet réciproque existe également et est appelé SHE inverse (ISHE). Cela se produit lorsqu'un courant de spin pur, injecté à travers un matériau ayant des propriétés de couplage Spin-Orbit, génère un courant de charge transversal.

Le courant de spin ou l'accumulation de spin généré par le SHE dans un métal lourd (HM) ou un alliage à fort SOC peut être exploité pour manipuler l'aimantation d'une couche magnétique FM adjacente dans une bicouche HM / FM. La manipulation de l'aimantation d'une couche FM sans une autre électrode FM exploitant la conversion courant de spin- courant de charge due au couplage orbite-spin, a été montrée expérimentalement. Ce nouveau phénomène, appelé Couple Spin-Orbit ou Spin Orbit Torque (SOT), a été proposé comme alternative à la technologie STT-MRAM permettant une consommation d'énergie encore plus faible.

Chapitre II: Méthodes expérimentales et échantillons

Nous avons réalisé une série d'échantillons W (3 nm) / CoxTb1-x (3,5 nm) / Al (3 nm, naturellement oxydé) comme système modèle pour cette recherche. Nous avons choisi le tungstène (W) comme métal lourd dans la structure en raison du grand spin Hall angle du W. Et nous avons choisi les alliages CoxTb1-x comme couche magnétique pour tirer le meilleur parti des matériaux ferrimagnétiques permettant d'ajuster l'aimantation total en changeant la composition des échantillons ou la température. La technique de croissance que nous avons

choisie est la pulvérisation magnétron. Nous présentons dans ce chapitre, la pulvérisation magnétron et soulignons le rôle important des magnétrons dans l'augmentation de l'efficacité de la pulvérisation. Nous discutons également les paramètres utilisés pour l'élaboration d'alliages CoxTb1-x par co-pulvérisation. Les échantillons ont été caractérisés en utilisant différentes techniques. Il s'agit notamment des méthodes de magnétométrie (SQUID-VSM), permettant d'étudier l'orientation de l'aimantation des films minces, et des mesures de magnéto-transport pour les propriétés électriques. Les méthodes de Lithographie permettant de réaliser des dispositifs de tailles réduites est présenté. L'objectif principal de ce chapitre est de décrire en détail les systèmes expérimentaux permettant d'effectuer les principales mesures magnéto-électriques. Le système se compose principalement d'un électroaimant pour régler le champ magnétique, d'une puce permettant de connecter l'échantillon à une source de courant et d'un voltmètre. Il nous a permis d'effectuer des mesures électrique DC, et sous des impulsions courtes de courant. Nous avons pu également adapter la configuration du système pour effectuer des expériences à différentes températures allant de 10K à 350K en utilisant un système cryogénique PPMS permettant d'appliquer un champ maximum de 7T.

Chapitre III : Retournement d'aimantation sous l'effet du couple spin-orbite dans des alliages ferrimagnétiques : Expériences et modélisations

Nous avons étudié le retournement d'aimantation induite par le couple spin-orbite (SOT) dans les alliages ferrimagnétiques (métaux de transition - terres rares) en étudiant les bicouches CoxTb1-x comme système modèle. Nous avons obtenu le retournement d'aimantation par SOT pour une large gamme de concentrations de Co et Tb, y compris des échantillons près du point de compensation magnétique. On constate que le courant de retournement varie continument avec la composition de l'alliage et aucune réduction du courant de retournement n'est observée au point de compensation magnétique malgré une très grande efficacité SOT. Pour expliquer ces résultats expérimentaux, nous avons développé un modèle simple basé sur les équations modifiées de Landau-Lifschitz-Gilbert (LLG). Le modèle montre que la densité critique de courant de retournement ne dépend pas directement de la valeur de l'aimantation mais du champ d'anisotropie perpendiculaire effectif Hk. Hk n'est pas minimum à la compensation magnétique, ce qui explique l'absence d'un courant de retourenement minimum à la compensation. Ce modèle suggère également que les mesures de champ SOT effectif conventionnel ne permettent pas de conclure si le moment angulaire est transféré à un sous-réseau ou à la magnétisation total de l'alliage. Nous présentons également des mesures utilisant la technique basée sur le mouvement de la paroi de domaine (DW) pour obtenir le champ SOT efficace et l'angle de Hall

de spin correspondant. Nous constatons que l'angle de Hall de spin effectif augmente d'un facteur 2 avec l'augmentation de la concentration de Tb, indiquant une contribution supplémentaire des atomes de Tb au SOT.

Chapitre IV: L'effet de la température sur le retournement de l'aimantation par couple spin-orbite dans le système métal / ferrimagnétique

Dans ce chapitre, j'aborde l'influence de la température sur le retournement de l'aimantation induite par le courant par couple spin-orbite en considérant les expériences réalisées sur des systèmes W / CoxTb1-x / Al. Nous démontrons que l'effet thermique est un effet essentiel pour expliquer le retournement d'aimantation induite par le courant dans ce système. Lorsque le courant est injecté dans la bicouche, le chauffage par effet Joule entraîne une forte augmentation de la température de l'échantillon. En utilisant des mesures SOT systématiques à différentes températures et compositions d'alliages, nous avons établi que pour chaque concentration x, le retournement de l'aimantation induite par le courant se produit pour une température d'échantillon unique Tswitch (x). Cette température de retournement caractéristique Tswitch est supérieure aux températures de compensation magnétique (TMcomp) et angulaire (TAcomp) mais inférieure à la température de Curie. Tswitch évolue comme la température de Curie (TC) de l'alliage.

Conclusions

Ce travail fournit de nouvelles perspectives sur les phénomènes de retournement de l'aimantation induits par SOT tant pour les aspects théoriques que pour les applications dans ce domaine.

Une série d'alliages ferrimagnétiques RE-TM CoxTb1-x en contact avec une couche de métal lourd le tungstène (W) avec une large gamme de compositions a été réalisée avec succès par pulvérisation magnétron DC. Tous les échantillons présentent une anisotropie magnéto-cristalline perpendiculaire forte. Nous avons présenté les expériences de retournement d'aimantation induites par le courant pour toutes les compositions d'échantillons et pour une large gamme de température allant de 10K à 350K. Le retournement d'aimantation induit par le SOT est obtenue pour tous les échantillons. Même pour un échantillon proche du point de compensation, la commutation est obtenue avec une densité de courant modérée (~ 10^{11} A /m^2) malgré un champ coercitif très important, ce qui est très interessant pour les applications dans le domaine des mémoires magnétiques.

Nous n'avons observé aucune réduction de la densité de courant de retournement au point de compensation magnétique. Un modèle simple basé sur des équations LLG couplées

antiferromagnétiquement a été développé pour expliquer ces résultats expérimentaux. Nous avons pu souligner que la densité de courant de retournement est proportionnelle à l'anisotropie effective, qui n'est pas minimale au point de compensation magnétique. Nous notons également que la mesure du champ SOT effectif conventionnelle ne permet pas clore le débat sur l'effet des courants de spin absorbés par un sous-réseau de l'aimantation particulier ou par l'aimantation totale.

En plus de l'effet SOT, nous avons observé une forte contribution thermique dans le processus de retournement de l'aimantation. Dans le système étudié, les résistivités de la couche ferrimagnétique et de la couche W sont du même ordre de grandeur, ce qui conduit à un fort échauffement. Nous avons pu démontrer que chaque échantillon, quel que soit sa composition, doit atteindre une certaine température Tswitch pour réaliser le retournement. Cette température Tswitch augmente avec la concentration de Co qui évolue ensuite avec la température de Curie Tc. Ces résultats soulignent l 'importance de considérer les contributions thermiques dans le retournement d'aimantation SOT. Nous notons que le système W / CoTb est un système robuste dans lequel le retournement d'aimantation SOT est toujours reproductible malgré la forte contribution de chauffage. Cela peut ouvrir la voie à de nouvelles applications tirant parti des effets de chauffage plutôt forts dans les dispositifs électroniques de taille de plus en plus réduite. Dans l'ensemble, W / CoTb / AlOx est un système modèle intéressant pour étudier les phénomènes liés au SOT où il reste de nombreuses perspectives de recherche pour une meilleur compréhension des phénomènes de retournement induit par le courant. La densité de courant pourrait être réduite en utilisant la phase bêta du tungstène (W). De plus, il sera intéressant d'étudier le retournement d'aimantation induit par le courant en fonction de la durée de l'impulsion sur une large gamme de la nanoseconde à la milliseconde afin de bien comprendre le rôle de la température sur le retournement. Une autre direction de recherche intéressante sera de combiner le retournement d'aimantation tout optique (AOS) et le retournement d'aimantation par couple Spin-orbite sur un système à base de couches minces ferrimagnétiques. En effet, nous avons commencé quelques premières étude sur l'effet du couple spin-orbite sous l'influence du laser. Jusqu'à présent, nous avons observé une nette réduction de la densité de courant critique nécessaire pour le retournement de l'aimantation par SOT avec la présence du laser, probablement en raison de l'effet de chauffage. Une étude beaucoup plus systématique serait nécessaire pour exploiter le potentiel de la combinaison AOS - SOT.

Introduction

In conventional electronics, devices are constructed based on the utility of electron charge only. The electron also possesses a spin angular momentum. Spintronics is the field that specifically study spin properties in addition to charge degrees of freedom of electrons. These studies play an important role in today's emerging information technology by providing new functions to conventional electronic devices, thus enabling next generation of devices which could be smaller, faster, non-volatility, more powerful while simultaneously low power consumption. The beginning of spintronics era dates back to the end of 1980s since the discovery of the giant magnetoresistance (GMR) and tunnel magnetoresistance (TMR). The basic idea of GMR/TMR is that the resistance of a system consisting of two ferromagnetic layers can vary significantly depending on the relative orientation of their magnetizations. The use of GMR and TMR effect on magnetic read heads led to a vastly improvement in data storage industry. However, in the GMR/TMR read heads, the magnetization was still manipulated by using an external magnetic field.

Another important spin-related phenomenon, the spin transfer torque (STT), was discovered in 1996 by L.Berger and J.Slonczewski. The idea is that if a spin-polarized current is directed into a magnetic layer, the angular momentum can be transferred to this layer, changing magnetization orientation. This effect was used for electrical manipulation of magnetization, for example to build magnetic random access memory (MRAM). The core component of a STT device is the magnetic tunnel junction (MTJ) which consists of two ferromagnets separated by a thin insulator serving as a tunnel barrier. STT-MRAM is a non-volatile memory which is a major advantage over charge-based conventional memories. STT-MRAM also has advantages of lower power consumption and better scalability than conventional MRAM which uses magnetic field to switch the magnetization. However, the high amount of current needed to control the magnetization in STT device is a challenge. Moreover, when the charge current tunnels through the insulating layer, a too large write current density can lead to the breakdown of the insulator. Thus, the reduction of the switching current density in STT device still demands further research.

In the last decade, spin orbit torque (SOT) has attracted increasing attention as a new technique for electrical manipulation of magnetization. A typical SOT device is a combination of a ferromagnetic layer (FM) and a heavy metal layer (HM) capped by an oxide. When injecting an in-plane charge current into the bilayer, a transverse spin current is generated due

to the spin-orbit coupling (SOC). The spin accumulation at the interface exerts the torque on the FM layer, then switch the magnetization. SOT devices have potential to overcome the shorcoming of STT devices with additional advantages in terms of lower power consumption and faster device operation. A large community has been working on understanding the physics of SOT as well as realizing the potential of SOT device on practical applications.

So far, FMs are major favourite material choices for SOT research. However, more recently, antiparallelly coupled magnetic systems, such as ferrimagnets, have also emerged as promising candidates for SOT switching. Ferrimagnetic alloy materials (FiM), combining rare-earths (RE) and transition-metals (TM) provide many advantages since the net magnetization of the system can be tuned by varying the RE-TM compositions or temperature. The highly efficient SOT as well as highly tunable properties make these materials attractive for potential devices applications.

The main goal of my PhD is to study spin-orbit torque in ferrimagnet. We want to exploit ferrimagnet (FiM) for spin-orbitronics and to know if the critical current to switch a perpendicular magnetization is strongly reduced or not close to the compensation magnetization point or temperature. In order to achieve that, two main studies were performed. One is from the calculation of the critical current in FiM/HM systems as elaborated in chapter 3, and the other is the systematically study of the current-induced magnetization switching for different compositions and temperatures. We have chosen the W/CoTb system to develop all these studies.

The manuscript is divided in four chapters:

Chapter 1 is the state of the art, presenting the basics of magnetism and spin orbit torques.

Chapter 2 introduces the samples and presents the experimental methods for this research.

Chapter 3 and 4 presents obtained results for W/CoTb system. Chapter 3 shows the model we developed to explain the experimental results while chapter 4 presents experimental results in more details with focus on the effect of temperature on SOT switching.

Chapitre I

Généralités : Nanomagnétisme et l’électronique de spin

Résumé

L’objectif de ce chapitre est de présenter les concepts de base en nanomagnétisme et électronique de spin qui sont nécessaires pour le reste du manuscrit. En effet, dans les chapitres III et IV je présenterai mes travaux sur la manipulation de l’aimantation de couches minces ferrimagnétiques sous l’effet du couple de spin-orbite. Dans la suite de ce chapitre, je définis l’aimantation magnétisation et les interactions magnétique présentent à l'intérieur d'un film mince ferromagnétique ou ferrimagnétique ou à l’interface entre une couche mince non-magnétique et une couche mince magnétique. Je définirai également les concepts d’électronique de spin tels que les courant de spin, la conversion courant charge – courant de spin principalement due au couplage spin-orbite, à savoir l'effet Hall de spin. Ensuite le couple spin-orbite dû à l'effet Hall de spin est discuté.

Summary

The goal of this chapter is to present the basic concept needed for the rest of the manuscript. Indeed, in chapter III and IV I will present my work on the magnetization manipulation of Ferrimagnetic thin film using spin orbit. In this chapter I will then define the magnetization and the magnetic interaction inside a ferromagnetic and a ferrimagnetic thin film. I will also briefly define the new concepts in spintronic such as spin current, spin-charge current conversion mainly due to spin-orbit coupling, namely spin Hall effect. Then, the spin-orbit torque due to spin Hall effect is discussed.

Chapter I

Basics of magnetism and spin orbit torque

1.1 Origin of magnetization

Magnetism in materials originates from the motion of electrons around the atoms nucleus. In classical mechanics, if we consider a particle with mass m and a charge q along a circular path of radius r, we can show the link between the magnetic moment (**μ**) created by the rotating charge and the angular momentum (**L**) created by a rotating mass such that

$$\vec{\mu} = \gamma \vec{L} \tag{1.1}$$

Where $\vec{\mu} = I.\vec{S}$ with I is the current generated by the particle motion and the vector $\vec{S}$ is the surface delimiting the extension of its displacement and γ= q/2m is the gyromagnetic factor. The above description was a classical approach if we generalize it using quantum mechanics concept the electron magnetic moment has two components; the orbital one $\overrightarrow{\mu_L}$ and the spin one $\overrightarrow{\mu_S}$. They can both be expressed as follows:

$$\overrightarrow{\mu_L} = -\mu_B g_L \vec{L} \quad \text{and} \quad \overrightarrow{\mu_S} = -\mu_B g_S \vec{S} \tag{1.2}$$

Where g_L and g_S are the Landé factors for the orbit and the spin (respectively and $\mu_B = \frac{eh}{4\pi}$ is the Bohr magneton. The net magnetization $\vec{M}$ will be given by considering all the magnetic moments in a given volume V:

$$\vec{M} = \frac{\sum_i \overrightarrow{\mu_i}}{V} \tag{1.3}$$

for the rest of the manuscript the quantity $\vec{M}$ will be considered as the total magnetization per unit of volume. While most of the atoms are magnetic (the total magnetic moment is not equal to zero), a solid formed of magnetic materials is not necessarily magnetic if no external magnetic field is applied. The response of a material to an external magnetic field is characterized by the magnetic susceptibility χ defined by $\vec{M}=\chi\vec{H}$, $\vec{H}$ being the applied field. For

diamagnetic materials χ is a negative constant, for paramagnetic materials χ is a positive constant. For ferromagnetic materials χ is a matrix whose values evolve with $\vec{H}$ and the magnetic history of the materials.

1.2 Magnetic interactions

In ordered magnetic materials as ferromagnets, ferrimagnets and antiferromagnets, magnetic moments are subject to various interactions associated with different energy terms. The most important interaction terms are developed in this part. These interactions are described in more details in several references [1] [2]

1.2a) Zeeman interaction

A magnetic moment $\vec{\mu}$ tends to follow an applied magnetic field $\overrightarrow{H_{ext}}$. This is called the Zeeman effect. The associated energy is expressed as:

$$E_{Zee} = -\mu_0 \, \vec{\mu}.\overrightarrow{H_{ext}} \qquad (1.4)$$

In the case of a uniform magnetization $\vec{M}$ in a volume V the energy is given by

$$E_{Zee} = -\mu_0 V \, \vec{M}.\overrightarrow{H_{ext}}$$

The energy is then minimum if the magnetization is parallel to the applied field.

1.2b) Dipolar interaction

The dipole-dipole magnetic interaction, also known as dipolar coupling, refers to the direct interaction between two magnetic dipoles. The energy of this interaction between two magnetic moments $\overrightarrow{\mu 1}$ and $\overrightarrow{\mu 2}$ separated by a distance r is expressed as follows:

$$\overrightarrow{E_{dip}} = \frac{1}{4\pi}\left[\frac{3(\overrightarrow{\mu 1}.\vec{r}).(\overrightarrow{\mu 2}.\vec{r})}{r^5} - \frac{\overrightarrow{\mu 1}.\overrightarrow{\mu 2}}{r^3}\right] \quad (1.5)$$

We can also describe this interaction by calculating the field, known as the dipolar field, created by a dipole of magnetic moment $\overrightarrow{\mu 1}$ at a distance r is:

$$\overrightarrow{H_{dip1}} = \frac{1}{4\pi}\left[\frac{3(\vec{\mu}1.\vec{r}).\vec{r}}{r^5} - \frac{\overrightarrow{\mu 1}}{r^3}\right] \quad (1.6)$$

The interaction between this field created by dipole $\overrightarrow{\mu 1}$ on dipole $\overrightarrow{\mu 2}$ is given by :

$$E_{dip} = -\mu_0\, \overrightarrow{\mu 2}.\overrightarrow{H_{dip1}} \quad (1.7)$$

If we consider a bulk sample, we will have a number of dipoles that act at a long range so all the generated dipolar fields add up to form a total field called the demagnetizing field $\overrightarrow{H_{dem}}$ that is opposite to the total magnetization if all the moments are parallel. This field depends on the shape on the sample for a uniform magnetization. Its general expression is:

$$\overrightarrow{H_{dem}} = -4\pi\, \overline{\overline{N_d}}.\overrightarrow{M_T} \quad (1.8)$$

$\overline{\overline{N_d}}$ is a demagnetization tensor that depends on the shape of the sample and $\overrightarrow{M_T}$ the total magnetic moment of the whole sample. If we consider a thin film elongated in the x and y direction we have N_{ZZ}=1 and the rest of the coefficients are equal to 0. The resulting energy is:

$$E_{dem} = -\frac{1}{2}\mu_0 \overrightarrow{M_T}.\overrightarrow{H_{dem}} = 2\pi\mu_0 M_Z^2 = 2\pi\mu_0 M_S^2 cos^2\theta \quad (1.9)$$

Where θ is the angle between the magnetization and the demagnetizing field.
In a thin film the magnetization tend to align in plane because of the dipolar field.

We can notice that in this expression the demagnetizing field helps to put the magnetization in the plane of the sample. In this description the demagnetization energy only depends on the shape of the object considered. It is then called shape anisotropy.

1.2c) Magnetocrystalline and effective anisotropy

In a magnetic crystal magnetic moments tend to be aligned along some preferred crystallographic directions. These directions are called easy axis of magnetization (or just "easy axis" for convenience). The magnetocrystalline anisotropy originates from the spin-orbit interaction. Indeed the orbital motion of the electrons which couples with crystal electric field gives rise to the first order contribution to magnetocrystalline anisotropy. The magnetocrystalline anisotropy energy is generally represented as an expansion in powers of the direction cosines of the magnetization which can give a complicated expression. The simplest expression for the magnetocrystalline anisotropy is considered uniaxial along a Δ axis:

$$E_K = -KVcos^2\theta \qquad (1.10)$$

θ is the angle between the magnetization and the magnetocrystalline anisotropy axis Δ.

In the case of thin films and multilayers where interfaces need to be considered the magnetic anisotropy does not depend only on bulk properties but an interface anisotropy needs to be considered. Moreover we have to take into account the shape anisotropy. We then define an effective anisotropy that includes the volume effects (K_V), the interfacial effects (K_S) and the shape anisotropy generated by the dipolar field. From equation (1.10) and (1.9) the expression of effective anisotropy constant K_{eff} is given by:

$$K_{eff} = K_V + \frac{K_S}{t} - 2\pi\mu_0 M_S^2 \qquad (1.11)$$

The interfacial contribution of anisotropy (K_S) predicted by Néel can induce perpendicular magnetic anisotropy (PMA) easy axis in thin films. This originates from the hybridization at the interface between two materials. This is the case in Co/Pt thin multilayers. It is then of primary importance to have thin layers of magnetic materials to increase the surface contribution of the anisotropy compared to the demagnetizing field, in order to obtain a perpendicular anisotropy. In TbCo and GdCo the PMA comes from the bulk contribution. Note that if the magnetization of the material is low the shape anisotropy that tends to align the magnetization in plane is lower.

1.2d) Exchange interaction

The exchange interaction is felt between two spins $\overrightarrow{S_1}$ and $\overrightarrow{S_2}$ and given by:

$$\varepsilon_{ex} = -2J_{12}\,\overrightarrow{S_1}.\overrightarrow{S_2} \qquad (1.12)$$

where J_{12} is called the exchange interaction constant (or integral).

Indeed, since electrons are fermions they are subject to the principle of exclusion of Pauli which prohibits two electrons to be in the same exact state and forces the wavefunction of the electron to be antisymmetric. The exchange interaction is a consequence of this and the Coulomb interaction.

The exchange interaction can be generalized as the interactions between two neighbor magnetic moment $\overrightarrow{\mu_1}$ and $\overrightarrow{\mu_2}$:

$$E_{ex} = -\mu_0 A_{ex}\,\overrightarrow{\mu_1}.\overrightarrow{\mu_2} \qquad (1.13)$$

where A is the exchange constant.

1.2e) DMI interaction

The Dzyaloshinsky-Moriya interaction (DMI) [3] [4] between two spins $\overrightarrow{S_1}$ and $\overrightarrow{S_2}$ is given by:

$$E_{DMI} = \overrightarrow{D_{12}}\,.\,(\overrightarrow{S_1} \times \overrightarrow{S_2}) \qquad (1.14)$$

where $\overrightarrow{D_{12}}$ is oriented perpendicularly to the segment between the spins $\overrightarrow{S_1}$ and $\overrightarrow{S_2}$. One can define a DMI constant D such that $\overrightarrow{D_{12}} = D\overrightarrow{r_{12}}$

Its origin has been attributed to the spin orbit coupling in 1960 by Moriya [4]. This expression has been generalized by Fert and Levy to spin glasses doped with heavy metal impurities.

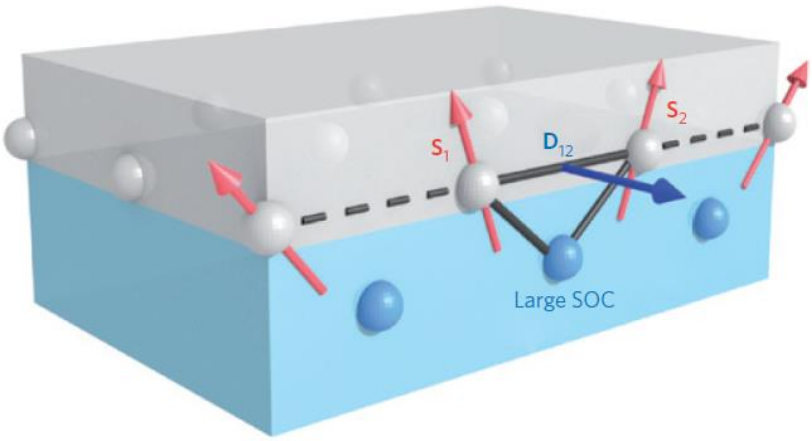

Figure 1.1: *Sketch of a DMI at the interface between a ferromagnetic metal (grey) and a metal with a strong SOC (blue). The DMI vector D_{12} related to the triangle composed of two magnetic sites and an atom with a large SOC is perpendicular to the plane of the triangle. Because a large SOC exists only in the bottom metal layer, this DMI is not compensated by a DMI coming from a symmetric triangle. Extracted from* [5]

1.3 Magnetic orders

Ferromagnetic material

In a ferromagnetic compound, the exchange constant is positive (A > 0), which leads to a parallel coupling of the magnetic moments (Figure 1.2). It follows an alignment of the magnetic moments at the microscopic scale and the appearance of a ferromagnetic order

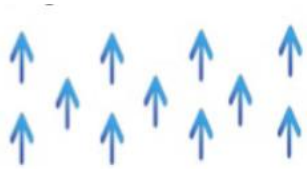

Figure 1.2: *Sketch of a ferromagnetic order: all magnetic moment are parallel*

In fact the magnetic order is set by the competition between the exchange interaction with the thermal fluctuations. If the thermal energy is higher than the exchange energy the magnetic order is broken and the material becomes paramagnetic. The temperature of transition

between a ferromagnetically ordered state and a paramagnetic state is called the Curie temperature (T_C).

Antiferromagnetic order

If A is negative, the magnetic moments on the atoms tend to set antiparallel with their neighbors and, there is no total magnetic moment. In this case the material is antiferromagnetic.

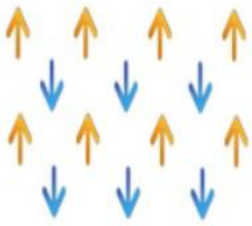

Figure 1.3: *Sketch of an antiferromagnetic order: the directions of the magnetic moments are alternatively up and down*

A ferrimagnetic order

A ferrimagnetic material is a material that has two sub-networks that do not have the same magnetization. The magnetic moments of the atoms can be opposite; the resulting moment being positive, or negative (Figure 1.4). Let us consider the example of a CoTb alloy. In this material $A_{Co\text{-}Co}$ and $A_{Tb\text{-}Tb}$ are positive while $A_{Co\text{-}Tb}$ is negative and the magnetic moments of Co and Tb atoms are different. This results in two sublattices (one of Co and one of Tb) antiparallelly aligned with respect to each other. Depending on the relative concentration of Co and Tb the net magnetization can either be mainly along the Tb moments or along the Co moments. Such a material with sublattices of opposite directions of magnetization is called a ferrimagnet.

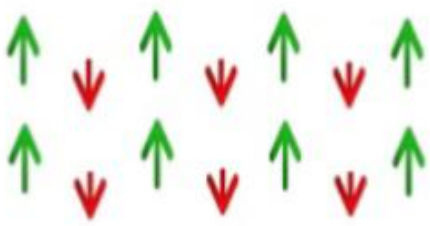

$$\overrightarrow{M_{tot}} = \overrightarrow{M_{Co}} + \overrightarrow{M_{Tb}}$$

Figure 1.4: *Sketch of a ferrimagnetic order*

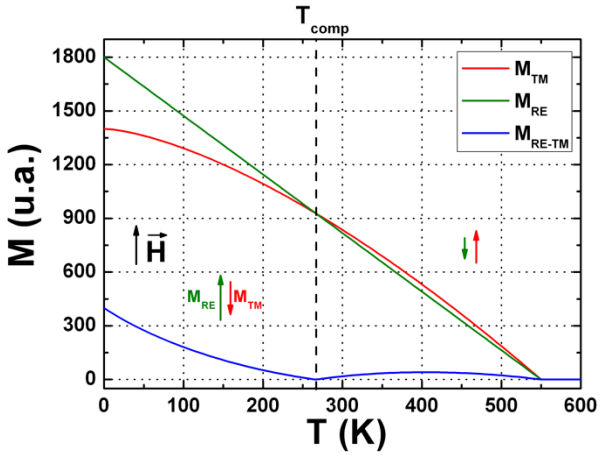

Figure 1.5: *Calculated magnetization of the transition metal sub-network (in red), the rare earth sub-network (in green) and the alloy (in blue) as a function of temperature.*

The case of an alloy is a bit more complex. Any magnetic order set by the exchange interaction (ferromagnetic, ferromagnetic, and antiferromagnetic) is in competition with the thermal fluctuations. If the thermal energy is higher than the exchange energy the magnetic order is broken and the material is paramagnetic. The temperature of transition between a magnetically ordered state and a paramagnetic state is called the Curie temperature (T_C) for ferromagnetic and ferromagnetic materials while it is called Néel temperature (T_N) for an antiferromagnetic material.

This exchange interaction exists between all the neighbor magnetic moments in a layer but also between two layers, for instance between a Co and an IrMn layer or a Co and a Ni layer as we will notice later in this manuscript.

1.4 Spintronics

In 1988 and 1998 a couple of works were published reporting a variation of electrical resistance upon a variation of an external field in Fe/Cr superlattices [6] and Fe/Cr/Fe trilayers [7]. These variations of magnetoresistance were the biggest measured at that time and thus, it was the discovery of the so-called Giant MagnetoResistance (GMR). Those works are considered as the birth of "spintronics". But what is spintronics? It is a science or field of research, not only a technology, that studies the role not only of electron charge but also of the one of electron spin in a number of physics phenomena in condensed matter. In the beginning

of spintronics, manipulation and creation of spin polarized current was a key new concept. Thus, the production of spin polarized current by magnetic materials was used in "classical" spintronics. This happened in the first decade after GMR discovery. Other events that boosted the activity of research in spintronics were the discovery of Tunnel Magnetoresistance (TMR) and spin transfer torque (STT). In figure 1.6 are shown the concept and schematic of the GMR as well as the mainstream application in technology, the read/writer HDD. The industrial applications of these discoveries, such as Hard Disk Drive (HDD) write/read head by IBM in 1997, heightened even more the spintronic activities not only for fundamental research but now also for the potential applications. Beyond applications in read/writer HDD, both GMR and TMR are widely used in magnetic sensors.

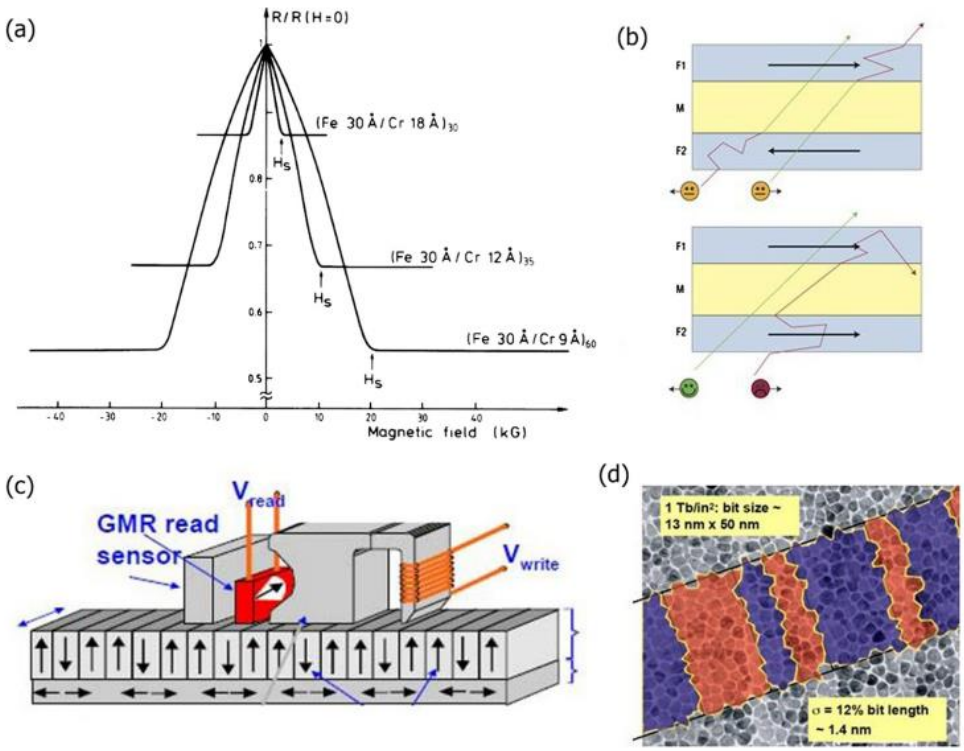

Figure 1.6: *Discovery of GMR. (a) GMR in Fe/Cr(001) multilayers. With the current definition of the magnetoresistance ratio, MR = 100 × [RAP − RP/Rp] , MR = 85% for the Fe 3 nm/Cr 0.9 nm multilayers. GMR effects were observed at about the same time with Fe/Cr/Fe trilayers by the team of Peter Grünberg at Jülich. (b) Schematic of the mechanism of the GMR. In the parallel magnetic configuration (bottom), the electrons of one of the spin directions can go easily through all the magnetic layers and the short-circuit through this channel leads to a small resistance. In the antiparallel configuration (top), the electrons of each channel are slowed down every second magnetic layer and the resistance is high. (c) Schematic of a GMR write/read head in HDD (courtesy of Dr. C. Tiusan). (d) Example of magnetic bits on the HDDs of today. Figure and caption taken from ref* [8]

Prior to introduce the spin current concept, let's recall the spin polarized current. In the beginnings of spintronics spin-polarized currents were produced by using the influence of the orientation of the spin on the transport properties of the electrons in ferromagnetic conductors as suggested first by Mott [9], and had been experimentally demonstrated and theoretically described in the sixties [10] and seventies [11] [12].

Larger Magnetoresistance than in metallic trilayer structure was found in a magnetic tunnel junction (MTJ) where the metallic spacer in GMR structure was replaced but a barrier insulator I, aluminum oxide at first place but single-crystal MgO keep ones of the current TMR record at room temperature. The physical origin of this large TMR having a single-crystal barrier has been attributed to symmetry selection at a FM/I interface. In such interfaces, an evanescent wave function of a given symmetry is connected to the Bloch functions of the same symmetry and spin direction at the Fermi level of the electrodes. In (001)MgO barriers, one of the symmetries corresponding to highly spin-polarized bands has a much slower decay, which results in a higher TMR. Other symmetry rules have been observed in barriers made of different materials, leading to different properties such as negative effective spin polarization in $SrTiO_3$-based MTJ [13]. Thus is, we found one sign of TMR in Co/MgO/Co MTJ and the opposite in Co/$SrTiO_3$/Co one.

In a suitable FM/I/FM MTJ heterostructure two resistance states, high and low, are realized when the two magnetic layers are either parallel (usually low resistance) or antiparallel (usually high resistance) to each other. Therefore those states are associated to 1 or 0 in order to store information. Hence, new applications can be found to storage information using a MTJ as a magnetic bit element or in a logic circuit exploiting the 1 and 0 states. To change from one state to another or "write" the information an external magnetic field is used. This is possible using "word" and "bit" lines as displayed in the Figure 1.7. This so-called magnetic random access memory (MRAM) doesn't need power to keep stored the information, thus reducing the energy needed to operate these MRAM. This new MRAM and non-volatile memory allowed reducing energy consumption. MRAMs are in the market since 2006.

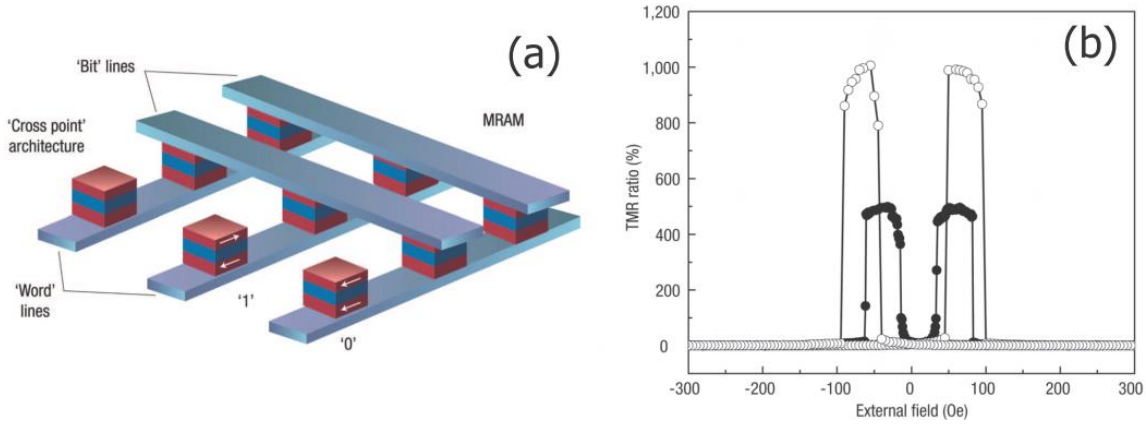

Figure 1.7: *a) Principle of the magnetic random access memory (MRAM) in the basic "cross point" architecture. The binary information "0" and "1" is recorded on the two opposite orientations of the magnetization of the free layer of magnetic tunnel junctions (MTJs), which are connected to the crossing points of two perpendicular arrays of parallel conducting lines. For writing, current pulses are sent through one line of each array, and only at the crossing point of these lines the resulting magnetic field is high enough to orient the magnetization of the free layer. For reading, one measures the resistance between the two lines connecting the addressed cell* [14]. *b) High magnetoresistance, TMR= (Rmax−Rmin)/Rmin, measured by for the magnetic stack* [15]*: $(Co_{25}Fe_{75})_{80}B_{20}$(4 nm)/MgO(2.1 nm)/ $(Co_{25}Fe_{75})_{80}B_{20}$(4.3 nm) annealed at 475 °C after growth, measured at room temperature (closed circles) and low temperature (open circles). Taken from ref.* [16]

Still it is possible to reduce even more the energy consumption in the magnetic memory if we are able to replace the external magnetic field for the write operation. This was made possible using the spin transfer torque (STT) concept introduced by Slonczewski [17] and Berger [18] in 1996. In this spin-transfer idea, one manipulates the magnetic moment of a ferromagnetic layer without applying any magnetic field but only by transfer of spin angular momentum from a spin-polarized current. The spin-polarized current is generated by the first magnetic element: the current coming out from the first magnetic layer is spin-polarized due to exchange interaction with the magnetization. The injection of a spin-polarized current into a second magnetic element leads to the transfer of the transverse component of the spin-polarized current, which creates a torque acting on the magnetization of the second magnetic element. This spin-transfer torque can be used to either switch the magnetization or to create a steady-state gyration regime. In the latter case, GMR or TMR can be used to translate this magnetization gyration into an oscillating voltage in the microwave frequency range, leading to the concept of spin-transfer oscillator.

The new kind of memory based on SST, namely STT-MRAM, was developed in 2005 [19], the first production in the market was in 2012 by EverSpin [20] and in the last two years were announced mass production by several companies including Samsung and Intel among others.

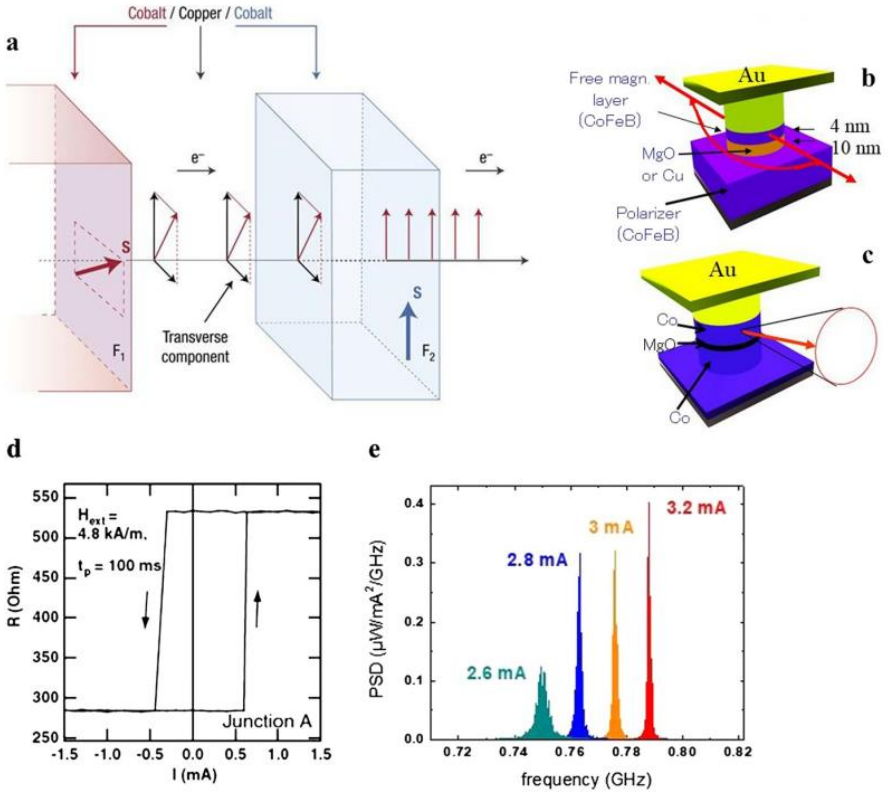

Figure 1.8: *(a) Illustration of the spin transfer concept introduced by John Slonczewski* [21] *and Berger* [22]. *A spin-polarized current is prepared by a first magnetic layer F with an obliquely oriented spin polarization with respect to the magnetization axis of a second layer F2. When it goes through F2, the exchange interaction aligns its spin polarization along the magnetization axis. The exchange interaction being spin conserving, the transverse spin polarization lost by the current is transferred to the total spin of F2, which can also be described by a spin-transfer torque acting on F2. (b) MTJ nano-pillar (as well, schematic of STT-RAM) for experiments of magnetic switching by STT: the magnetization of the free magnetic layer is reversed by the STT due to injection of a spin-polarized current created by the CoFeB layer. (c) Same as (b), but with the creation of a steady-state gyration of the magnetization of the free layer (STT oscillator). (d) An experimental example of back-and-forth switching between parallel and antiparallel MTJs* [23]. *Taken from* [8].

Spin current

A pure spin current in metals is simply defined as electrons with opposite spins moving in opposite directions. So, there is not net flow of electrons charges but only electrons spins [24] [25]. Such conveyance of angular moment is realized through spin waves in insulator ferromagnets. This simple novel concept is attracting a lot of interest in the field of generation, manipulation and detection of spin current for both fundamental research and practical applications. Today, the conversions of spin current into charge current and vice versa are essential operations in spintronics devices.

There are different ways to generate spin currents depending on the physical origin of the excitation such as heat [26], light, ferromagnetic resonance spin pumping [27], sound and spin orbit coupling phenomena [28] [29].

1.5 Spin Hall effect (SHE) - Spin Orbit Torque (SOT)

1.5.1 Spin Hall effect (SHE)

The spin Hall effect can be understood as the electron spin dependent asymmetric scattering [28] [30] [31] due to spin orbit coupling. In the direct SHE, an electrical current flowing through a material with a relativistic spin-orbit coupling will generate a transversal spin current (direct SHE). The reciprocal effect also exists and is called inverse SHE (ISHE). It happens when a pure spin current, injected through a material with spin orbit coupling properties, generates a transverse charge current. This asymmetric scattering was first proposed in 1971 by Dyakonov and Perel [32], however the interest was triggered with a new theoretical work with similar predictions by Hirsch [24] who gave the name to the phenomena and also with the fast development of spintronics. SHE was predicted and detected in semiconductors [33] [34] like GaAs [35], pSi [36], pGe [37] and nGe [38] [39] [40]; in metals [41] such as Pt [42] [43] [44] [45], Pd [46], Ta [47] [48] and W [49], and in alloys [50] [51] such as CuIr [52], CuBi [53], CuPb [54], and AuW [55]. The spin Hall effect is a bulk manifestation of the charge-spin current conversion due to spin orbit coupling. Thus the charge-spin current conversion happens in the bulk of the material but its detection should be performed at the edge of the sample. A schematic representation of the SHE and ISHE is showed in figure 1.9.

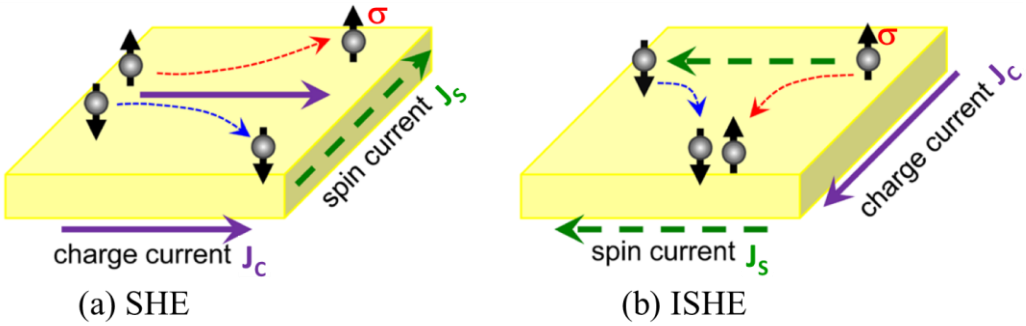

Figure 1.9: *Illustration of the direct spin Hall effect (a) and inverse spin Hall effect (b). J_c and J_s stand for charge and spin currents, respectively. The spin polarization vector of the spin current is denoted by σ, and its fulfilled: $J_s = -J_c \times \sigma$* **[56]**

1.5.2 Mechanism of the SHE

As for the Anomalous Hall effect (AHE), we have intrinsic and extrinsic contributions to the SHE, all due to SOC. The intrinsic mechanism is related to the interband coherence induced by an external electric field, i.e injection of charge current. There are two kinds of extrinsic mechanisms where electrons are deflected after scattering by an impurity due to effective SOC: the skew scattering and side jump. These contributions are illustrated in fig 1.10.

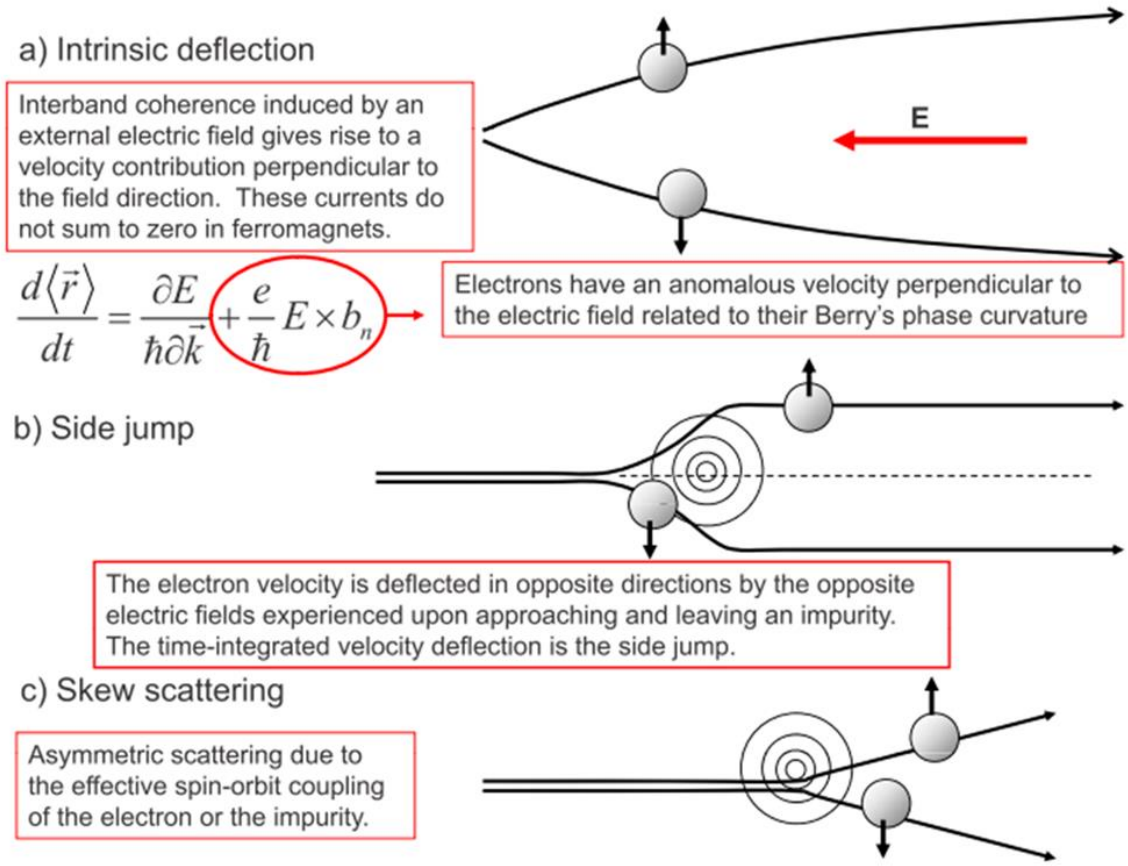

Figure 1.10: *Illustration of the three main mechanisms that can give rise to an AHE as well as SHE. Taken from* [57]

For the sake of comparison, in Fig. 1.11 are shown the three effects, Hall effect, AHE and SHE. In the Hall effect (discovery by Sir Edwin Hall in 1879) a conductor develops a transverse voltage due to the Lorentz force acting on the charge current in the presence of an external magnetic field. The AHE happens in FM materials. In FM materials the transverse voltage is not simply proportional to the magnetic field, but there is an additional contribution related to the magnetization. Thus, the electrons flowing in a ferromagnetic conductor acquire

a transverse velocity with opposite directions for different spin orientations. Therefore, spin dependent transverse velocity results in a net transverse voltage. As mentioned, in the SHE upon an injection of a charge current and without any external magnetic field is created no net voltage but a transverse spin accumulation is generated.

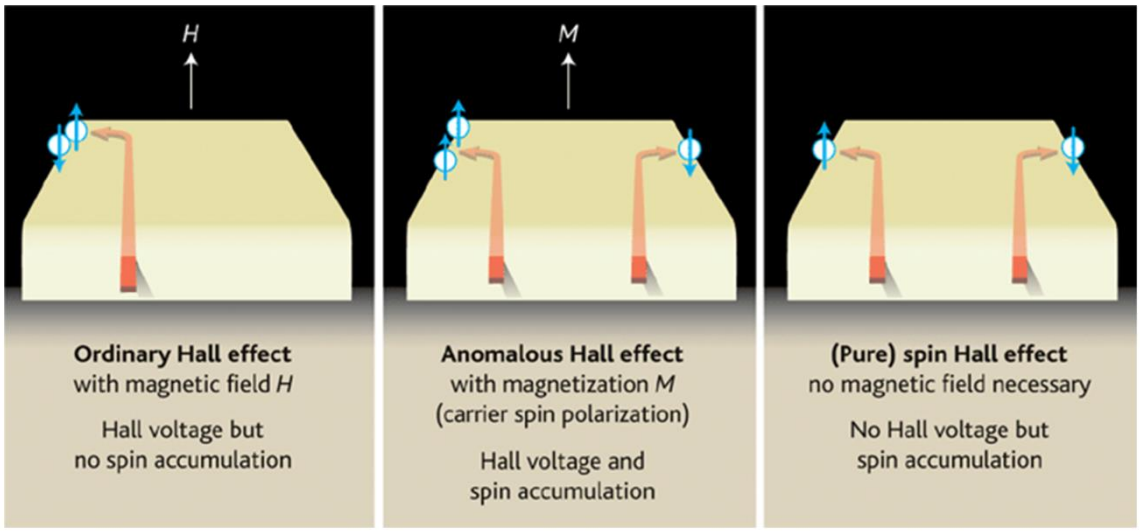

Figure 1.11: *Illustration of three phenomena due to SOC: Ordinary Hall effect in normal metals, AHE in magnetic metals, and SHE in normal metals with strong SOC. Taken from* [58]

1.5.3 Efficiency of SHE

The conversion ratio between the charge current and spin current is called the spin Hall angle (θ_{SHE}) which is a dimensionless parameter. The spin Hall angle is subsequently a key parameter to qualify a material for the integration in new experiments, and new spintronic-based devices. Large spin Hall angles can be found in 5*d* or 4*d* transition metals such as Pt, Ta, and W. Additionally in metal alloys such as CuBi, CuIr, and AuW, it will be possible to tune the magnitude of the spin Hall angle varying the composition of the alloy. Here there is a path to explore new alloys of Cu or Au host doped with impurities such as C, Bi or Os, in order to enlarge the SHE efficiency due to resonant asymmetric scattering by impurities [53] [59] as proposed already in 1981[44] [50]. Indeed, the spin Hall resistivity, ρ_{SHE}, is proportional to the longitudinal resistivity ρ for an intrinsic and skew scattering contributions but is proportional to the square of such longitudinal resistivity for a side-jump contribution. And the spin Hall

angle being also the ratio of spin Hall resistivity over the charge or longitudinal resitivity, i.e. $\theta_{SHE} = \rho_{SHE}/\rho$. It is thus interesting to look for new alloy materials with strong spin-orbit coupling, where the longitudinal resistivity may be changed and therefore the spin Hall angle may be modulated. If skew scattering or intrinsic mechanism are dominant, then θ_{SHE} is independent of ρ, otherwise if side-jump mechanism is predominant, then $\theta_{SHE} \propto \rho$.

Independently of the value of the spin Hall angle, interfaces play also an important role in the injection of pure spin current from one layer to another due to the spin-flip scattering at the interfaces and spin resistance at the interfaces, historically called as spin memory loss (SML) [60]. The relevance of such SML effect in the correct qualification of spin Hall angle in materials was recently pointed out [61]**Erreur ! Signet non défini.**. One can optimize the spin Hall angle in a material, however its contribution to the spin injection could be strongly decreased by the interface. For example, in metallic-ferromagnetic/normal-metal (FM/NM) systems with large SML or poor transmission coefficient, part of the spin current injected from one layer to the other one will be lost at the interface.

1.5.4 Spin Orbit Torque

The spin current or spin accumulation generated by the SHE in a heavy metal (HM) or alloy with strong SOC could be exploited to manipulate the magnetization of an adjacent magnetic layer FM in a HM/FM bilayer.

The switching of the magnetization of a FM layer without another FM electrode exploiting spin-charge current conversion due to spin orbit coupling, was experimentally shown. This new phenomenon, called Spin Orbit Torque (SOT) has been proposed as an alternative for the STT-MRAM technology with the addition of even lower power consumption.

It was shown in FM/HM systems that the reversal of the magnetization occurs first by a magnetic domain nucleation followed by a domain wall propagation thanks to SHE and iDMI [62] [63] [64] [65] [66]. Therefore, because the spin currents can lead to the electrical control of magnetic and resistance states in spintronics nanostructures, it allows to switch the magnetization in a perpendicular magnetic (PMA) system [67] [68] [69]. Developing materials and engineering interfaces are still needed to exploit the SOT-SHE in order to reduce the critical current to switch the magnetization and consequently reduce the power consumption.

So far the electrical switching of the magnetization in a perpendicular magnetic system (PMA) was realized using layers with SHE properties such as Pt and Ta. Besides the different contributions to the SOT like iDMI [70] [71], it was experimentally shown that the key role to achieve such control on the magnetization reversal lies in the layer with strong spin-charge current conversion [72] [73].

1.5.4 Damping-like (DL) and field-like (FL) torques

The spin current injected from the HM into the FM layer has a spin polarization σ perpendicular to both J_S and J_C as displayed in Fig 1.12. This spin polarization σ leads to two symmetries on the torque exerted on the magnetization *M* of the FM layer: they are so-called DL and FL torques as displayed in 1.12. The relationship for both torques can be expressed as the last term in the following extended Landau-Lifshitz-Gilbert (LLG) equation:

$$\frac{\partial \hat{m}}{\partial t} = -\gamma \hat{m} \times \overrightarrow{H_{eff}} + \alpha \hat{m} \times \frac{\partial \hat{m}}{\partial t} + \gamma \frac{\hbar}{2e} \frac{J_c(t)}{\mu_0 M_S t_{FM}} \left(\xi_{DL}^{eff} (\hat{m} \times \hat{\sigma} \times \hat{m}) + \xi_{FL}^{eff} (\hat{m} \times \hat{\sigma}) \right) \quad (1.15)$$

where the effective field H_{eff} includes any applied field, H_{app} and the anisotropies field. The SHE can contribute to both torques. There are also other effects that generate spin accumulation due to SOC, such as the Rashba interfaces and topological insulators, and, in similar way, they can contribute with both symmetries to the torque on magnetization M. The dimensionless parameters ξ_{DL}^{eff} and ξ_{FL}^{eff} represent the effective efficiency of the charge-to-spin current conversion (i.e; convoluted with loss or transparency at the interface). Hence, the parameter ξ_{DL}^{eff} is indeed the efficient spin Hall angle of the HM layer in the HM/FM structure. The last term has the same form as the first term in the LLG equation and induces a precession of the magnetization if $H_{eff} \| \sigma$, that explains the name of the torque as field-like. The damping-like term has a double cross product and also acts perpendicular to the magnetization as the second term in the LLG equation where the damping constant α is shown. That is the reason why this term is called damping-like torque.

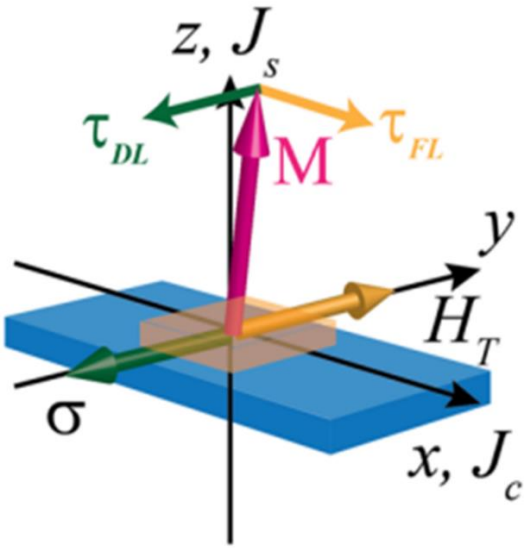

Figure 1.12: *Schematic of the DL and FL torques due to SHE of heavy metal (blue strip) acting on a magnetic layer (orange). The in-plane applied field, H_{app} , is collinear with in-plane charge current. From* [74]

In order to get the SHE-SOT or current-induced magnetization switching ,still a small in-plane external field, H_x, is needed. This is to break the symmetry in a macrospin model or to overcome the effective field due to iDMI (after a nucleation and to favor the right propagation of domain walls) [62] [75]. Kyung-Jin Lee and coworkers developed the expression to account for the critical current needed to obtain the magnetization switching considering the effective spin Hall angle and the in-plane external magnetic field [75]. It reads:

$$J_{C,perp}^{SH} = \frac{2e}{\hbar}\frac{M_S t_F}{\theta_{SH}}\left(\frac{H_{K,eff}}{2} - \frac{H_x}{\sqrt{2}}\right) \qquad (1.16)$$

$$J_{switch} \approx \frac{2e}{\hbar}\frac{t_F}{\theta_{SHE}^{eff}}\left(K_{eff} - \frac{\mu_0 H_x M}{\sqrt{2}}\right) \qquad (1.17)$$

Field-free magnetization switching is possible by using wedge to induced an in-plane effective anisotropy [76], exchange-bias [77] [78] or interlayer exchange coupling [79].

1.6 All Optical Switching

The group of Theo Rasing in Nijmegen has been the first group to demonstrate that it is possible to switch the local magnetization using only femtosecond polarized light as shown in

ref. [80] This is called all optical switching (AOS). There are two types of AOS: all optical helicity-dependent switching (AO-HDS) and all optical helicity-independent switching (AO-HIS). We will focus on AO-HDS which was first observed on a 20 nm thick $Gd_{22}Fe_{74}.6Co_{3.4}$ showing domain patterned using a Faraday microscope as seen on figure 1.13. The black domains are magnetized along $-\vec{z}$ while the white domains are magnetized along $+\vec{z}$. Using different circularly polarization light the magnetization can be switch in one direction or the other. Using σ+ (resp. σ-) helicity they have been able to set the magnetization along $+\vec{z}$ (resp. $-\vec{z}$). This helicity dependent switching of the light is called AO-HDS (All Optical Helicity Dependent Switching). Sweeping with a linearly polarized light they obtained a mix of both types of domains.

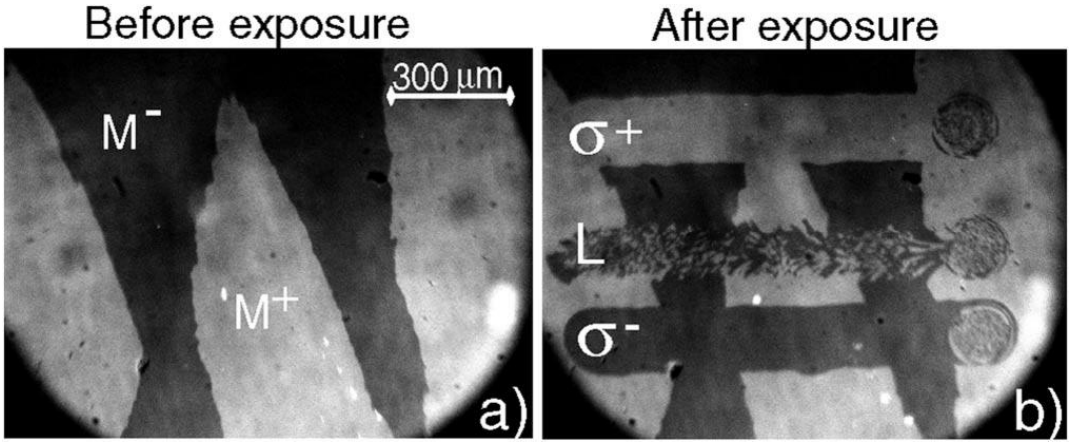

Figure 1.13: *Faraday image of a 20 nm thick $Gd_{22}Fe_{74}.6Co_{3.4}$ with dark contrast standing for positive magnetization and clear contrast for negative magnetization. (a) Image of the initial multidomain state. (b) Image obtain after sweeping of left, right and linear polarized light with a speed around 30 µm/s and a fluence of 11.4 mJ/cm^2. Extracted from* [80].

References

[1] J. Coey, «Magnetism and magnetic materials,» *Cambride University Press,* 2010.

[2] A. P. Guimaraes, «Principles of Nanomagnetism,» *Springer,* 2009.

[3] I. E. Dzyaloshinskii, «Thermodynamic theory of weak ferromagnetism in antiferromagnetic substances,» *Sov. Phys. JETP,* vol. 5, p. 1259–1272, 1957.

[4] T. Moriya, «Anisotropic superexchange interaction and weak ferromagnetism.,» *Phys. Rev.,* vol. 120, p. 91–98, 1960.

[5] A. Fert, V. Cros and J. Sampaio, "Skyrmions on the track," *Nature Nanotechnology,* vol. 8, p. 152–156, 2013.

[6] M. N. Baibich, J. M. Broto, A. Fert, F. N. Van Dau, F. Petroff, P. Etienne, G. Creuzet, A. Friederich and J. Chazelas, "Giant Magnetoresistance of (001)Fe/(001)Cr Magnetic Superlattices," *Phys. Rev. Lett.,* vol. 61, p. 2472, 1988.

[7] S. Uran, M. Grimsditch, E. E. Fullerton and S. D. Bader, "Infrared spectra of giant magnetoresistance Fe/Cr/Fe trilayers," *Phys. Rev. B,* vol. 57, p. 2705, 1998.

[8] A. Fert and F. N. Van Dau, "Spintronics, from giant magnetoresistance to magnetic skyrmions and topological insulators," *Comptes Rendus Physique,* vol. 20, pp. 817-831, 2019.

[9] N. F. Mott, "The electrical conductivity of transition metals," *Proceedings of the Royal Society A,* vol. 153(880), pp. 699-717, 1936.

[10] A. Fert and I. A. Campbell, "Two-Current Conduction in Nickel," *Phys. Rev. Lett.,* vol. 21, p. 1190, 1968.

[11] A. Fert and I. Campbell, "Transport properties of ferromagnetic transition metals," *Journal de Physique Colloques,* vol. 32(C1), pp. C1-46-C1-50, 1971.

[12] A. Fert and I. A. Campbell, "Electrical resistivity of ferromagnetic nickel and iron based alloys," *J. Phys. F, Met. Phys.,* vol. 6(5), p. 849–871, 1976.

[13] J. M. De Teresa, A. Barthélémy, A. Fert, J. P. Contour, F. Montaigne and P. Seneor, "Role of Metal-Oxide Interface in Determining the Spin Polarization of Magnetic Tunnel Junctions," *Science,* vol. 286(5439), pp. 507-509, 1999.

[14] C. Chappert, A. Fert and F. N. Van Dau, "The emergence of spin electronics in data storage," *Nature Mater.,* vol. 6(11), pp. 813-23, 2007.

[15] Y. M. Lee, J. Hayakawa, S. Ikeda, F. Matsukura and H. Ohno, *Appl. Phys. Lett.,* vol. 90, p. 212507, 2007.

[16] A. Fert, "Nobel Lecture: Origin, development, and future of spintronics," *Rev. Mod. Phys.,* vol. 80, p. 1517, 2008.

[17] J. Slonczewski, "Current-driven excitation of magnetic multilayers," *J. Magn. Magn. Mater.,* vol. 159(1–2), p. L1–L7, 1996.

[18] L. Berger, "Emission of spin waves by a magnetic multilayer traversed by a current," *Phys. Rev. B,* vol. 54(13), p. 9353–9358, 1996.

[19] M. Hosomi, H. Yamagishi, T. Yamamoto, K. Bessho, Y. Higo, K. Yamane, H. Yamada, M. Shoji, H. Hachino, C. Fukumoto, H. Nagao and H. Kano, "A novel nonvolatile memory with spin torque transfer magnetization switching," *IEEE International Electron Devices Meeting, IEDM Technical Digest.,* p. 459–462, 2005.

[20] "Everspin ships first ST-MRAM memory with 500 × performance of flash | Computerworld, [Online]".

[21] J. C. Slonczewski, "Current-driven excitation of magnetic multilayers," *J. Magn. Magn. Mater.,* vol. 159, p. L1–L7, 1996.

[22] L. Berger, "Emission of spin waves by a magnetic multilayer traversed by a current," *Phys. Rev. B,* vol. 54(13), p. 9353–9358, 1996.

[23] H. Kubota, A. Fukushima, Y. Ootani, S. Yuasa, K. Ando, H. Maehara, K. Tsunekawa, D. D. Djayaprawira, N. Watanabe and Y. Suzuki, "Evaluation of Spin-Transfer Switching in CoFeB/MgO/CoFeB Magnetic Tunnel Junctions," *Japanese Journal of Applied Physics,* vol. 44(9L), p. L1237, 2005.

[24] J. E. Hirsch, *Phys. Rev. Lett.,* vol. 83, p. 1834, 1999.

[25] S. Maekawa, S. O. Valenzuela, E. Saitoh and T. Kimura, "Spin Current," *Oxford University Press,* 2012.

[26] G. E. Bauer, E. Saitoh and B. J. v. Wees, *Nat. Mat.,* vol. 11(5), pp. 391-399, 2012.

[27] Y. Tserkovnyak, A. Brataas and G. E. Bauer, *Phys. Rev. Lett.,* vol. 88, p. 117601, 2002.

[28] Y. Bychkov and E. I. Rashba, *JETP Lett.,* vol. 39(78), 1984.

[29] J. C. Rojas Sánchez, L. Vila, G. Desfonds, S. Gambarelli, J. P. Attané, J. M. D. Teresa, C. Magén and A. Fert, "Spin-to-charge conversion using Rashba coupling at the interface between non-magnetic materials," *Nature Communications,* vol. 4(1), pp. 1-7, 2013.

[30] A. Hoffmann, "Spin Hall effects in metals," *IEEE Trans. on Magn.,* vol. 49(10), pp. 5172-5193, 2013.

[31] J.Sinova, S. O. Valenzuela, J. Wunderlich, C. Back and T. Jungwirth, "Spin Hall effects," *Rev. Mod. Phys.,* vol. 87, p. 1213, 2015.

[32] M. Dyakonov and V. I. Perel, *Phys. Lett. A,* vol. 35, p. 459, 1971.

[33] J. Sinova, D. Culcer, N. A. S. Q. Niu, T. Jungwirth and A. H. MacDonald, "Universal Intrinsic Spin Hall Effect," *Phys. Rev. Lett.,* vol. 92, p. 126603, 2004.

[34] Y. Kato, R. Myers, A. Gossard and D. Awschalom, "Observation of the spin Hall effect in semiconductors," *Science,* vol. 306 (5703), p. 1910–1913, 2004.

[35] K. Ando, S. Takahashi, J. Ieda, H. Kurebayashi, T. Trypiniotis, C. H. W. Barnes, S. Maekawa and E. Saitoh, "Electrically tunable spin injector free from the impedance mismatch problem," *Nature Materials,* vol. 10, pp. 655-659, 2011.

[36] K. Ando and E. Saitoh, "Observation of the inverse spin Hall effect in silicon," *Nature Communications,* vol. 3, 2012.

[37] M. Koike, Y. Kamimuta and T. Tezuka, "Modulation of NiGe/Ge Schottky barrier height by S and P co-introduction," *Appl. Phys. Lett.,* vol. 102(3), p. 032108, 2013.

[38] J.-C. Rojas-Sánchez, M. Cubukcu, A. Jain, C. Vergnaud, C. Portemont, C. Ducruet, A. Barski, A. Marty, L. Vila, J.-P. Attané, E. Augendre, G. Desfonds, S. Gambarelli, H. Jaffrès, J.-M. George and M. Jamet, "Spin pumping and inverse spin Hall effect in germanium," *Phys. Rev. B,* vol. 88, p. 064403, 2013.

[39] A. Jain, J.-C. Rojas-Sanchez, M. Cubukcu, J. Peiro, J. C. L. Breton, E. Prestat, C. Vergnaud, L. Louahadj, C. Portemont, C. Ducruet, V. Baltz, A. Barski, P. Bayle-Guillemaud, L. Vila, J.-P. Attané, E. Augendre, G. Desfonds, S. Gambarelli, H. Jaffrès, J.-M. George and M. Jamet, "Crossover from Spin Accumulation into Interface States to Spin Injection in the Germanium Conduction Band," *Phys. Rev. Lett.,* vol. 109, p. 106603, 2012.

[40] A. Jain, J.-C. Rojas-Sanchez, M. Cubukcu, J. Peiro, J.-C. Le Breton, C. Vergnaud, E. Augendre, L. Vila, J.-P. Attané, S. Gambarelli, H. Jaffrès, J.-M. George and M. Jamet, "Transition from spin accumulation into interface states to spin injection in silicon and germanium conduction bands," *The European Physical Journal B,* vol. 86(4), p. 140, 2013.

[41] S. O. Valenzuela and M. Tinkham, "Direct electronic measurement of the spin Hall effect," *Nature ,* vol. 442, p. 176–17, 2006.

[42] L. Vila, T. Kimura and Y. Otani, "Evolution of the Spin Hall Effect in Pt Nanowires: Size and Temperature Effects," *Phys. Rev. Lett.,* vol. 99, p. 226604, 2007.

[43] K. Ando, S. Takahashi, J. Ieda, Y. Kajiwara, H. Nakayama, T. Yoshino, K. Harii, Y. Fujikawa, M. Matsuo, S. Maekawa and E. Saitoh, "Inverse spin-Hall effect induced by spin pumping in metallic system," *Journal of Applied Physics,* vol. 109, p. 103913, 2011.

[44] O. Mosendz, V. Vlaminck, J. E. Pearson, F. Y. Fradin, G. E. W. Bauer, S. D. Bader and A. Hoffmann, "Detection and quantification of inverse spin Hall effect from spin pumping in permalloy/normal metal bilayers," *Phys. Rev. B,* vol. 82, p. 214403, 2010.

[45] A. Azevedo, L. H. Vilela-Leão, R. L. Rodríguez-Suárez, A. F. L. Santos and S. M. Rezende, "Spin pumping and anisotropic magnetoresistance voltages in magnetic bilayers: Theory and experiment," *Phys. Rev. B,* vol. 83, p. 144402, 2011.

[46] K. Ando and E. Saitoh, "Inverse spin-Hall effect in palladium at room temperature," *Journal of Applied Physics,* vol. 108, p. 113925, 2010.

[47] C. Hahn, G. d. Loubens, O. Klein, M. Viret, V. V. Naletov and J. B. Youssef, "Comparative measurements of inverse spin Hall effects and magnetoresistance in YIG/Pt and YIG/Ta," *Phys. Rev. B,* vol. 87, p. 174417, 2013.

[48] J. E. Gómez, B. Zerai Tedlla, N. R. Álvarez, G. Alejandro, E. Goovaerts and A. Butera, "Spin transport parameters in Ni80Fe20/Ru and Ni80Fe20/Ta bilayers," *Phys. Rev. B,* vol. 90, p. 184401, 2014.

[49] P. C.-F., L. Liu, H. W. T. Y. Li, D. C. Ralph and R. A. Buhrman, "Spin transfer torque devices utilizing the giant spin Hall effect of tungsten," *Appl. Phys. Lett.,* vol. 101, p. 122404, 2012.

[50] A.Fert, A.Friederich and A.Hamzic, "Hall effect in dilute magnetic alloys," *J. Magn. Magn. Mater. ,* vol. 24(3), pp. 231-257, 1981.

[51] A. Fert and P. M. Levy, "Spin Hall Effect Induced by Resonant Scattering on Impurities in Metals," *Phys. Rev. Lett.,* vol. 106, p. 157208, 2013.

[52] Y. Niimi, M. Morota, D. H. Wei, C. Deranlot, M. Basletic, A. Hamzic, A. Fert and Y. Otani, "Extrinsic Spin Hall Effect Induced by Iridium Impurities in Copper," *Phys. Rev. Lett.,* vol. 106, p. 126601, 2011.

[53] Y. Niimi, Y. Kawanishi, D. H. Wei, C. Deranlot, H. X. Yang, M. Chshiev, T. Valet, A. Fert and Y. Otani, "Giant Spin Hall Effect Induced by Skew Scattering from Bismuth Impurities inside Thin Film CuBi Alloys," *Phys. Rev. Lett.,* vol. 109, p. 156602, 2012.

[54] Y. Niimi, H. Suzuki, Y. Kawanishi, Y. Omori, T. Valet, A. Fert and Y. Otani, "Extrinsic spin Hall effects measured with lateral spin valve structures," *Phys. Rev. B,* vol. 89, p. 054401, 2014.

[55] P. Laczkowski, J.-C. Rojas-Sánchez, W. Savero-Torres, H. Jaffrès, N. Reyren, C. Deranlot, L. Notin, C. Beigné, A. Marty, J.-P. Attané, L. Vila, J.-M. George and A. Fert, "Experimental evidences of a large extrinsic spin Hall effect in AuW alloy," *Appl. Phys. Lett.,* vol. 104, p. 142403, 2014.

[56] Y. Niimi and Y. Otani, "Reciprocal spin Hall effects in conductors with strong spin–orbit coupling: a review," *Reports on Progress in Physics,* vol. 78(12), 2015.

[57] N. Nagaosa, J. Sinova, S. Onoda, A. H. MacDonald and N. P. Ong, "Anomalous Hall effect," *Rev. Mod. Phys.,* vol. 82, p. 1539, 2010.

[58] J. Inoue and H. Ohno, "Taking the Hall Effect for a Spin," *Science,* vol. 309(5473), pp. 2004-2005, 2005.

[59] M. Gradhand, D. V. Fedorov, P. Zahn and I. Mertig, "Spin Hall angle versus spin diffusion length: Tailored by impurities," *Phys. Rev. B,* vol. 81, p. 245109, 2010.

[60] J. Bass and W. P. Pratt Jr, "Spin-diffusion lengths in metals and alloys, and spin-flipping at metal/metal interfaces: an experimentalist's critical review," *J. Phys. Condens. Matter,* vol. 19(18), p. 183201, 2007.

[61] J.-C. Rojas-Sánchez, N. Reyren, P. Laczkowski, W. Savero, J.-P. Attané, C. Deranlot, M. Jamet, J.-M. George, L. Vila and H. Jaffrès, "Spin Pumping and Inverse Spin Hall Effect in Platinum: The Essential Role of Spin-Memory Loss at Metallic Interfaces," *Phys. Rev. Lett.,* vol. 112, p. 106602, 2014.

[62] J. C. Rojas-Sánchez, P. Laczkowski, J. Sampaio, S. Collin, K. Bouzehouane, N. Reyren, H. Jaffrès, A. Mougin and J. M. George, "Perpendicular magnetization reversal in Pt/[Co/Ni]3/Al multilayers via the spin Hall effect of Pt," *Appl. Phys. Lett.,* vol. 108, p. 08240, 2016.

[63] O. J. Lee, L. Q. Liu, C. F. Pai, Y. Li, H. W. Tseng, P. G. Gowtham, J. P. Park, D. C. Ralph and R. a. Buhrman, "Central role of domain wall depinning for perpendicular magnetization switching driven by spin torque from the spin Hall effect," *Phys. Rev. B,* vol. 89, p. 024418, 2014.

[64] C. F. Pai, M. Mann, A. J. Tan and G. S. D. Beach, "Determination of spin torque efficiencies in heterostructures with perpendicular magnetic anisotropy," *Phys. Rev. B,* vol. 93, p. 144409, 2016.

[65] N. Mikuszeit, O. Boulle, I. M. Miron, K. Garello, P. Gambardella, G. Gaudin and L. D. Buda-Prejbeanu, "Spin-orbit torque driven chiral magnetization reversal in ultrathin nanostructures," *Phys. Rev. B,* vol. 92, p. 144424, 2015.

[66] M. Baumgartner, K. Garello, J. Mendil, C. O. Avci, E. Grimaldi, C. Murer, J. Feng, M. Gabureac, C. Stamm, Y. Acremann, S. Finizio, S. Wintz, J. Raabe and P. Gambardella, "Spatially and time-resolved magnetization dynamics driven by spin–orbit torques," *Nat. Nanotechnol.,* vol. 12, p. 980, 2017.

[67] I. M. Miron, G. Gaudin, S. Auffret, B. Rodmacq, A. Schuhl, S. Pizzini, J. Vogel and P. Gambardella, "Current-driven spin torque induced by the Rashba effect in a ferromagnetic metal layer," *Nat. Mater.,* vol. 9, p. 230, 2010.

[68] I. M. Miron, K. Garello, G. Gaudin, P.-J. Zermatten, M. V. Costache, S. Auffret, S. Bandiera, B. Rodmacq, A. Schuhl and P. Gambardella, "Perpendicular switching of a single ferromagnetic layer induced by in-plane current injection," *Nature,* vol. 476, p. 189, 2011.

[69] L. Liu, C.-F. Pai, Y. Li, H. W. Tseng, D. C. Ralph and R. A. Buhrman, "Spin-Torque Switching with the Giant Spin Hall Effect of Tantalum," *Science,* vol. 336(6081), pp. 555-558, 2012.

[70] A. Thiaville, S. Rohart, É. Jué, V. Cros and A. Fert, "Dynamics of Dzyaloshinskii domain walls in ultrathin magnetic films," *Europhysics Letters,* vol. 100(5), p. 57002, 2012.

[71] A. V. Khvalkovskiy, V. Cros, D. Apalkov, V. Nikitin, M. Krounbi, K. A. Zvezdin, A. Anane, J. Grollier and A. Fert, "Matching domain-wall configuration and spin-orbit torques for efficient domain-wall motion," *Phys. Rev. B*, vol. 87, p. 020402, 2013.

[72] S. Emori, U. Bauer, S.-M. Ahn, E. Martinez and G. S. D. Beach, "Current-driven dynamics of chiral ferromagnetic domain walls," *Nature Materials*, vol. 12, p. 611–616, 2013.

[73] J. Torrejon, J. Kim, J. Sinha, S. Mitani, M. Hayashi, M. Yamanouchi and H. Ohno, "Interface control of the magnetic chirality in CoFeB/MgO heterostructures with heavy-metal underlayers," *Nature Communications*, vol. 5(1), pp. 1-8, 2014.

[74] J. Park, G. E. Rowlands, O. J. Lee, D. C. Ralph and R. A. Buhrman1, "Macrospin modeling of sub-ns pulse switching of perpendicularly magnetized free layer via spin-orbit torques for cryogenic memory applications," *Appl. Phys. Lett.*, vol. 105, p. 102404, 2014.

[75] K.-S. Lee, S.-W. Lee, B.-C. Min and K.-J. Lee, "Threshold current for switching of a perpendicular magnetic layer induced by spin Hall effect," *Appl. Phys. Lett.*, vol. 102, p. 112410, 2013.

[76] T.-Y. Chen, H.-I. Chan, W.-B. Liao and C.-F. Pai, "Current-Induced Spin-Orbit Torque and Field-Free Switching in Mo-Based Magnetic Heterostructures," *PHYSICAL REVIEW APPLIED*, vol. 10, p. 044038, 2018.

[77] S. A. Razavi, D. Wu, G. Yu, Y.-C. Lau, K. L. Wong, W. Zhu and C. He, "Joule Heating Effect on Field-Free Magnetization Switching by Spin-Orbit Torque in Exchange-Biased Systems," *PHYSICAL REVIEW APPLIED*, vol. 7, p. 024023, 2017.

[78] A. van den Brink, G. Vermijs, A. Solignac, J. Koo, J. Kohlhepp, H. Swagten and B. Koopmans, "Field-free magnetization reversal by spin-Hall effect and exchange bias," *Nature Communications*, vol. 7(1), pp. 1-6, 2016.

[79] Y.-C. Lau, D. Betto, K. Rode, J. M. D. Coey and P. Stamenov, "Spin–orbit torque switching without an external field using interlayer exchange coupling," *Nature Nanotechnology*, vol. 11(9), p. 758, 2016.

[80] C. D. Stanciu, F. Hansteen, A. V. Kimel, A. Kirilyuk, A. Tsukamoto, A. Itoh and T. Rasing, "All-Optical Magnetic Recording with Circularly Polarized Light," *Phys. Rev. Lett.*, vol. 99, p. 047601, 2007.

Chapitre II

Résumé

Dans ce chapitre je décris les principaux dispositifs et méthodes expérimentales que j'ai utilisé pendant ma thèse : les dépôt des couches minces, les magnétomètres, les techniques de lithographie et le dispositif pour les mesures de transport.

Summary

In this chapter we present the main experimental tools I used along my Ph. D. These include the growing technique (DC magnetron sputtering), methods for magnetometry (SQUID-VSM), methods to study the magnetization orientation of thin films, methods to pattern the desirable devices (UV lithography process) and magneto-transport set-ups.

Chapter II

Experimental methods and samples

2.1 Thin film deposition by DC magnetron sputtering

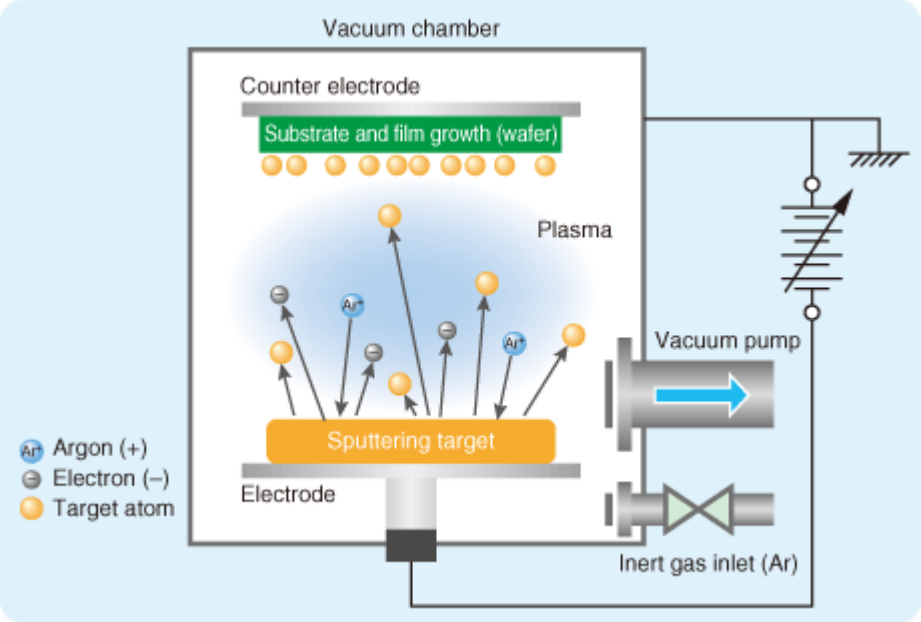

Figure 2.1: *Schematic representation of DC Magnetron sputtering process*

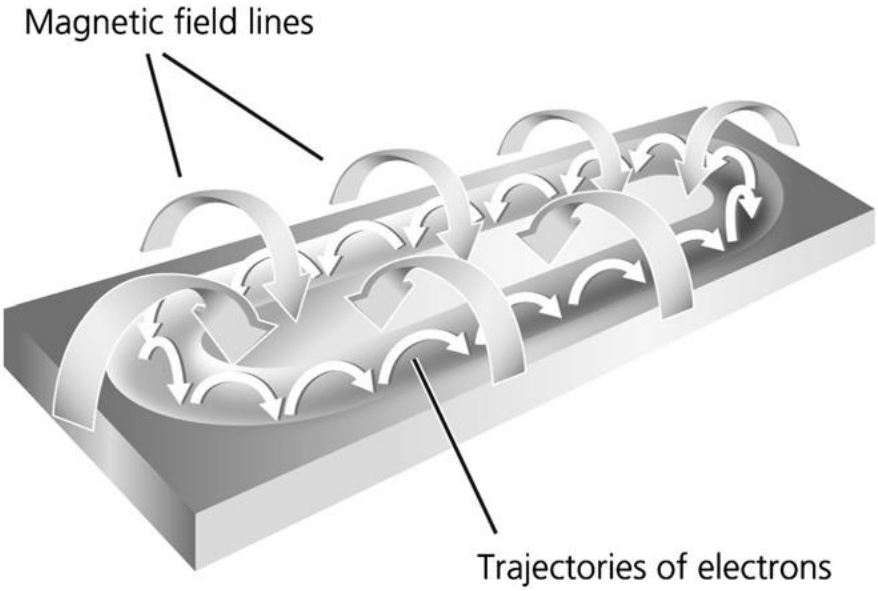

Figure 2.2: *The principle of magnetron sputtering. Electrons are trapped by the Lorentz force* $K = e(v \times B)$ *in an inhomogeneous magnetic field, resulting in an enhanced ionisation of argon atoms.*

Basic description of sputtering process

The basic principle of sputtering is presented in figure 2.1. In the sputtering process, argons atoms are injected into an high vacuum chamber. A high voltage is applied between the target (or cathode) and a substrate. The energetic Ar^+ ions in glow discharge plasma bombard the target material. The bombardment process causes the removal, i.e., "sputtering", of target atoms, which then condense on the substrate as a thin film. The ion bombardment also results in the emission of secondary electrons which play an important role in maintaining the plasma. The basic sputtering process has some limitation such as low deposition rate, low ionization efficiencies in the plasma and high substrate heating effects. A typical solution for this problem is the development of magnetrong sputtering.

The role of magnetron

Figure 2.2 visualized the role of the magnetron. Magnetrons utilizes of the fact that a magnetic field configured parallel to the target surface can constrain secondary electron motion to the vicinity of the target. The magnets are arranged in a way that one pole is positioned at the central axis of the target and the second pole is formed by a ring of magnets around the outer edge of the target. The electrons are trapped that leds to significantly increase of the probability of ionizing electron-atom collision. The result of high ionization efficiency is a dense plasma in the target region, which leads to increased bombardment of the target. Thus, higher sputtering rates and therefore higher deposition rates at the substrate can be obtained. Moreover, the increased ionization efficiency in the magnetron mode allows the discharge to be maintained at lower operating pressures (typically, 10^{-3} mbar, compared to 10^{-2} mbar) and lower operating voltages (typically 500V compared to 2 to 3kV) than is required in the basic sputtering mode.

Elaboration of alloys by co-sputtering:

In the case of co-sputtering, the magnetron sputtering of several targets is performed at the same time. Therefore, atoms of several species are ejected towards a substrate on which they form the desired alloy. The main concerns about the materials that are grown by this method are the deposition rate and the atomic composition of the layers.

Let us determine the deposition rate in terms of thickness per deposition time. In order to determine that, we have to know first the thickness deposition rate of each material deposited. This can be achieved by growing calibration samples, at a given set of conditions concerning the argon flux and pressure, and varying the power applied to the target. Usually, whether a DC

or RF deposition is performed, a linear dependence between the deposition rate and the working power applied to the cathode is found. Let us note $v_i(P_i)$ the deposition rate of the ith target (which is a linear function of the power applied to this target P_i). This quantity can be expressed in units of nanometers per second. Let us convert this into a molar rate. In order to do so, we use the molar volume of the species studied, that we note as ρ_i, which is expressed in units of m^3/mol. We can thus express the ratio $\frac{v_i(P_i)}{\rho_i} = \tau_i(P_i)$ that can be expressed in mol.m²/sec. This quantity corresponds to the molar deposition rate per surface. By stating the previous sentence, we make an approximation considering that the calibration samples are composed of a perfect monocrystal of the material considered.

In order to tune the stoichiometry of the alloy chosen, by calling x_i the molar proportion of the ith component, we have to solve the linear system:

$$\frac{\tau_i(P_i)}{\sum_j \tau_j\,(P_j)} = x_i \;\forall i \qquad (2.1)$$

If we call *n* the number of materials used, this system has *n* degrees of freedom, and has n-1 constraints since the implicit condition $\sum x_i = 1$, that is a data of the problem, lets one of the equations of Eq. (2.1) be useless. Therefore, the choice on one applied power determines all the others. Since the power applied to each cathode can be tuned continuously, the choice made is often to have values of the power that are not too large, in order to prevent the heating of the materials targets, but also not too low, so that the linear dependence between the applied power and the deposition rate still holds.

In order to obtain the thickness deposition rate of the alloy, we use again the assumption that the materials grown in the alloy have the same volume parameters as when they are grown separately in a perfect crystal. The thickness deposition rate is thus the simple sum of the thickness rates of each material at the power considered for each cathode. We can express the thickness deposition as:

$$v_{alloy} = \sum_i v_i(P_i) \qquad (2.2)$$

In the special case of CoTb alloys that is of great interest to us, let us explicit these equations. The thickness deposition rates can be expressed as:

$$\begin{cases} v_{Co}(P_{Co}) = a_{Co}P_{Co} + b_{Co} \\ v_{Tb}(P_{Tb}) = a_{Tb}P_{Tb} + b_{Tb} \end{cases} \qquad (2.3)$$

The molar deposition rate of each material can thus be written as:

$$\begin{cases} \tau_{Co}(P_{Co}) = \dfrac{a_{Co}}{\rho_{Co}} P_{Co} + \dfrac{b_{Co}}{\rho_{Co}} \\ \tau_{Tb}(P_{Tb}) = \dfrac{a_{Tb}}{\rho_{Tb}} P_{Tb} + \dfrac{b_{Tb}}{\rho_{Tb}} \end{cases} \qquad (2.4)$$

Let us note $a_x^* = \frac{a_x}{\rho_x}$ and $b_x^* = \frac{b_x}{\rho_x}$ where x= Co, Tb. By using the fact that $x_{Tb} = 1 - x_{Co}$, we see that the system Eq. (2.1) is the equivalent to the sole equation:

$$P_{Tb} = \left((a_{Co}^* P_{Co} + b_{Co}^*) \frac{(1 - x_{Co})}{x_{Co}} - b_{Tb}^* \right) \Big/ a_{Tb}^* \qquad (2.5)$$

We can then choose the power applied to the cobalt target as we wish, and compute easily the corresponding terbium power. If the power applied to the terbium is more sensitive, we can inverse the relationship Eq. 2.5 by switching the indices Co and Tb, since all the problem is symmetric with respect to the materials.

2.2 Vibrating Sample Magnetometry (VSM)

Vibrating Sample Magnetometry (VSM) is a direct magnetic measuring technique that allow to determine the magnetic moment and other magnetic parameters of a sample with high precision. The invention of this technique dates back to 1950s by Simon Foner in MIT. Since its introduction till now, VSM is popular thanks to many advantages of accuracy, versatility and ease of use. The essential set up of VSM is described in figure 2.3.

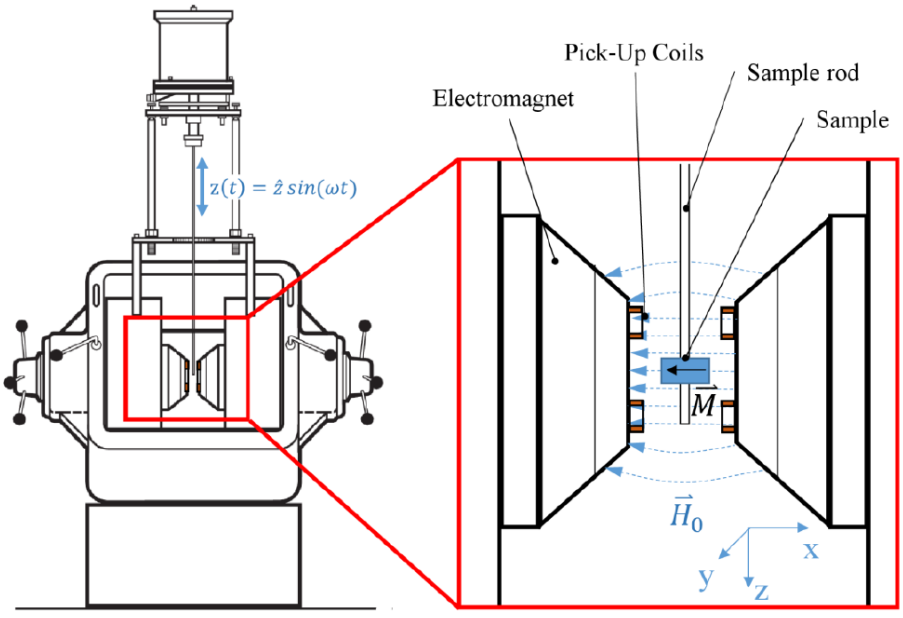

Figure 2.3: *Schematic representation of a VSM*

The principle of VSM is based on Faraday's law of induction which states that a change in flux through a coil will generate an electromagnetic force in the coil. In the measurement set up, the sample is attached to a nonmagnetic rod, which is vibrates in a gap between pick-up coils at a known frequency, usually between 50 and 100Hz, and at a fixed amplitude, typically 1-3 mm. The stray magnetic field arising from the magnetized sample moves together with the sample, thus induces a varying magnetic flux in the coils. The voltage generated by this varying magnetic flux in the coils is proportional to the magnetic moment, providing the way to read it. The VSM set up requires signal processing using a lock-in amplifier to obtain high signal-to-noise ratios. The pickup coils are desisned to ensure a linear response over the length of vibration and eliminate the signal from the applied dc field. In order to provide reliable measurement, the instrument requires calibration of the absolute scale of magnetization and the corresponding voltage by using a reference sample.

2.3 Lithography process

After the deposition with magnetron sputtering, our thin films were patterned into devices of different geometries (lines, Hall crosses or double Hall crosses) using optical lithography. For that, we took advantage of the common MiNaLor cleanroom platform (platform for micro and nano technology of Lorraine).

We have used lateral dimensions spanning from width of 20 µm down to 2 µm. So, UV lithography was sufficiently precise to achieve such dimensions. We have used two lithography steps for the whole process, which are:

a) **Etching of the thin film using the photoresist as hard mask**. This step involves the following sub-steps:
    - Put the positive photosensitive resist Microdeposit Shipley 1813 (s1813) on the sample (Fig. 2.4a)
    - spread uniformly the resist on the sample by spinning it at 10000 RPM during 40 seconds.
    - Baking it at 115°C during 1 minute. The last two steps are known as a spin coating (Fig. 2.4b)
    - Expose UV light through the mask (Fig. 2.4c). The UV wave length is 365 nm. We used a power of about 240 W using the appropriate mask (that we called

SOT1) over a period of 20 seconds in *vacuum contact mode*. A SUSS MicroTec Mask Aligner MJB4 was used.

- develop the resist (Fig. 2.4d). The sample is placed in MF319 developer for 40 to 45 seconds, and then rinsed in double de-ionized water for 30 seconds.
- The quality of the above steps is verified by the observation in an optical microscope, where lateral dimensions can be measured and pictures can be taken.
- the sample is then fixed in a holder and placed in a pre-chamber of an Ion Beam Etch machine (4Wave).
  - Here we use Ar inert gas which is ionized to etch the material of our thin films until the substrate (SiO_2) in our case (Fig. 2.4e).
  - Typical values of etching process are: Voltage beam= 200V, current beam= 50 mA, sample voltage = 60V, etching angle =10 degree. The sample is continuously rotated to homogenize the etching.
  - The etching is followed in situ by chemical detection using Secondary-ion mass spectrometry (SIMS).
  - Typical etching time for a W(3 nm/CoTb(3.5 nm)/AlOx (3 nm) is about 750 seconds with the parameters mentioned.
  - It is important not to over-etch the films in order to keep the SiO_2 substrate (Fig. 2.4 f) which works as a barrier to avoid a shunting into Si during the magneto-transport experiments.
- Remove the remaining photoresist (Fig. 2.4g). Now the sample is patterned into the suitable geometries but there are regions still covered by the s1813 photoresist. We can remove this photoresist by placing the sample in an acetone beaker during several hours followed by a few minutes (3 to 5) in ultrasound bath. Finally, the sample is cleaned with isopropanol and dried with Ar flow. It is important to check in a microscope the quality of the sample and to look if the photoresist was well removed from the devices.
- Sometimes, the last step doesn't work well to remove the resist. Then some alternatives might be used, depending on the materials. These could be O_2 plasma, UV irradiation (without mask) and developer, or remover 1165 at 80°C during 30 to 40 minutes.

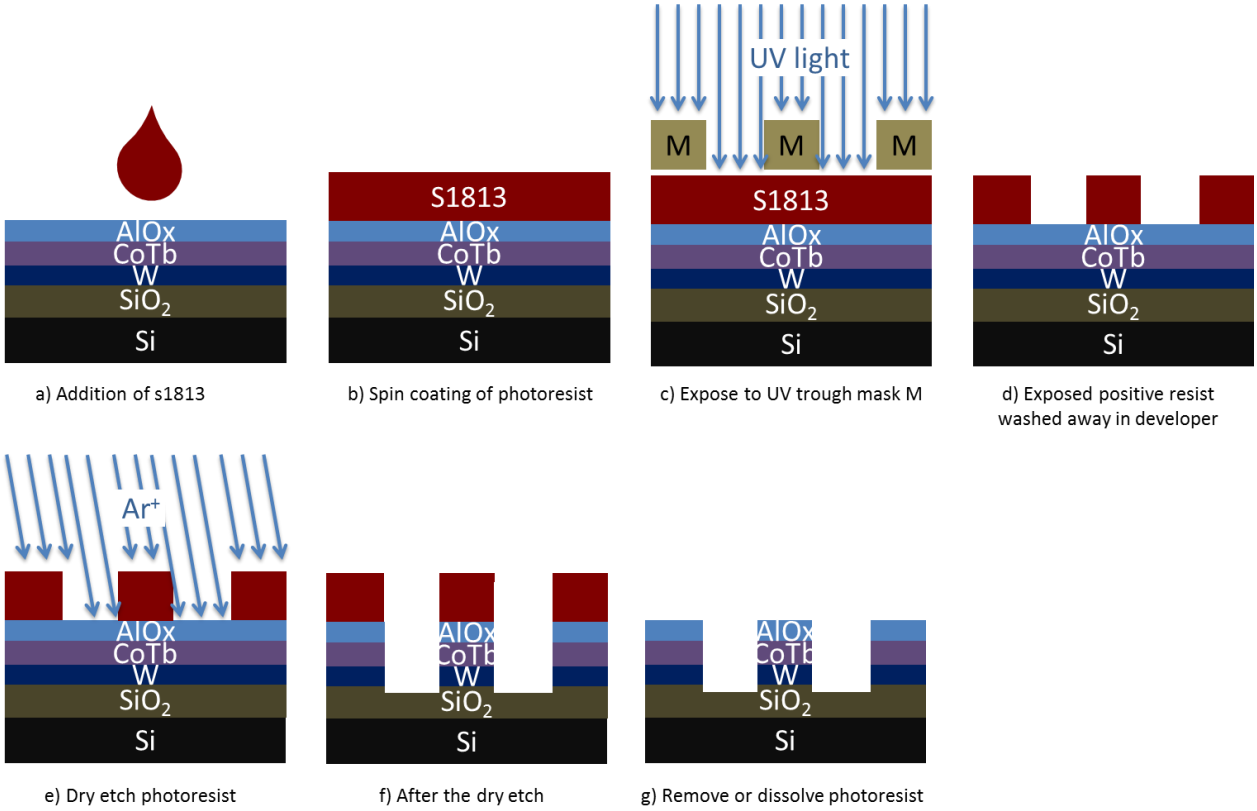

Figure 2.4: *Schematic of etching process by UV lithography used in my PhD.*

b) **Lift-off of Ti/Au (Figure 2.5)**. After having successfully achieved the previous stage, it is now necessary to deposit electrodes or relatively large ohmic contacts in order to make the macroscopic contacts. These contacts are necessary to perform transport measurements later. This lift-off step involves the following sub-steps:

- To improve the adherence and facilitate the lifting of the photoresist, a primer is spin coated on the sample: spinning speed is 7000 RPM for 40 seconds, followed by a bake at 115° for one minute.
- Then the Spin coating of LOR3A photoresist. LOR3A is spinned at 7000 RPM for 40 seconds and baking at 140 °C for two minutes.
- Now the spin coating of the positive s1813 photoresist as previously used in the etching process. Spinning at 10000 RPM and baking at 115°C for one minute.
- Expose to UV trough mask. Now the suitable mask is SOT2 using the same MJB4 machine and same expositions conditions. The irradiation is performed after the right alignment is achieved.

- Deposition of Ti/Au. The sample is fixed in a sample holder and placed into the chamber of a e-beam evaporator PLASSYS MEB 400S. Here we deposit 10 nm of Ti to improve the adherence of the 100 or 150 nm of Au. The deposition rate is 0.15 nm/s for each material.
- Lift-off of Ti/Au. The Ti/Au bilayer deposited on top of the s1813 photoresist is lifted using a remover 1165 in a beaker which is placed in a water bath at 80°C for 40 minutes to 1 hour, followed by a few minutes in ultrasound bath . Finally, the sample is placed in deionized H_2O for 30 seconds.
- A control in an optical microscope to make sure that all the lithography ended well.

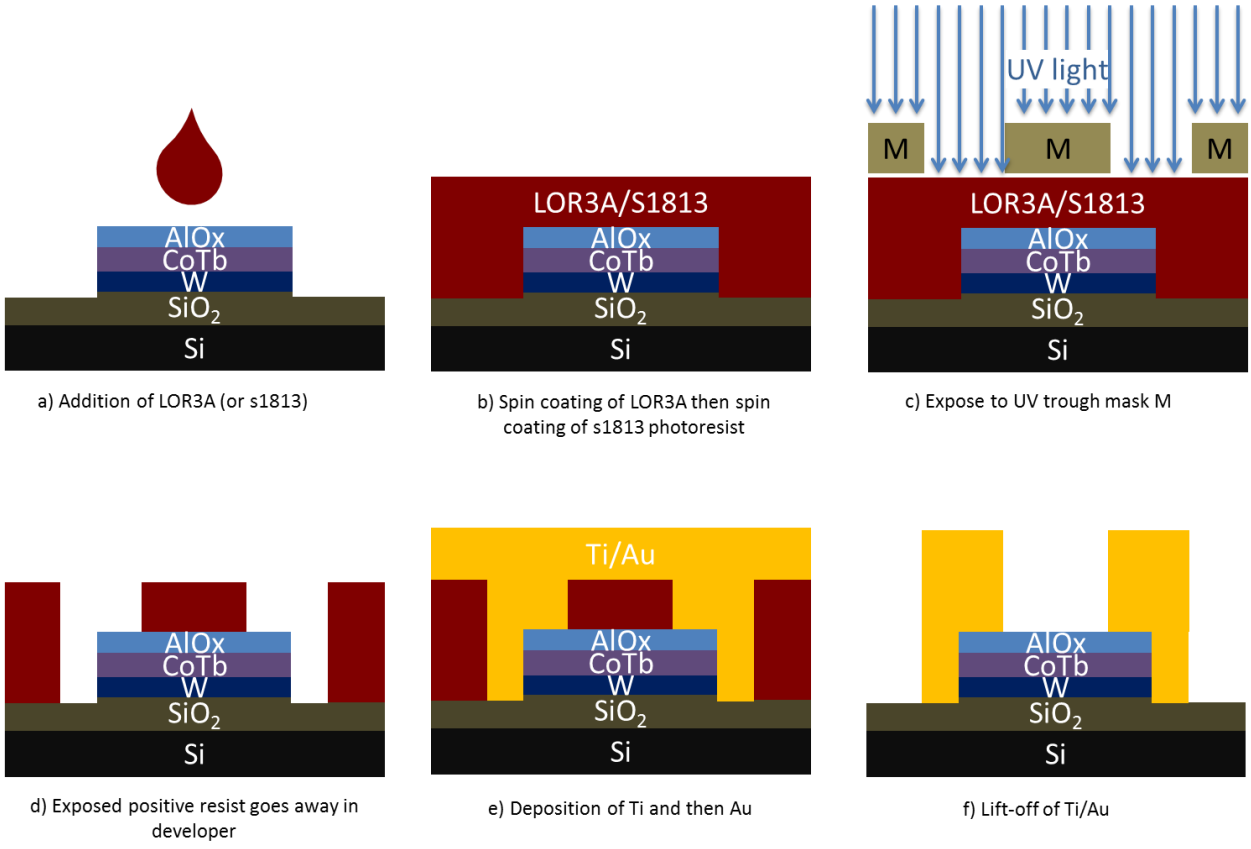

Figure 2.5: *Schematic of lift-off process by UV lithography used in my PhD.*

One of the key sub-processes is the alignment of the macroscopic contacts with the already patterned structures (Fig. 2.5c). To achieve this, alignment marks consisting of crosses and grids are used on the first (SOT1) and second (SOT2) masks. Figure 2.6 shows some images of myself using the spinner to add the photoresist and the MJB4 mask alignment equipment.

Figure 2.7 shows the mask designs for the samples fabricated for my thesis work. SOT refers to "spin-orbit torque". We can observe different geometries such as lines, to study domain wall propagation, single and double Hall bars. For my measurements I have mostly used the single Hall bar. Fig. 2.8 shows a micrograph of a 20 μm width devices (the width of the voltage channel is 4 μm).

Once the whole lithography process is finished the sample is cut into pieces of approximately 6x6 mm^2 which contain a block as shown in Fig. 2.8. These sample pieces are then glued on a chip or holder in order to perform Al wire bonding (Fig. 2.9). Now the devices of the sample are ready to carry out the magneto-transport experiments.

Figure 2.6: *Pictures showing myself doing some lithography steps. a) Deposition of a s1813 photoresist on a sample, which is installed on a spinner to obtain the desired thickness. The resist will then be annealed on a hot plate (115°C) to evaporate the solvent. These manipulations are carried out in a clean room, under a laminar flow hood to avoid any deposit of dust. b) Placing a sample previously coated with photoresist on the sample holder of an optical lithography machine (an MJB4 mask aligner) in a clean room. c) Pattern alignment of a mask, SOT2, on a sample previously coated with a photoresist and already etched using SOT1 mask (see the screen). Pictures are from Hubert RAGUET / IJL / CNRS Photo Library.*

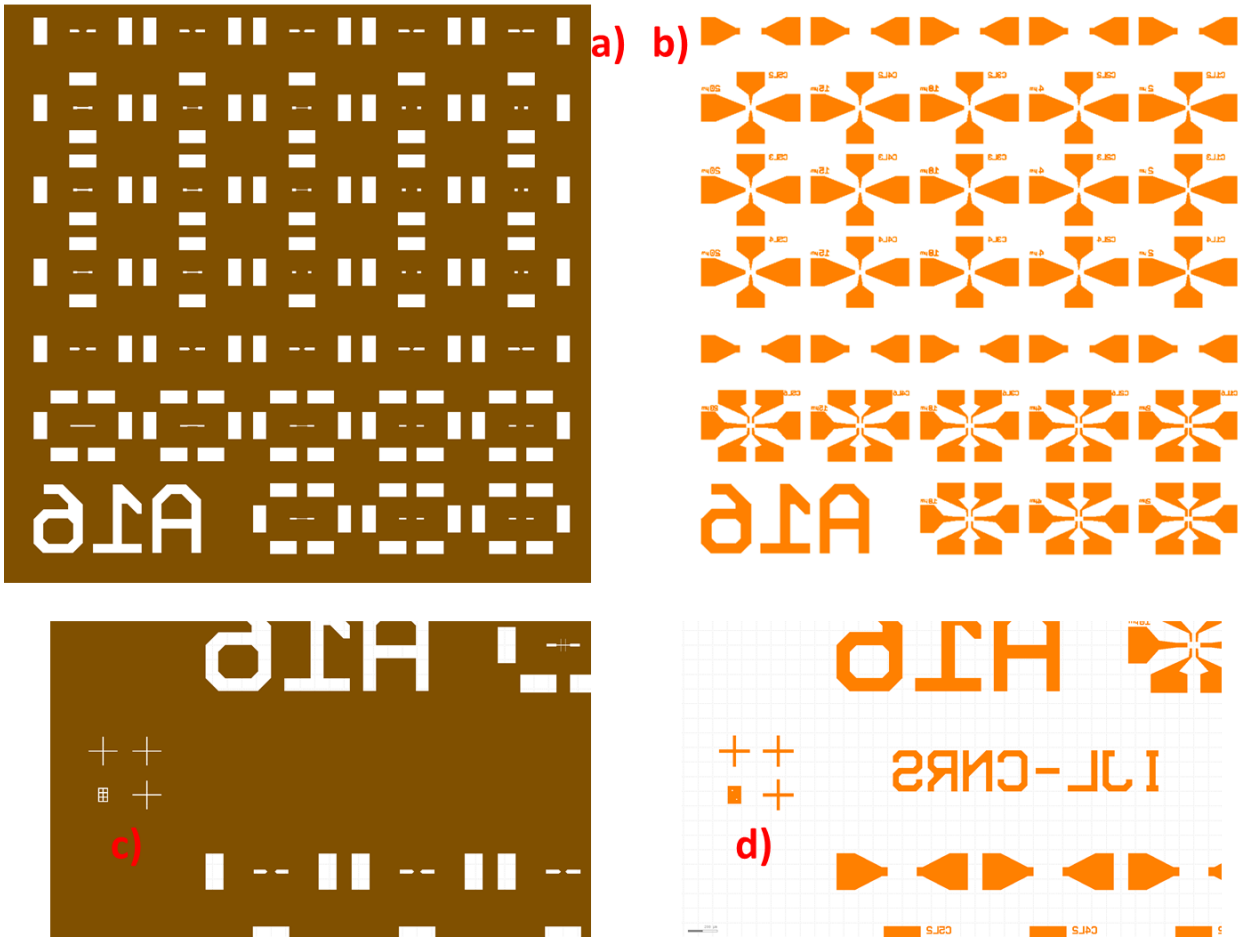

Figure 2.7: *Design of masks SOT1 (a) and SOT 2(b). The white or transparent region is the region where the positive photoresist remains after development. SOT1 is designed for etching. It means that in the white areas the thin films will remain after the etching process (as described above and in Fig. 2.4). SOT2 is designed for lift-off. It means that after the lift-off process the white areas will be the only only covered by Ti/Au previously deposited (as described also in Fig. 2.5). In these images we illustrate block A16. Each block fits in a region of 5x5 mm^2. In Figures (c) and (d) are shown the alignment marks of each layer or mask.*

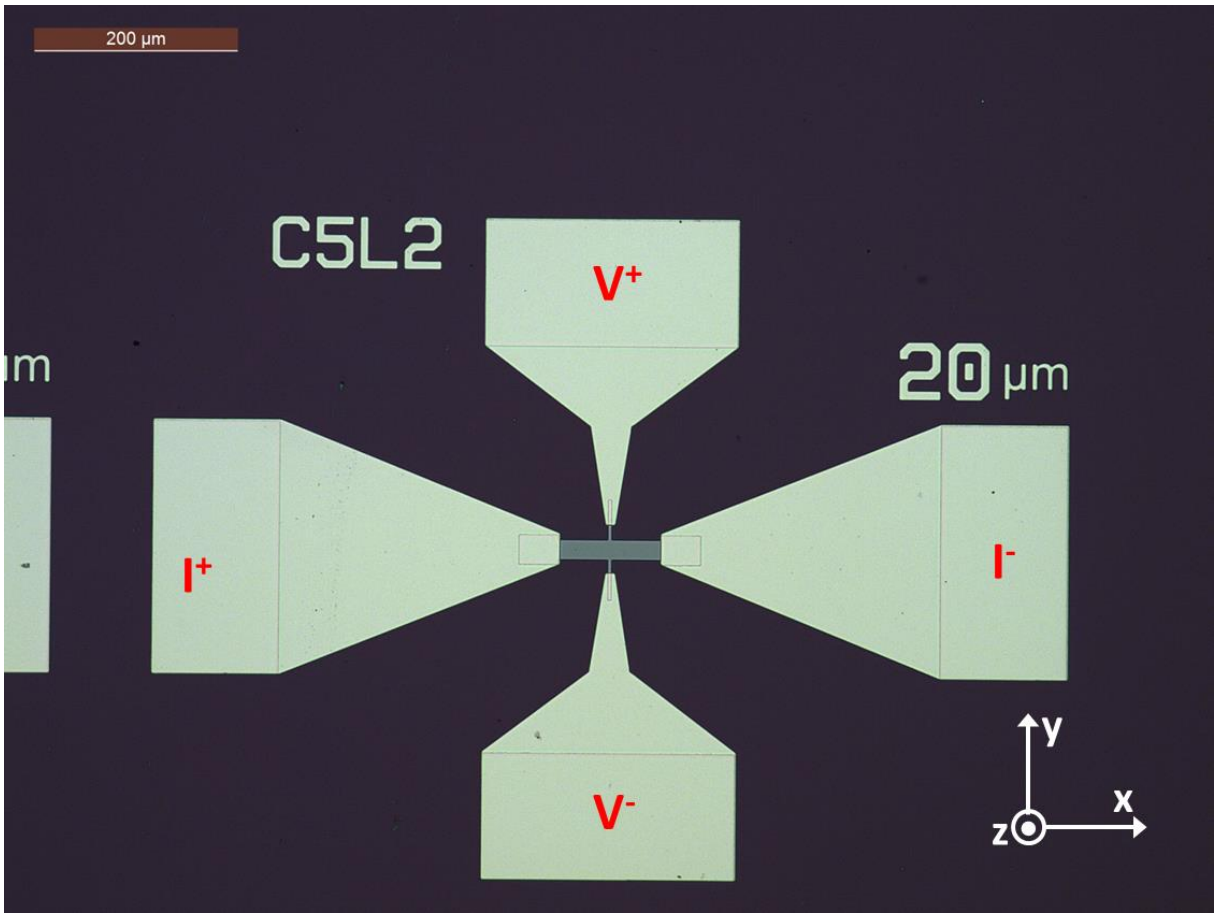

Figure 2.8. *Micrograph showing a typical Hall bar device at the end of the whole lithography process. In this case the device has a current channel of w= 20µm and the length between the ohmic contact is L= 100 µm. The used xyz reference systems as well as the current source and voltmeter contacts to measure transversal or Hall resistance are also displayed.*

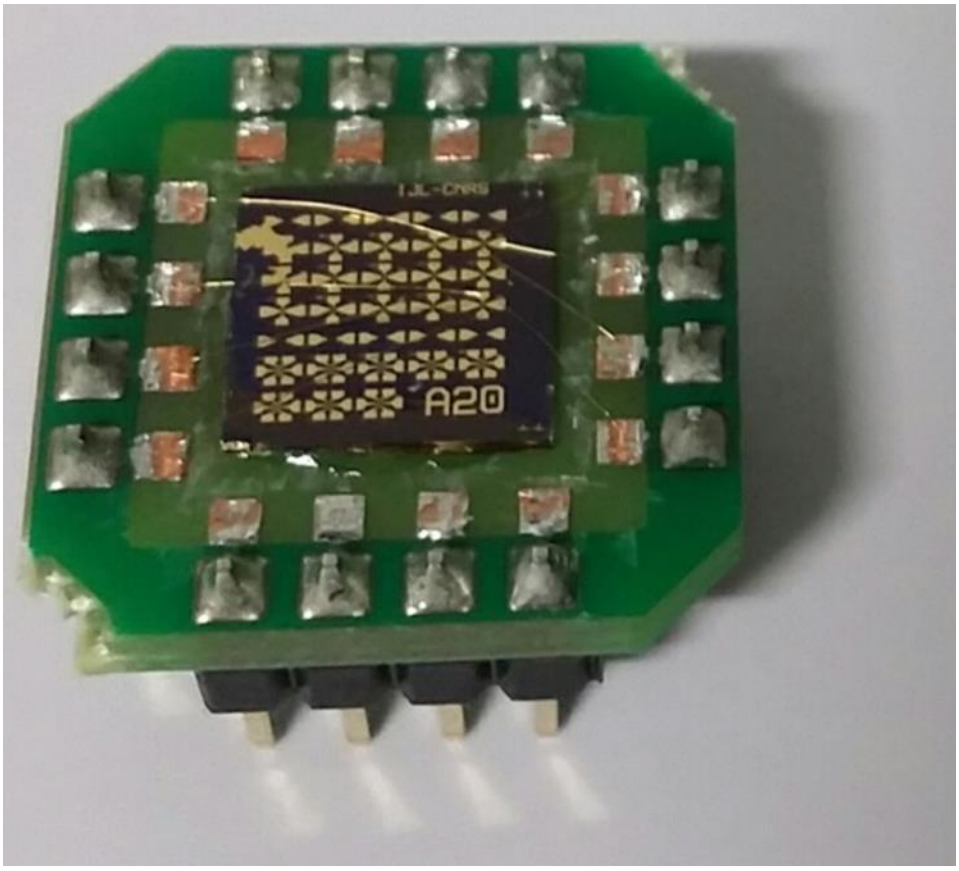

Figure 2.9: *Picture of a sample block containing several devices mounted in a green chip. Some of them are connected through Al or Au wire bonding to the green chip holder. So, it is ready to be measured.*

2.4 Magneto-transport (spin-orbit torque) setup

We have set up a system to carry out the main magneto-electrical measurements. This consists essentially of an electromagnet to set the DC magnetic field, and the *green chip* connected to a current source and voltmeter (Fig. 2.10). In the following we list the main components:

- The DC magnetic field is generated through an electromagnet. The one shown in Fig. 2.10 reaches 0.7 T.
- A PCB printed with up to 16 contacts where the green chip is connected.
- In turn this circuit board is connected to a current source (Keithley 6221) and a nanovoltmeter (Keithley 2182A). Both communicate with a PC through GPIB.
- A gauss-meter (observed in the red circle in Fig. 2.10c)

- Changing connections from one device to another was initially done manually. Recently a switch has been added and that allows us to change the connections from one device to another automatically. The switcher we use is a Keysight 34980A.
- We can also perform measurements using a lock-in amplifier. We have one that allows us to simultaneously measure the first and second harmonic (Ametek SR7270).

The protocol to carry out the main measurements is as following:

DC measurements: to perform the basic characterization. The Hall resistance *vs.* the perpendicular field, i.e R_{AHE}(Hz), is measured in this configuration. If the magnetization of the sample is spontaneously aligned perpendicular to the field plane, then a "square loop" is measured. Here we used a low current (typically 400 uA). In Fig. 2.10c we observe the sample placed in a position to carry out these measurements.

Pulse measurements: to perform the current-induced magnetization switching or spin-orbit torque switching. The sample is rotated so the film plane is parallel to the external dc magnetic field. Here we used the pulse mode of the K6221 current source and detect simultaneously the voltage in the K2182A nanovoltmeter. To do so, we turn off the GPIB connection of the K6221A which automatically turns on the RS232 serial connection. As indicated in the K6221 guide, a RS232 cable and a trigger cable are plugged between the K2182A and the K6221. The communication to the PC is just performed through the GPIB of the K6221. When the K2182A is coupled to the K6221A, the pulse width of the injected electrical current could be 100 us or above. We can inject up to 105 mA which is driven by a maximum voltage of 105 V. If we wish to inject much shorter current pulses, i.e. below 1μs, a voltage source is used instead a current source. However, typical voltage source with short pulses (in the range of few μs and ns) drive only a maximum voltage of 10V. This is a limitation if one would like to use such shorter pulses. For example if a device has a longitudinal resistance of 1kΩ and switch with a 100 μs current pulse of 20 mA then, a voltage of 20 V is needed to drive such switching current. If now we wish to use the standards voltage pulse source, it will be no possible since the voltage needed is well above the maximum voltage (10 V). Some option would be to reduce strongly the length of the device in order to reduce the longitudinal resistance. However, additional details have to be taken into account such as mismatch impedance which could be overcome using a bias-T and radio-frequency connectors. In any case, concerning the investigation of my PhD, I focus on 100 μs pulses. Thus, the coupled K6221 + K81282A are long enough.

All the above mentioned protocols can be carried out using the setup displayed in Fig. 2.10. In this case the experiments are performed at room temperature. However, the same setup and protocols can be transferred to any other magneto-transport setup. That is for example if we need higher magnetic field or, as in most of my studies, we need to perform the experiments at different temperatures. In the last case, we take advantage of the cryogenic system of PPMS where we can measure at temperatures between 5 and 350K and with a maximum field of 7 T.

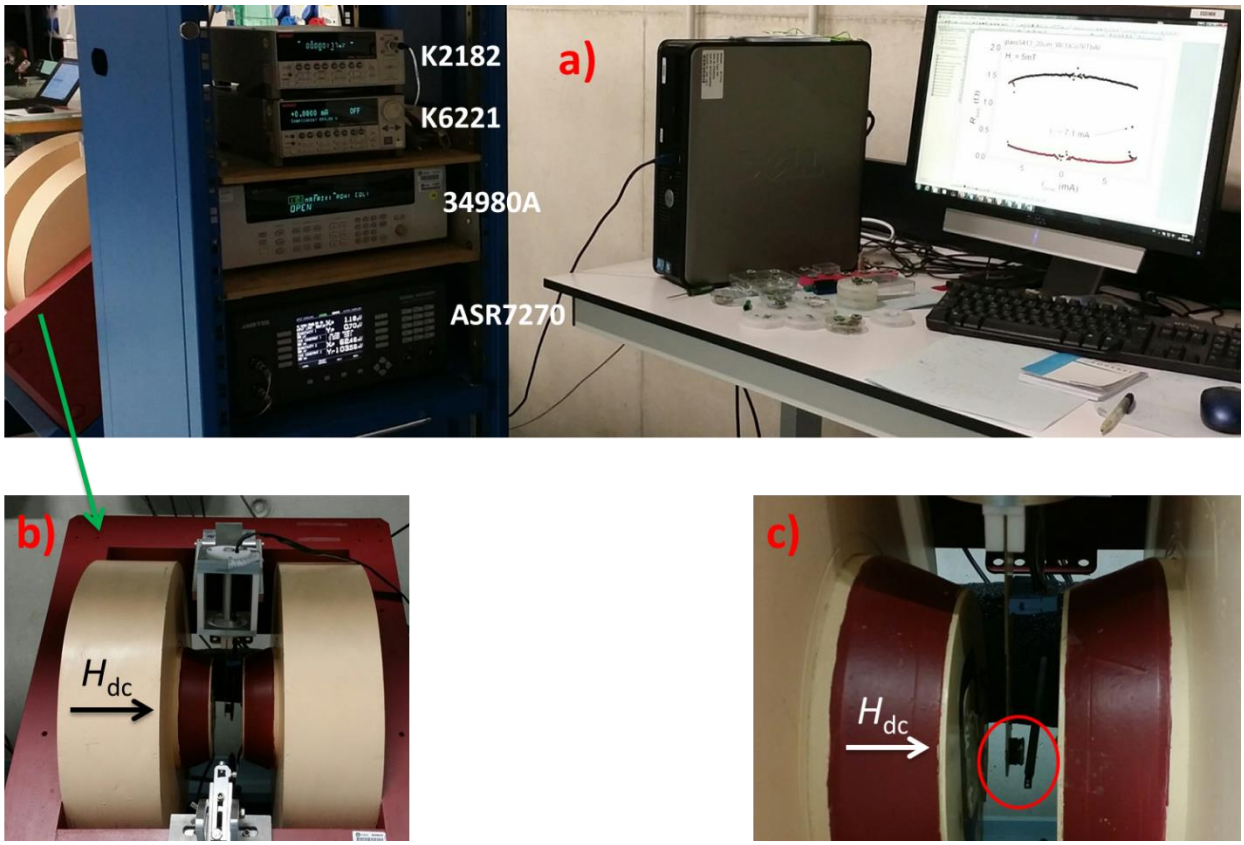

Figure 2.10: *a) Current version of the main magnetotransport setup I used during my PhD. We can observe the electromagnet (also in b and c), the current source K6221 and nanovoltmeter K2182A. Recently a Keysight 34980A switcher was added. This allows us to perform faster measurements commuting several devices or connections configurations. We also perform lock-in detection to study for instance second harmonic technique. b) The electromagnet with the fixed magnetic field direction displayed. c) A close view owing the sample holder inside the red circle. In this image the DC field is applied perpendicular to the field plane.*

References

[1] Bräuer, G., et al. "Magnetron sputtering–Milestones of 30 years." Vacuum 84.12 (2010): 1354-1359

Chapitre III

Retournement d'aimantation sous l'effet du couple spin-orbite dans des alliages ferrimagnétiques : Expériences et modélisations

Résumé

Nous avons étudié le retournement de l'aimantation induit par couple de spin orbite (SOT) dans les alliages intermétalliques terre rare – métal de transition, en utilisant comme système modèle les bicouches Co_xTb_{1-x}. Le courant de retournement varie de façon continue avec la composition de l'alliage et nous n'avons pas observé une réduction de celui-ci au point de compensation malgré la forte augmentation de l'efficacité du SOT. Un modèle basé sur les équations de Landau-Lifschitz-Gilbert couplées montre que la densité du courant de retournement est proportionnelle à l'anisotropie perpendiculaire effective, qui ne diminue pas au point de compensation. Ceci permet d'expliquer les données expérimentales. Ce modèle suggère aussi que les mesures du champ effectif associé au SOT ne permettent pas de conclure si le moment angulaire est transféré à l'un des sous-réseaux de l'alliage, ou à l'aimantation effective.

Summary

We have investigated spin-orbit torque (SOT)-induced switching in rare-earth-transition metal ferrimagnetic alloys using as model system the Co_xTb_{1-x} bilayers. The switching current is found to vary continuously with the alloy composition and no reduction in the switching current is observed at the magnetic compensation point despite a very large SOT efficiency. A model

based on coupled Landau-Lifschitz-Gilbert equations shows that the switching current density scales with the effective perpendicular anisotropy which does not exhibit a strong reduction at the magnetic compensation, explaining the behavior of the switching current density. This model also suggests that conventional SOT effective field measurements do not allow one to conclude whether the angular momentum is transferred to one sublattice or to the net magnetization. The effective spin Hall angle measurement shows an enhancement of the spin Hall angle with the Tb concentration which suggests an additional SOT contribution from the rare earth Tb atoms.

Chapter III

Spin-orbit torque-induced switching in ferrimagnetic alloys: Experiments and modeling

3.1 Introduction

Current - induced spin-orbit torque (SOT) has great applied interest for the next generation of spintronic devices due to its capability of manipulating magnetization efficiently [1,2]. So far, most studies of SOT have focused on ferromagnetic films in contact with heavy metals with strong spin-orbit coupling [3-7]. More recently, antiparallelly coupled magnetic systems, such as ferrimagnets, antiferromagnets and synthetic ferrimagnets, have emerged as promising candidates for more efficient SOT switching [8-14]. Indeed these magnetic systems could lead to a reduction of the energy consumption [15] as well as to a low susceptibility to external magnetic fields, which is necessary for data storage and memory applications [6].

Ferrimagnetic alloy materials, combining rare-earths (RE) and transition-metals (TM) provide many advantages. In these systems, the exchange coupling between the RE moments and the exchange coupling between the TM moments are ferromagnetic whereas it is antiferromagnetic between a TM moment and a heavy RE moment. The net magnetization can be tuned easily by varying the RE-TM compositions or the temperature [17,18]. Thus, the system can be either RE-rich - the net magnetization of the alloy is parallel to the magnetization of the RE sublattice direction or TM-rich - the net magnetization of the alloy is parallel to the magnetization of the TM sublattice direction. For a certain composition range there is given temperature at which the magnetization of the RE and TM sublattices have opposite directions and the same magnitude, resulting in zero net magnetization : it is named the compensation point.

Having two antiferromagnetically coupled sublattices with different orbital character, ferrimagnetic materials become attractive systems to study the spin transfer mechanism, by examining how the SOT-related phenomena change with the alloy composition [9]. Even though considerable efforts have been made in understanding the magnetization reversal by SOT in these systems, the mechanism still remains a scientific debate. The RE atoms have *4f* orbitals which are generally far below the Fermi level, thus one might expect that spin currents mainly interact with TM atoms rather than RE atoms. However, in some recent work it is argued that the SOT acts on the net magnetization [8-10]. Particularly, a divergence of the effective

field near the magnetization compensation point is reported [8, 12-14]. However, in [8,14] there is no evidence of a reduction of the critical switching current density at the compensation, although this is expected to show a minimum if the SOT is acting on the net magnetization [15]. Thus, it remains unclear whether the SOT acts preferably on an individual sublattice or on the net magnetization.

This chapter discusses SOT switching in Co_xTb_{1-x} ferrimagnetic alloys in contact with heavy metal W layer. Section 3.2 shows typical results of SOT-induced magnetization switching experiments. We obtained SOT switching for a wide range of Co and Tb concentrations, including samples near the magnetic compensation point. The switching current density changes continuously with the alloy composition without any reduction at the magnetic compensation. To explain these experimental results, in section 3.3, we develop a simple model based on the modified Landau-Lifschitz-Gilbert (LLG) equations. The model shows that the critical switching current density does not scale with the net magnetization but with the effective perpendicular anisotropy field H_k. H_k is not minimum at the magnetic compensation, which explains the absence of a minimum switching current at the compensation. The model also shows that conventional SOT effective field measurements cannot be the conclusive method to deduce that the spin angular momentum is simply transferred to net magnetization, as claimed in previous works. Section 3.4 reports measurements using the domain wall (DW) motion based technique to obtain the SOT effective field and the corresponding effective spin Hall angle. We find that the effective spin Hall angle increases by a factor of 2 with the increasing Tb concentration, indicating an additional contribution of the Tb atoms to SOT.

3.2 Samples and magnetic properties

The model samples for this study is a series of W(3nm)/Co_xTb_{1-x}(3.5nm)/Al (3nm, naturally oxidized) thin films, grown by DC magnetron sputtering ($0.71 \leq x \leq 0.86$). The films were then patterned into 20µm-wide and 100µm-long tracks with two Hall bars. A sketch of the sample structure and the measurement setup are shown in figure 3.1(a).

In these samples, the W layer plays the role of spin current source to generate the damping-like SOT [19]. The change of system's magnetization is detected using the anomalous Hall effect (AHE) described in Chapter II. The magnetization reversal can be detected even at the magnetic compensation point since the Hall signal comes mainly from the Co sublattice. Indeed the magneto-transport properties are dominated by the *3d* orbitals of the transition metal.

In Figure 3.1(b) I plotted the coercive field versus the Co concentration for several Co_xTb_{1-x} alloys at 300K. At x ~ 0.77 (green dashed line) the coercive field diverges, indicating that magnetic compensation occurs at this concentration at 300K. The compensation is also confirmed by the sign reversal of AHE cycles when crossing the point x ~ 0.77. Indeed for large applied field the net magnetization always follows the magnetic field direction. However when the alloy changes from Co-rich to Tb-rich the AHE cycles are inversed.

SOT-induced magnetization switching was performed by injecting 3ms-long in-plane current pulses in the Hall bars under the presence of a dc in plane magnetic field in the direction of the current. Figure 3.1(c) and 3.1(d) present typical examples of the AHE field hysteresis cycle and the SOT switching, respectively. It should be noted that the SOT-induced switching is achieved with a moderate current density (~10^{11} A/m^2) in this sample despite a very large coercive field near compensation. This is an interesting property that is promising for memory applications. The SOT switching is observed in all alloy compositions, and Figure 3.1(e) summarizes the switching current density J_{sw} versus x. We note that the current density refers to the one flowing in the W layer (in this experiment the resistivity of 3-nm thick W layer is 162 μΩ cm). J_{sw} shows a monotonous variation without any special behavior at the compensation, in contradiction with the expected reduction of J_{sw} at the compensation point [15].

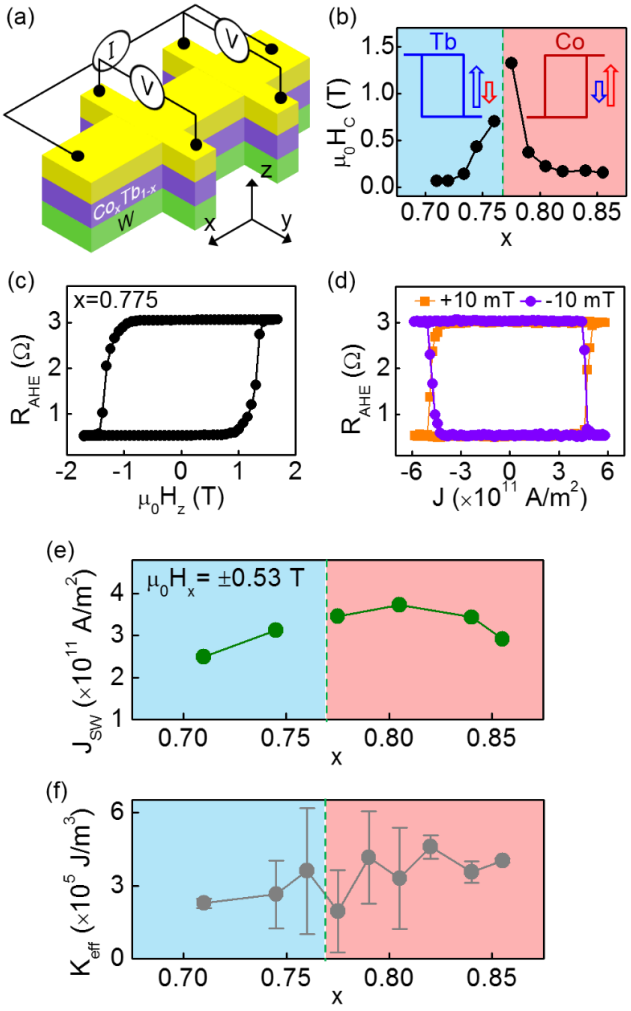

Figure 3.1: *(a) Sketch of the sample structure and AHE measurement (b) The coercive field of the Co_xTb_{1-x} ferrimagnetic alloys versus the composition. The blue and red arrows stand for the Tb and Co magnetizations in the presence of $+H_z$, respectively. The blue region (red region) stands for the Tb-rich phase (Co-rich phase). (c) Out-of-plane magnetization curve for a composition x=0.775 close to the magnetic compensation point. (d) Current-induced magnetization switching at $x = 0.775$ ($\mu_0 H_x$ = 10mT). (e) Switching current density for various H_x value on the left (in T). (f) Effective anisotropy energy vs the alloy composition.*

3.3 Theoretical model

To understand the continuous change in J_{sw}, we use a simple micromagnetic model adapted for ferrimagnets with two different sublattices a and b. In this model, we assume that the sublattices are strongly coupled antiparallel. In other words, the magnetic moments $\boldsymbol{M}^a$ and $\boldsymbol{M}^b$ of the sublattice a and b always stay antiparallel, thus we can define the effective net magnetization $\boldsymbol{M}$ as:

$$\boldsymbol{M} = \boldsymbol{M}^a + \boldsymbol{M}^b = M^a\boldsymbol{m}^a + M^b\boldsymbol{m}^b = (M^a - M^b)\boldsymbol{m} = M\boldsymbol{m}$$

with $\boldsymbol{m} = \boldsymbol{m}^a = -\boldsymbol{m}^b$ (see Fig. 3.2)

Here $M^{a(b)}$ is the magnetization magnitude of the sublattice a (b), $\boldsymbol{m}^{a(b)} = \boldsymbol{M}^{a(b)}/M^{a(b)}$ is the unit vector and M is the magnitude of the net magnetization $\boldsymbol{M}$.

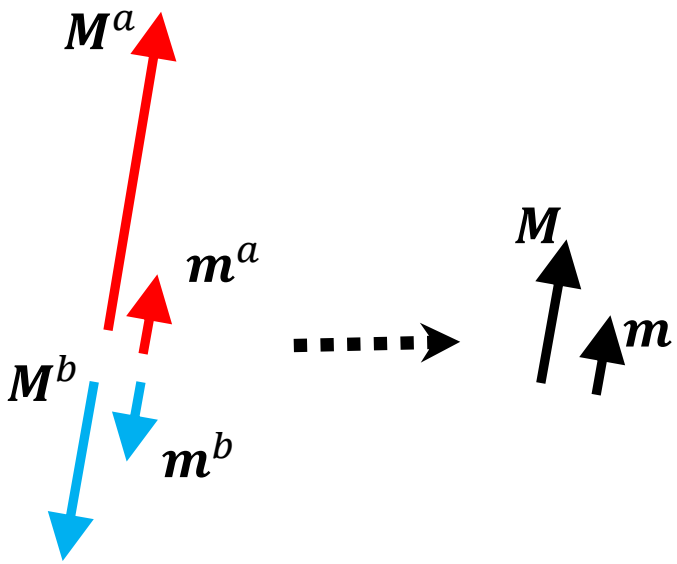

Figure 3.2: *In this model the magnetic moments $\boldsymbol{M}^a$ and $\boldsymbol{M}^b$ of the sublattice a and b are assumed to always stay antiparallel due to strong coupling*

The magnetization dynamics in the alloy can be described by modified LLG equations [20] written for each sublattice a and b as:

$$\frac{\dot{\boldsymbol{M}}^a}{\gamma^a} = -\boldsymbol{M}^a \times (\boldsymbol{H}^a + h\boldsymbol{M}^b) + \frac{\alpha^a}{\gamma^a}\boldsymbol{M}^a \times \dot{\boldsymbol{m}}^a - pT^a\boldsymbol{M}^a \times (\hat{\boldsymbol{y}} \times \boldsymbol{m}^a) \qquad (3.1a)$$

$$\frac{\dot{\boldsymbol{M}}^b}{\gamma^b} = -\boldsymbol{M}^b \times (\boldsymbol{H}^b + h\boldsymbol{M}^a) + \frac{\alpha^b}{\gamma^b}\boldsymbol{M}^b \times \dot{\boldsymbol{m}}^b - qT^b\boldsymbol{M}^b \times (\hat{\boldsymbol{y}} \times \boldsymbol{m}^b) \qquad (3.1b)$$

Here $\gamma^{a(b)}$ is the gyromagnetic ratio, $\alpha^{a(b)}$ is the damping constant. The field on the sublattice a, written as $(\boldsymbol{H}^a + h\boldsymbol{M}^b)$, is the sum of the effective local exchange field $h\boldsymbol{M}^b$ acting on the sublattice a and the remaining effective fields $\boldsymbol{H}^a$. This notation applies to the sublattice b. h is the coupling constant and it is the same for each sublattice because of reciprocity of the exchange energy.

The last term is the damping-like torque (spin-Hall torque), which is characterized by $T^{a(b)} = \hbar\theta_{SH}^{eff} J/2eM^{a(b)}t$, where $\hbar$ is the reduced Planck constant, θ_{SH}^{eff} is the effective spin Hall angle, J is the charge current density through the heavy metal layer, e is the electron charge, and t is the thickness of the magnetic layer. Here, p and q represent weighting factors for the transfer of the spin current to the sublattices a and b, respectively. Since we are assuming that the incoming spin angular momentum is fully transferred to the magnetic layer, the sum of p and q should equal to 1.

Equations (3.1a) and (3.1b) can be rewritten as:

$$\frac{\dot{M}^a}{\gamma^a}\dot{\boldsymbol{m}} = -\boldsymbol{m} \times (M^a\boldsymbol{H}^a + hM^aM^b\boldsymbol{m}) + \frac{\alpha^a}{\gamma^a}M^a\boldsymbol{m} \times \dot{\boldsymbol{m}} - pT^aM^a \times (\hat{\boldsymbol{y}} \times \boldsymbol{m}) \tag{3.2a}$$

$$-\frac{\dot{M}^b}{\gamma^b}\dot{\boldsymbol{m}} = -\boldsymbol{m} \times (-M^b\boldsymbol{H}^b - hM^aM^b\boldsymbol{m}) + \frac{\alpha^b}{\gamma^b}M^b\boldsymbol{m} \times \dot{\boldsymbol{m}} - qT^bM^b \times (\hat{\boldsymbol{y}} \times \boldsymbol{m}) \tag{3.2b}$$

By summing up Eqs. (3.2a) and (3.2b) we have:

$$\left(\frac{M^a}{\gamma^a} - \frac{M^b}{\gamma^b}\right)\dot{\boldsymbol{m}} = -\boldsymbol{m} \times (M^a\boldsymbol{H}^a - M^b\boldsymbol{H}^b) + \left(\frac{\alpha^a}{\gamma^a}M^a + \frac{\alpha^b}{\gamma^b}M^b\right)\boldsymbol{m} \times \dot{\boldsymbol{m}} - (pT^aM^a + qT^bM^b)\boldsymbol{m} \times (\hat{\boldsymbol{y}} \times \boldsymbol{m}) \tag{3.3}$$

Considering the first term:

$$-\boldsymbol{m} \times (M^a\boldsymbol{H}^a - M^b\boldsymbol{H}^b)$$

$$= -M\boldsymbol{m} \times \left(\frac{M^a\boldsymbol{H}^a - M^b\boldsymbol{H}^b}{M}\right)$$

$$= -\boldsymbol{M} \times \left(\frac{M^a\boldsymbol{H}^a - M^b\boldsymbol{H}^b}{M^a - M^b}\right)$$

Considering the last term (spin-Hall torque) term:

$$-(pT^aM^a + qT^bM^b)\boldsymbol{m} \times (\hat{\boldsymbol{y}} \times \boldsymbol{m})$$

$$= -M\boldsymbol{m}\left(\frac{pT^aM^a + qT^bM^b}{M}\right) \times (\hat{\boldsymbol{y}} \times \boldsymbol{m})$$

$$= -M\boldsymbol{m}\left(\frac{p\hbar\theta_{SH}^{eff}J}{2eM^{a}t}\frac{M^{a}}{M} + \frac{q\hbar\theta_{SH}^{eff}J}{2eM^{b}t}\frac{M^{b}}{M}\right) \times (\hat{\boldsymbol{y}} \times \boldsymbol{m})$$

$$= -\boldsymbol{M}\frac{(p+q)\hbar\theta_{SH}^{eff}J}{2eMt} \times (\hat{\boldsymbol{y}} \times \boldsymbol{m})$$

We define the effective values as follows:

The effective values of the gyromagnetic ratio:

$$\gamma_{eff} = \frac{M^{a} - M^{b}}{\frac{M^{a}}{\gamma^{a}} - \frac{M^{b}}{\gamma^{b}}} \tag{3.4}$$

The effective damping constant:

$$\alpha_{eff} = \frac{\frac{\alpha^{a}M^{a}}{\gamma^{a}} + \frac{\alpha^{b}M^{b}}{\gamma^{b}}}{\frac{M^{a}}{\gamma^{a}} - \frac{M^{b}}{\gamma^{b}}} \tag{3.5}$$

The effective field:

$$\boldsymbol{H}_{eff} = \frac{M^{a}\boldsymbol{H}^{a} - M^{b}\boldsymbol{H}^{b}}{M^{a} - M^{b}} \tag{3.6}$$

By defining these effective values, equation (3.3) can be written in the compact form:

$$\dot{\boldsymbol{m}} = -\gamma_{eff}\boldsymbol{m} \times \boldsymbol{H}_{eff} + \alpha_{eff}\boldsymbol{m} \times \dot{\boldsymbol{m}} - \gamma_{eff}\frac{(p+q)\hbar\theta_{SH}^{eff}J}{2eMt}\boldsymbol{m} \times (\hat{\boldsymbol{y}} \times \boldsymbol{m}) \tag{3.7}$$

Thus, we obtain the modified LLG equation of a strongly coupled ferrimagnetic thin film.

We can rewrite equation (3.7) by describing the effective field $\boldsymbol{H}_{eff}$ through its components. If H^{ext} is the external field and E_{ani} the effective anisotropy energy, including the magnetocrystalline anisotropy energy and the demagnetizing energy, we achieve:

$$\dot{\boldsymbol{m}} = -\mu_0\gamma_{eff}\boldsymbol{m} \times \boldsymbol{H}^{ext} + \frac{\gamma_{eff}}{M}\boldsymbol{m} \times \left(\frac{\delta E_{ani}}{\delta \boldsymbol{m}}\right) + \alpha_{eff}\boldsymbol{m} \times \dot{\boldsymbol{m}} - \gamma_{eff}(p+q)\left(\frac{\hbar\theta_{SH}^{eff}}{2eMt}\right)J\boldsymbol{m} \times (\hat{\boldsymbol{y}} \times \boldsymbol{m}) \tag{3.8}$$

where $E_{ani} = m_z^2 K_{eff}$ with the total effective anisotropy $K_{eff} = K - \frac{\mu_0(M_a - M_b)^2}{2}$. In this final form, all terms are written in terms of the net magnetization and the weighting factors disappear, as $p + q = 1$.

By solving Eq. (3.8) and following Ref. 21, we obtain the switching current density of the magnetic systems as:

$$J_{sw} \approx \frac{2e}{\hbar}\frac{t}{\theta_{SH}^{eff}}\left(K_{eff} - \frac{\mu_0 H_x M}{\sqrt{2}}\right) \qquad (3.9)$$

where H_x is an in-plane field along the current to assist the progress of SOT switching. The M dependence of J_{sw} arises from the demagnetizing energy in the effective anisotropy and from the Zeeman term associated to the in-plane magnetic field. At the compensation point, the net magnetization $M = 0$, but the net effective anisotropy $K_{eff} > 0$ because K_{eff} is obtained from the sum of the effective anisotropy energy values of each lattice. In our experiments, the first term proportional to K_{eff} is then much larger than the second term. Thus, J_{sw} does not scale linearly with M but scales with the net K_{eff}. As a result, no large reduction of the critical current density is predicted at the compensation. Therefore, the switching current density in the antiferromagnetically coupled system exhibits the continuous behavior, rather than the drastic change, across the compensation point [8, 14, 22].

Figure 3.1(f) shows the K_{eff} of the W/Co_xTb_{1-x} alloys *versus* x. K_{eff} is determined by M and the effective anisotropy field, which is obtained by the tilting of the magnetization under rotating external fields of 0.5-2T. The tilting is measured using AHE, and the effective anisotropy fields is then extracted by the best fit formulated by the Stoner-Wohlfarth model.[23] K_{eff} changes continuously across the magnetic compensation, which is a similar trend to the switching current density as shown in Fig. 3.1(e). The small dip in K_{eff} near the compensation can be explained by the limit of the simple Stoner-Wohlfarth model, which does not consider the small misalignment of the Tb and Co sublattices due to the large magnetic field needed to tilt magnetization, as discussed in previous reports [24, 25].

We note that the heating effect is not considered in our model while the thermal effect can play an important role [22]. Because in our samples W/Co_xTb_{1-x}, the resistivity of W layer is of the same order of magnitude as that of the Co_xTb_{1-x} layer, a noticeable amount of current flows through the magnetic layer, generating strong heating. The role of the heating effect will be discussed in details with experimental evidences in chapter IV. Even though our model can explain the absence of a reduction of the switching current density at compensation in our sample, the model would be more appropriate for systems with lower temperature dependence as for example Co_xTb_{1-x} on Pt, where most of the current goes through Pt layer.

3.4 Results of transport measurements

To quantify the SOT-induced effective field the modulation of the DW dynamics induced by SOT is measured [28-30]. A sketch of the measurement set-up and the typical AHE resistance are presented in Fig. 3.3(a). In this experiment, we studied devices with two Hall bars and the size of the channel is 20µm-wide and 100µm-long. The domain wall is nucleated at a natural nucleation point by a pulsed magnetic field, then driven along the channel by a combination of a perpendicular magnetic field H_z and a small bias DC current. The DW motion is observed at each Hall bar in real time.

By analyzing the two AHE resistance data sets, we deduced the time (t) needed for each DW to pass the Hall cross. Only the data that exhibit sufficiently separated reversal times are taken into account, to exclude the case where the DW is nucleated between the Hall bars. Using the experimental values of (t) and knowing the length L of the Hall cross, we can calculate the DW velocity $v = L/t$. Fig. 3.3(b) shows a typical result of DW speed curves as a function of $\mu_0 H_z$ under opposite bias currents $+J$ and $-J$. We can then define the effective field H_z^{eff} by measuring the horizontal shift between of the two curves for the two currents. This implies that the SOT-induced effective field for a given current density J acts on the DW like an effective field H_z^{eff}.

The efficiency of the SOT is defined as $\chi \equiv H_z^{eff}/J$. χ can be extracted from Figure 3.3(c) which presents the linear relationship between the effective field H_z^{eff} and current density J. In these measurements, we use very low current densities ($< 1.5 \times 10^{10}\ A/m^2$) to minimize significant effects from Joule heating. Indeed, for larger current densities, we observe a deviation of the effective field from linearity, resulting in an over-estimation or an under-estimation of χ as shown in the inset of Fig 3.3(c). Fig 3.3(d) and 3.3(e) show typical examples of the effeciency χ measured with respect to an in-plane field H_x for Tb-rich and for Co-rich alloys, respectively. χ increases linearly with H_x then it stays at a constant value χ_{sat} when the field is larger than a certain value H_{sat}.

Figure 3.4(a) presents the SOT efficiency χ_{sat} for various compositions of the Co_xTb_{1-x} alloys. The significant divergence of χ_{sat} near the magnetic compensation indicates the $1/M$ dependence. The magnitude of χ_{sat} reaches up to $37 \times 10^{-14}\ Tm^2/A$, which is more than 3 times larger than for Ta/Co_xTb_{1-x} ferrimagnetic alloys [8] and 5 times larger compared to the ferromagnetic Pt/Co/AlOx trilayers [3]. Although the effective field is extremely large at the compensation point, we note that this is not a firm indication of highly efficient switching at

compensation. For the switching operation, it is important to overcome the energy barrier [21,26] which is dominated by the effective anisotropy energy. Since the effective anisotropy does not simply scale as M, the minimized magnetization does not lead to the minimization of the switching current, which is more relevant to energy consumption.

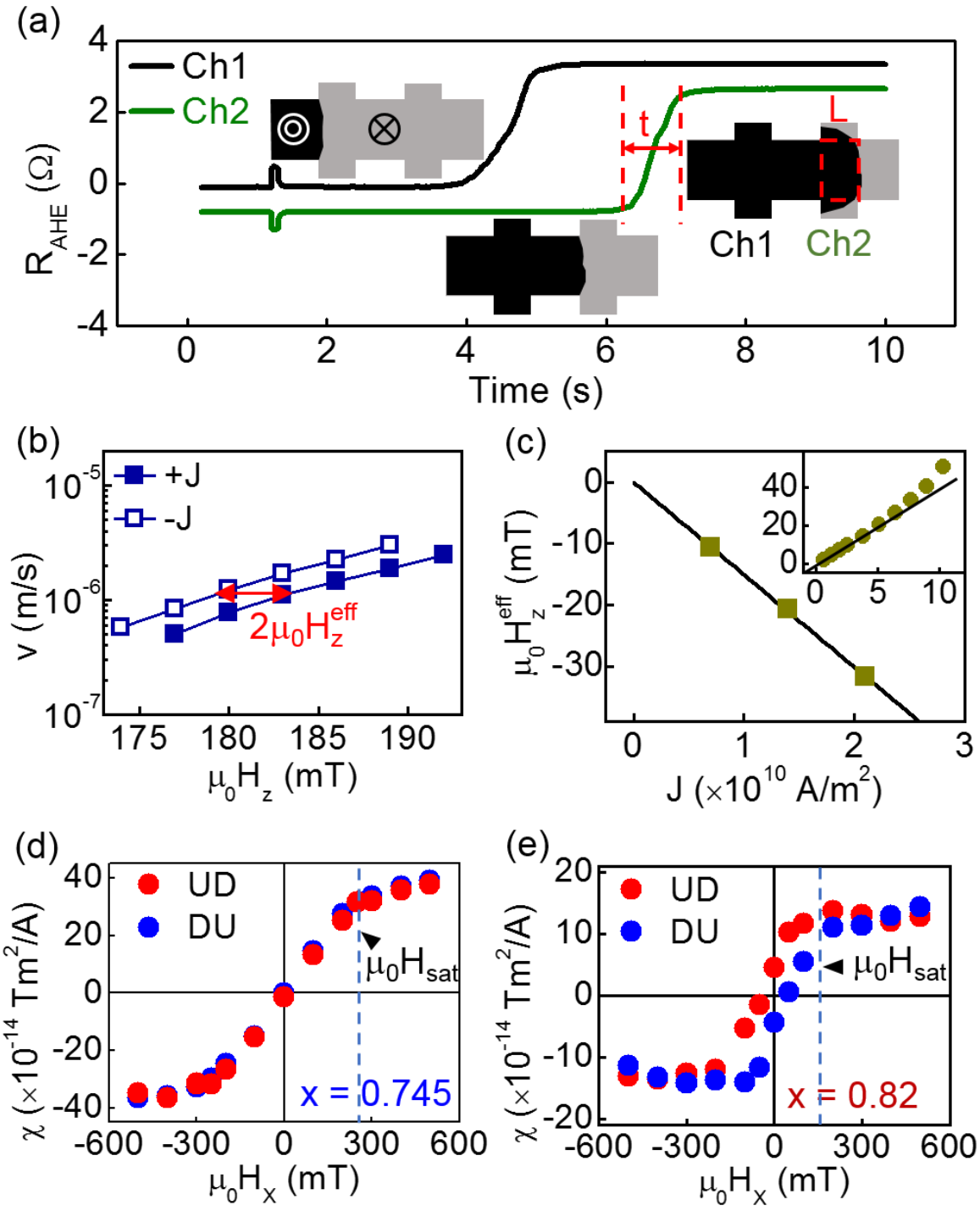

Figure 3.3: *(a) Sketch of the DW velocity measurement for the effective field measurement. (b) Typical example of DW speed curves modulated by H_{eff}. (c) Current-induced effective field as a function of current density. (d)-(e) Typical examples of the efficiency χ for Tb-rich (d) and Co-rich (e) alloys. The UD (DU) refers to the up domain (down domain) expansion.*

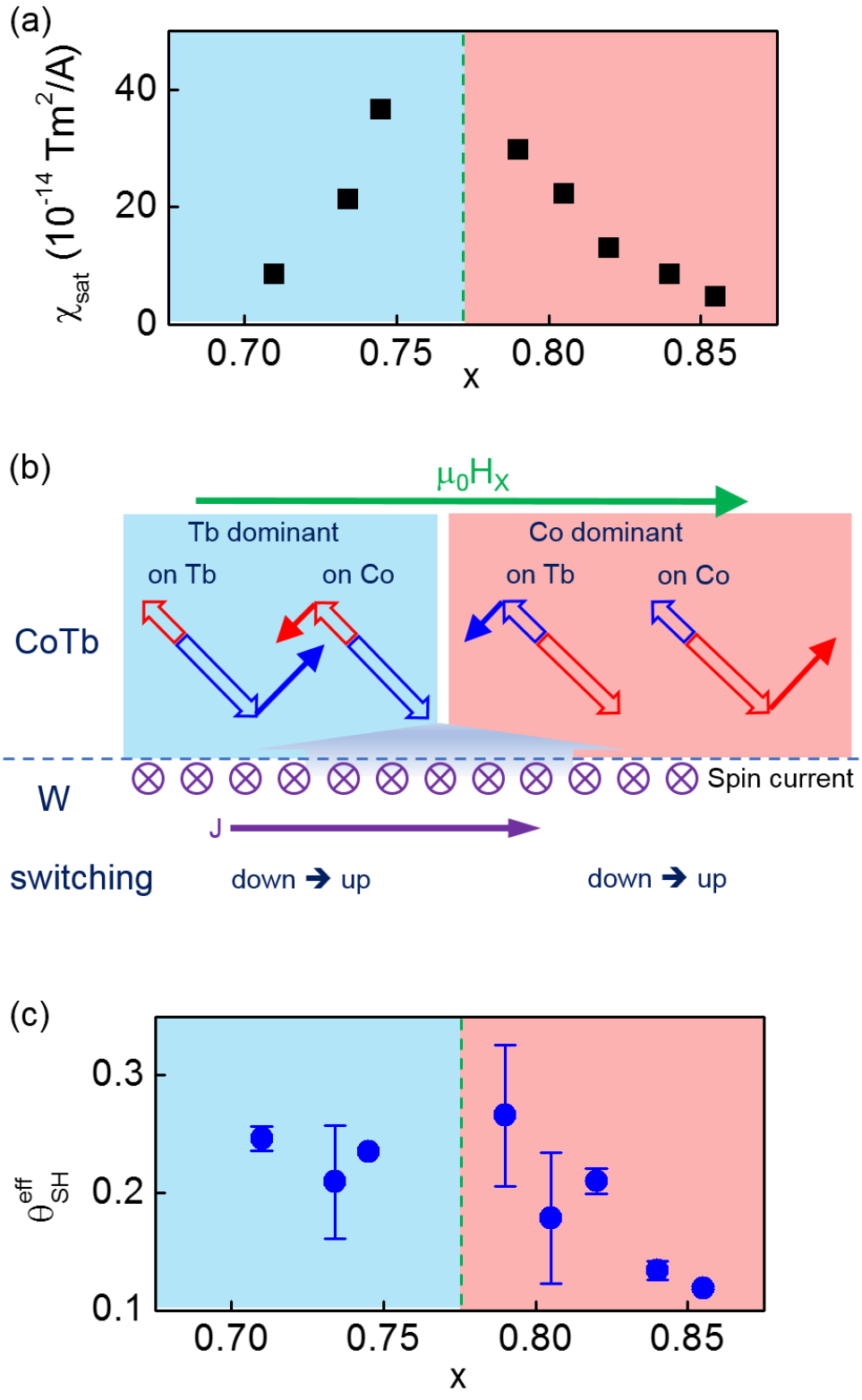

Figure 3.4: *(a) Divergence of χ_{sat} near the magnetic compensation. (b) Schematic representation of SOT effective fields. The spin current is transferred from the W layer and exerts a torque on either only Tb or only Co sublattices. In any case, the resultant switching polarity is the same. (c) Effective spin Hall angle vs. alloy composition*

3.5 Analytical model

To analyze the results in section 3.4, we consider a model based on two collective coordinates, namely the DW position q and the DW magnetic moment angle ψ [31, 32]. The model is constructed with the assumption of a static DW structure during its motion. Using the coupled LLG equations and a Lagrangian approach [32-34], we obtain the following coupled equations:

$$\dot{\psi} + \alpha_{eff}\frac{\dot{q}}{\Delta} = \gamma_{eff}J(p+q)\frac{\pi}{2}\frac{\hbar\theta_{SH}^{eff}}{2eMt}\sin\psi + \mu_0\gamma_{eff}H_z \qquad (3.10)$$

$$\alpha_{eff}\dot{\psi} - \frac{\dot{q}}{\Delta} = \mu_0\gamma_{eff}\frac{\pi}{2}H_x\cos\psi - \mu_0\gamma_{eff}\frac{MN_{DW}\sin 2\psi}{2}$$

with $\Delta = \sqrt{\frac{A}{K_{eff}}}$ and $N_{DW} = \frac{t\ln 2}{\pi\Delta}$ [35]

In these equations we neglect the Dzyaloshinskii–Moriya interaction (DMI). From equation (3.10), the SOT term is equivalent to an effective field $\mu_0 H_{SOT}^{eff} = J(p+q)\frac{\pi}{2}\frac{\hbar\theta_{SH}^{eff}}{2eMt}\sin\psi$. For $H_x < H_{sat}$, the domain wall internal structure continously rotates from Bloch to Néel, so that $\sin\psi = \frac{2\pi H_x}{MN_{DW}}$ and χ scales linearly with H_x. This linear behaviour is in agreement with the experimental observation (see Figures 3.3(d) and 3.3(e)). For $H_x > H_{sat}$, a Néel DW $\left(\psi = \frac{\pi}{2}\right)$ is achieved, which leads to a saturation efficiency $\chi_{sat} = \frac{H_{SOT}^{eff}}{J} = (p+q)\frac{\pi}{2}\frac{\hbar\theta_{SH}^{eff}}{2eMt}$. The same expression for the effective field and particular the $1/M$ dependence can be reproduced from modified LLG equation (Eq. 3.8 in section 3.3). Since the sum of the weighting factors $p+q=1$, the individual sublattice dependence disappears and H_{SOT}^{eff} simply carries the net magnetization. As a result, the SOT effective field in ferrimagnets diverges at the magnetic compensation point [8, 12-14]. Note that the effective field is basically determined by the comparison between the effect of the transferred SOT (which does not depend on M) and the magnetic susceptibility to an external field, and so, even though the same torque in transferred to the magnetic system, the system with small M gives rise to the larger effective field.

We emphasize that the divergent behavior, the sign of the effective field, and the switching polarity cannot provide the firm evidence that the SOT acts on the net magnetization rather than on the TM sublattice [10, 13]. Even in the case that the angular momentum

absorption concerns only one sublattice, i.e., p or q is 0, the experimentally determined effective field and switching current always show the same behavior and the same switching sign due to the strong coupling as described in Fig.3.4(b).

We also calculated the effective spin Hall angle θ_{SH}^{eff}, which indicates how much spin currents are transmitted to a magnetic layer. The values of θ_{SH}^{eff} versus composition for the W/Co_xTb_{1-x} alloys are presented in Figure 3.4(c). The values range from 0.11 to 0.26. There is a noticeable increase in θ_{SH}^{eff}, by a factor of 2, when passing from the Co-rich to Tb-rich phases. The θ_{SH}^{eff} increasing with the Tb concentration might be attributed to an additional contribution from the Tb atoms which have a large orbital angular momentum. For alloys with low thickness, it is reported that there might exist a segregation in the Tb composition, resulting in a relatively Tb-rich region at the top of the magnetic layer [39,40]. Since the sign of the spin Hall angle of RE is found to be positive [37], the spin currents from the bottom W and the rich Tb region at the top can be additive, leading to the enhancement of θ_{SH}^{eff} as the Tb concentration increases. A possible alternative explanation could be the increase in transparency of the W/ Co_xTb_{1-x} interface due to the increasing Tb composition, which may alter the interface properties, such as the spin-mixing conductance and hence θ_{SH}^{eff}. [41]

Regarding the DMI in the system, since the present DW motion based SOT effective field measurement are performed on a single DW, this technique may be used to quantify the DMI-induced effective field [26-28]. However, we find no significant DMI-induced field in the W/Co_xTb_{1-x} system which might be attributed to the relatively thick magnetic layer (3.5nm) and the single interface. The field-driven method [42, 43] and the Brillouin light scattering method [44] also yield consistent results.

3.6 Conclusion

In this chapter, I discussed the SOT-induced switching in RE-TM ferrimagnetic Co_xTb_{1-x} alloys in contact with a heavy metal W layer. We observed the SOT switching in a wide range of Co and Tb concentrations and the switching current density is not minimum at the magnetic compensation point. We explained these experimental results using a simple model based on antiferromagnetically coupled LLG equations. We find that the switching current density scales with the effective anisotropy, which exhibit no reduction at the magnetic compensation point. We also note that conventional SOT effective field measurement cannot clear up the debate of whether the spin currents are absorbed into one particular magnetization

sublattice or into the net magnetization. The effective spin Hall angle measurement shows an enhancement of the spin Hall angle with the Tb concentration which might suggest an additional SOT contribution from the rare earth Tb atoms. The results provide some new insights into the SOT-induced switching phenomena in both practical and theoretical terms.

References

[1] I. M. Miron, K. Garello, G. Gaudin, P.-J. Zermatten, M. V. Costache, S. Auffret, S. Bandiera, B. Rodmacq, A. Schuhl, and P. Gambardella, Nature **476**, 189–193 (2011).

[2] L. Liu, O. J. Lee, T. J. Gudmundsen, D. C. Ralph, and R. A. Buhrman, Phys. Rev. Lett. **109**, 096602 (2012).

[3] K. Garello, I. M. Miron, C. O. Avci, F. Freimuth, Y. Mokrousov, S. Blugel, S. Auffret, O. Boulle, G. Gaudin, and P. Gambardella, Nat. Nanotechnol. **8**, 587 (2013).

[4] L. Liu, C.-F. Pai, Y. Li, H. W. Tseng, D. C. Ralph, and R. A. Buhrman, Science 336, 555 (2012).

[5] S. Woo, M. Mann, A. J. Tan, L. Caretta, and G. S. D. Beach, Appl. Phys. Lett. 105, 212404 (2014).

[6] Q. Hao and G. Xiao, Phys. Rev. Appl. 3, 034009 (2015).

[7] M. Cubukcu, O. Boulle, M. Drouard, K. Garello, C. O. Avci, I. M. Miron, J. Langer, B. Ocker, P. Gambardella, and G. Gaudin, Appl. Phys. Lett. **104**, 042406 (2014).

[8] J. Finley and L. Liu, Phys. Rev. Appl. **6**, 054001 (2016).

[9] N. Roschewsky, T. Matsumura, S. Cheema, F. Hellman, T. Kato, S. Iwata, and S. Salahuddin, Appl. Phys. Lett. **109**, 112403 (2016).

[10] K. Ueda, M. Mann, C.-F. Pai, A.-J. Tan, and G. S. D. Beach, Appl. Phys. Lett. **109**, 232403 (2016).

[11] Z. Zhao, M. Jamali, A. K. Smith, and J.-P. Wang, Appl. Phys. Lett. **106**, 132404 (2015).

[12] N. Roschewsky, C.-H. Lambert, and S. Salahuddin, Phys. Rev. B **96**, 064406 (2017).

[13] W. S. Ham, S. Kim, D.-H. Kim, K.-J. Kim, T. Okuno, H. Yoshikawa, A. Tsukamoto, T. Moriyama, and T. Ono, Appl. Phys. Lett. **110**, 242405 (2017).

[14] R. Mishra, J. Yu, X. Qiu, M. Motapothula, T. Venkatesan, and H. Yang, Phys. Rev. Lett. **118**, 167201 (2017).

[15] J. Z. Sun and D. C. Ralph, J. Magn. Magn. Mater. **320**, 1227 (2008).

[16] T. Jungwirth, X. Marti, P. Wadley, and J. Wunderlich, Nat. Nanotechnol. 11, **231** (2016).

[17] M. Gottwald, M. Hehn, F. Montaigne, D. Lacour, G. Lengaigne, S. Suire, and S. Mangin, J. Appl. Phys. **111**(8), 083904 (2012).

[18] R. Tolley, T. Liu, Y. Xu, S. Le Gall, M. Gottwald, T. Hauet, M. Hehn, F. Montaigne, E. E. Fullerton, and S. Mangin, Appl. Phys. Lett. **106**(24), 242403 (2015).

[19] C.-F. Pai, L. Liu, Y. Li, H. W. Tseng, D. C. Ralph, and R. A. Buhrman, Appl. Phys. Lett. **101**, 122404 (2012).

[20] H. Oezelt, A. Kovacs, F. Reichel, J. Fischbacher, S. Bance, M. Gusenbauer, C. Schubert, M. Albrecht, and T. Schrefl, J. Magn. Magn. Mater. **381**, 28 (2015).

[21] K.-S. Lee, S.-W. Lee, B.-C. Min, and K.-J. Lee, Appl. Phys. Lett. **102**, 112410 (2013).

[22] T.-H. Pham, S.-G. Je, P. Vallobra, T. Fache, D. Lacour, G. Malinowski, M. C. Cyrille, G. Gaudin, O. Boulle, M. Hehn et al. Phys. Rev. Appl. **9**(6), 064032 ((2018).

[23] K.-W. Moon, J.-C. Lee, S.-B. Choe, and K.-H. Shin, Rev. Sci. Instrum. **80**, 113904 (2009).

[24] F. Hellman, Appl. Phys. Lett. **59**, 2757 (1991).

[25] T. Wu, H. Fu, R. A. Hajjar, T. Suzuki, and M. Mansuripur, J. Appl. Phys. **73**, 1368 (1993).

[26] N. Mikuszeit, O. Boulle, I. M. Miron, K. Garello, P. Gambardella, G. Gaudin, and L. D. Buda-Prejbeanu, Phys. Rev. B **92**, 144424 (2015).

[27] O. J. Lee, L. Q. Liu, C. F. Pai, Y. Li, H. W. Tseng, P. G. Gowtham, J. P. Park, D. C. Ralph, and R. A. Buhrman, Phys. Rev. B **89**, 024418 (2014).

[28] S.-G. Je, S.-C. Yoo, J.-S. Kim, Y.-K. Park, M.-H. Park, J. Moon, B.-C. Min, and S.-B. Choe, Phys. Rev. Lett. **118**, 167205 (2017).

[29] J. H. Franken, M. Herps, H. J. M. Swagten, and B. Koopmans, Sci. Rep. **4**, 5248 (2014).

[30] S. Emori, E. Martinez, K.-J. Lee, H.-W. Lee, U. Bauer, S.-M. Ahn, P. Agrawal, D. C. Bono, and G. S. D. Beach, Phys. Rev. B **90**, 184427 (2014).

[31] A. Malozemoff and J. Slonczewski, Magnetic Domain Walls in Bubble Materials (Academic Press, New York, 1979).

[32] A. Hubert, Theorie der Domanenwande in Geordneten Medien (Springer, Berlin, 1974).

[33] A. Thiaville, S. Rohart, É. Jué, V. Cros, and A. Fert, Europhys. Lett. **100**, 57002 (2012).

[34] O. Boulle, S. Rohart, L. D. Buda-Prejbeanu, E. Jué, I. M. Miron, S. Pizzini, J. Vogel, G. Gaudin, and A. Thiaville, Phys. Rev. Lett. **111**, 217203 (2013).

[35] S. V. Tarasenko, A. Stankiewicz, V. V. Tarasenko, and J. Ferré, J. Magn. Magn. Mater. **189**, 19 (1998).

[36] T. Schulz, K. Lee, B. Kr€uger, R. L. Conte, G. V. Karnad, K. Garcia, L. Vila, B. Ocker, D. Ravelosona, and M. Kl€aui, Phys. Rev. B **95**, 224409 (2017).

[37] N. Reynolds, P. Jadaun, J. T. Heron, C. L. Jermain, J. Gibbons, R. Collette, R. A. Buhrman, D. G. Schlom, and D. C. Ralph, Phys. Rev. B **95**(6), 064412 (2017).

[38] K. Ueda, C.-F. Pai, A. J. Tan, M. Mann, and G. S. D. Beach, Appl. Phys. Lett. **108**, 232405 (2016).

[39] B. Hebler, A. Hassdenteufe, P. Reinhard, H. Karl, and M. Albrecht, Front. Mater. **3**, 8 (2016).

[40] M. S. E. Hadri, M. Hehn, P. Pirro, C.-H. Lambert, G. Malinowski, E. E. Fullerton, and S. Mangin, Phys. Rev. B **94**, 064419 (2016).

[41] C.-F. Pai, Y. Ou, L. Henrique Vilela-Le~ao, D. C. Ralph, and R. A. Buhrman, Phys. Rev. B **92**, 064426 (2015).

[42] S.-G. Je, D.-H. Kim, S.-C. Yoo, B.-C. Min, K.-J. Lee, and S.-B. Choe, Phys. Rev. B **88**, 214401 (2013).

[43] D.-Y. Kim, M.-H. Park, Y.-K. Park, J.-S. Kim, Y.-S. Nam, D.-H. Kim, S.-G. Je, B.-C. Min, and S.-B. Choe, NPG ASIA Mater. **10**, e464 (2018).

[44] M. Belmeguenai, J.-P. Adam, Y. Roussigne, S. Eimer, T. Devolder, J.-V. Kim, S. M. Cherif, A. Stashkevich, and A. Thiaville, Phys. Rev. B **91**, 180405(R) (2015).

Chapitre IV

L'effet de la température sur le retournement de l'aimantation par couple spin-orbite dans le système métal / ferrimagnétique

Résumé

Dans ce chapitre nous présentons l'étude du retournement de l'aimantation par spin orbit torque du système W/Co_xTb_{1-x} , en utilisant des mesures de magnétométrie et de résistance Hall anomale entre 10K et 350K. Les mesures de retournement de l'aimantation sont effectuées dans la géométrie SOT avec les impulsions de courants injectées dans le plan des couches. Le renversement total de l'aimantation est observé pour tous les échantillons. Malgré la forte anisotropie des échantillons on mesure le retournement pour des faibles valeurs du champ appliqué dans le plan des couches. Ceci est dû à la contribution thermique au retournement. Nous trouvons une température caractéristique de retournement, T_{switch}, induite par effet Joule , qui est plus haute que la température de compensation du moment magnétique (T_{Mcomp}) et du moment angulaire (T_{Mcomp}).

Summary

In this chapter we present experimental study of magnetization switching by SOT of W/Co_xTb_{1-x} bilayers characterized using magnetometry and anomalous Hall resistance measurements, for temperatures ranging from 10 to 350 K. The current-induced-switching experiments are performed in the spin-orbit torque geometry where the current pulses are injected in-plane and the magnetization reversal is detected by the measurement of the Hall resistance. The full magnetization reversal has been observed in all samples. Despite its large perpendicular magnetic anisotropy we find magnetic reversal for a strongly reduced in-plane magnetic field which is due to the thermal contribution to switching. We find a characteristic switching temperature T_{switch} induced by Joule heating which is above the magnetic, (T_{Mcomp}) and angular (T_{Acomp}) compensation temperatures but below its Curie temperature.

Chapter IV

The effect of temperature on magnetization switching by spin-orbit torque in metal/ferrimagnetic system

4.1 Introduction

As shown in Chapter I, magnetization switching controlled by current induced spin orbit torque (SOT) came into the spotlight in recent years as a promising research direction for the new spintronics technology. To exploit full potential of SOT on spintronics devices, it is crucial to reduce the critical current density required for switching while maintaining a sufficient thermal stability. So far, intensive studies have focused on ferromagnetic materials, reporting typical values of the critical switching current density, J_{sw}, within order of $\sim 10^{10}$ to 10^{12} A/m^2. This range of J_{sw} depends on the applied current pulse duration and on the in-plane external magnetic field H_x [1 - 4]. For ferrimagnetic (FiM) systems, we have shown in Chapter III that J_{sw} is proportional to the FiM layer thickness t as for ferromagnetic ($J_{sw} \approx \frac{2e}{\hbar}\frac{t}{\theta_{SH}^{eff}}\left(K_{eff} - \frac{\mu_0 H_x M}{\sqrt{2}}\right)$).

As mentioned in Chapter 1, unlike ferromagnetic systems with interfacial perpendicular magnetic anisotropy (PMA), ferrimagnetic films based on rare-earth (RE) - transition metal (TM) alloys possess strong bulk PMA which makes them easier to integrate with different non-magnetic materials while keeping a large thermal stability [5]. In RE-TM alloys, RE and TM sublattices are antiferromagnetically coupled due to the exchange interaction between the f and d electrons. Thus, the net magnetization M, which is given by the sum of the magnetization of the two sublattices, is relatively low. Moreover, in ferrimagnetic materials, M can be tuned by varying the alloy composition and temperature. Especially, a magnetic compensation point with zero net magnetization can occur for a certain alloy concentration, x_{Mcomp}, or temperature, T_{Mcomp}, where the magnetization of he two sublattices compensate. The highly tunable magnetic properties of ferrimagnets make them attractive for potential applications. Indeed, there are many recent reports of ferrimagnetic systems applied in different fields such as ultrafast optical switching, current induced switching and domain wall motion [6,7,8]

Particularly, using ferrimagnetic materials for current induced magnetization switching opens the way to research towards reducing critical current density J_{sw} to reverse M and

consequently leading to low power consumption applications. There are debates on the modulation of J_{sw} in ferrimagnetic systems. In our experiment on W/Co_xTb_{1-x}/Al described in chapter III, J_{sw} does not show a minimum at the magnetic compensation point as might be expected if J_{sw} was proportional to the net magnetization. I have shown in the model in Chapter III that actually J_{sw} is proportional to the perpendicular anisotropy H_k. However, in chapter III we have only considered a simple model that neglects the heating effect.

In this chapter, I address the influence of temperature on current induced spin orbit torque switching by considering experiments on well characterized W/Co_xTb_{1-x}/Al systems for various concentrations. We demonstrate that the thermal effects are keys to explain the current induced magnetization reversal in this system. When the current is injected into the bilayer the Joule heating leads to a large increase of the sample temperature. Using systematic SOT measurements at different temperatures and alloy compositions, we established that for each concentration x the current induced magnetization switching occurs for a unique sample temperature $T_{\mathrm{switch}}(x)$. T_{switch} scales with the Curie temperature (T_C) of the alloy. In the specific case where T_{switch} is close to T_{Mcomp} an unexpected "double switching" is observed. This work has been published on Physical Review Applied [9]. More importantly, the SOT-switching process assisted by heating effect is reversible, thus demonstrating that the W/CoTb system is quite robust.

4.2 Samples and magnetic properties

To investigate the impact of temperature on SOT magnetization swiching in RE-TM alloys, we study a series of Co_xTb_{1-x} ferrimagnetic alloys deposited on a tungsten heavy metal film using DC magnetron sputtering. Deposition was done at room temperature. The full sample stack is $Si - SiO_2/W(3\ nm)/Co_xTb_{1-x}(3.5\ nm)/Al(3\ nm)$ with $0.71 \leq x \leq 0.86$. We used silicon substrates covered by an oxidized silicon layer of 100 nm thick to minimize the leakage current that might go through Si substrates in the measurements. The Co_xTb_{1-x} alloys were fabricated by co-sputtering pure Co and Tb sources. The relative concentration of the two elements Co and Tb was controlled by varying the sputtering powers. A 3 nm thick Al layer that naturally oxidized is used to protect the sample from oxidation. The W and CoTb layers have amorphous structure. This was confirmed by X-ray diffraction measurements where only broad amorphous contributions were observed even for films as thick as 20 nm.

In this section, I discuss the magnetic properties of Co_xTb_{1-x} alloys. Alloys of rare earth (RE) and transition metal (TM) have been studied for a long time and there are detailed reports on their properties (e.g. [10]). However, a thorough characterization of our particular samples is essential because the magnetic properties are very sensitive to the specific growth technique and conditions. Also, for RE-TM alloys, a small fluctuation of the sample composition can lead to important changes in magnetic properties of the system.

The magnetism of CoTb alloys is due to the itinerant magnetism of the Co sublattice and the localized *4f* electrons of the Tb atoms. The moments of the two sublattices are antiparallel. The exchange constant between the Co moments or between the Tb moments is positive while the exchange constant between a Tb and a Co moment is negative. This coupling between Co and Tb happens in an indirect way via the conducting *5s* electrons of the Tb atoms.

The total magnetization M_{CoTb} of CoTb alloy is described by the sum of the two sublattice contributions:

$$|M_{CoTb}(x_{vol}, T)| = |M_{Co}(T).(1 - x_{vol}) - M_{Tb}(T).x_{vol}|$$

Here, T is the temperature and x_{vol} is the volumic sample composition. The Curie temperature of Co is high (1400 K), thus we could consider M_{Co} to be independent from T for $T < 1000\ K$, in a very first approximation. However, Tb has a low Curie temperature (273K), so it is very sensitive to T. Consequently the compensation composition x_{Mcomp}, where the net magnetization is zero, is a function of temperature.

For ferrimagnetic alloys like CoTb, there exist a certain composition x_{Mcomp} where the antiparallel Co and Tb moments compensate each other, resulting in a net magnetization equals to zero. This value x_{Mcomp} is called magnetization compensation point. For Co concentrations lower than x_{Mcomp}, the net magnetization is parallel to the Tb sublattice. The composition is then called a Tb-rich composition. For Co concentrations higher than x_{Mcomp}, the net magnetization is parallel to the Co sublattice. The composition is then called Co-rich composition.

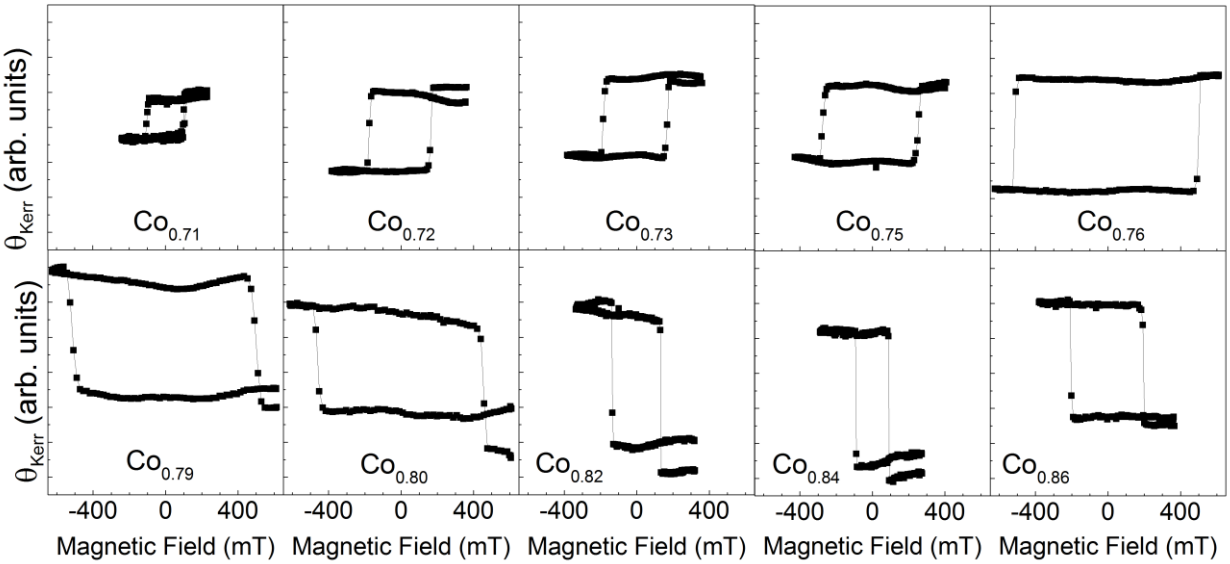

Figure 4.1: *Kerr cycles of samples Si-SiO_2/W(3nm)/Co_xTb_{1-x}(3.5nm)/Al(3nm) (x = 0.71 to 0.86) measured at room temperature.*

4.2.1 Magnetic compensation point x_{Mcomp}

The room temperature magnetic properties of the samples are examined using magneto-optic Kerr effect (MOKE) and superconducting quantum interference device – vibrating sample magnetometer (SQUID – VSM). Both MOKE and SQUID results show that all samples have a strong perpendicular magnetic anisotropy (PMA). From MOKE results presented in Figure 4.1, we notice the difference of the sign of Kerr cycles between samples with Co concentration $x < 0.77$ and those with $x > 0.77$. Since the Kerr signal is mainly sensitive to the Co sublattice when a red laser is used [11], the change of the Kerr loops sign can be seen as an indicator to distinguish between Co-rich and Tb-rich samples. Thus, the magnetic compensation, at which the Co and Tb moments cancel each other out, occurs around $x_{Mcomp} \approx 0.77$. Moreover, from SQUID-VSM results, this magnetization compensation point is also confirmed by examining the change of the coercivity H_c and the net saturation magnetization M_S with the alloys composition. As shown in Figure 4.2, both MOKE and SQUID results show a significant divergence of H_c when approaching the point $x_{Mcomp} \approx 0.77$. In addition, the M_S values obtained from SQUID-VSM measurements clearly show the tendency to reach 0 at $x_{Mcomp} \approx 0.77$. This value of room-temperature magnetization compensation point is close to the one reported earlier for bulk and thicker Co_xTb_{1-x} films [10,12].

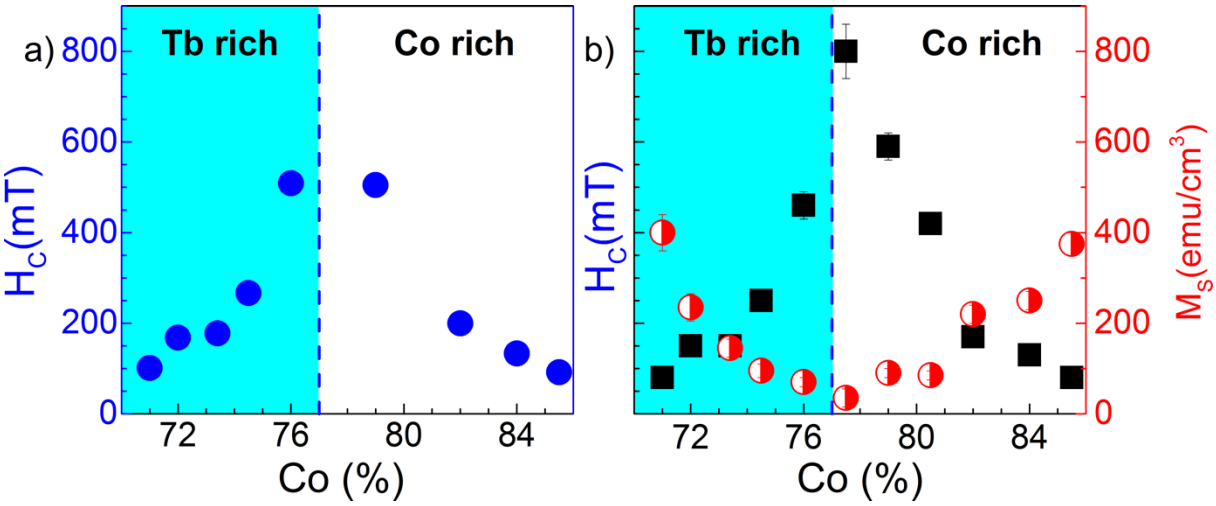

Figure 4.2: *Coercive field H_c and saturation magnetization M_S of samples Si-SiO_2/W(3nm)/Co_xTb_{1-x} (3.5nm)/Al(3nm) (x = 0.71 to 0.86) at room temperature. (a) H_c obtained by MOKE measurements. (b) H_c and M_S obtained by SQUID-VSM measurements. Magnetic compensation is observed for x_{Mcomp} ≈* 0.77.

As shown in figure 4.2(b), the advantage of this CoTb system is that we can obtain different values of magnetization between 0 and 400 emu/cm^3 by choosing specific concentration. The coercive field also changes in a large range from 100 mT up to 800mT for composition near compensation point. In order to explain the coercive field behavior, the competition of several magnetic interactions have to be considered including the Zeeman energy, the local anisotropy and exchange interactions. The Zeeman energy favors the reversal, while the two latter terms act against the nucleation of reversed domains. Once a reversed domain is nucleated, the competition is between Zeeman energy favoring the growth of this domain and local pinning fields that block the propagation of its domain walls. Consequently, coercivity diverges for small magnetization because strong fields are needed to reach significant Zeeman energies. This can also be understood, in a rough approximation using the Stoner-Wolfang model, $H_c \sim H_k = 2K/M_s$. From the last relationship, we can see that when M_s approches 0, H_c will diverge.

4.2.2 Compensation temperature T_{Mcomp}

After the deposition process, the $Si - SiO_2/W(3\ nm)/Co_xTb_{1-x}(3.5\ nm)/Al(3\ nm)$ stacks were patterned by standard UV lithography into micro-sized Hall crosses with a channel of 2, 4, 10 and 20 μm. The results shown in this chapter were obtained for the 20 μm Hall bars

unless otherwise specified. Ti(5)/Au(100) ohmic contacts were made by evaporation deposition and lift-off on top of W layers.

The magnetic compensation temperature of the samples are determined by measuring the anomalous Hall resistance R_{AHE} of the Hall crosses *versus* perpendicular magnetic field H_z at different temperatures. Figure 4.3 shows typicals results obtained for sample with 78% Co, where we plotted the temperature dependence of H_c. The coercive field H_c diverges around 280 K which determines T_{Mcomp} for this composition. While changing the temperature in the experiments, we can also identify the T_{Mcomp} by observing the change of the sign of $R_{AHE}(H_z)$ cycle, namely the change of field switching polarity (Field-SP). As shown in the insets of figure 4.3, the $R_{AHE}(H_z)$ cycle is reversed for Tb-rich (T<280 K) and Co-rich (T>280 K) phases. This change happens because anomalous Hall resistance is sensitive to the cobalt sublattice. The AHE is in fact a property of the itinerant Co electrons, so its sign switches at the compensation point in the presence of an external magnetic field, when the orientation of the Co moments switches.

For different alloy compositions between 0.76<x<0.82 we were able to obtain the T_{Mcomp} with an error bar lower than 10 K. For the others compositions, due to experimental limitations (7T maximum field and 400K maximum temperature in our measurement setup) we could not t determine the T_{Mcomp} value with such a precision. Nevertheless, we could obtain T_{Mcomp} for x > 0.82 with a larger error bar. Finally, for x<0.76, due to the fact that T_{Mcomp} shows a linear behavior on Co-composition, we could extrapolate $T_{Mcomp.}$ Thus, we have the value of T_{Mcomp} versus Co concentrations for the whole range in our sample.

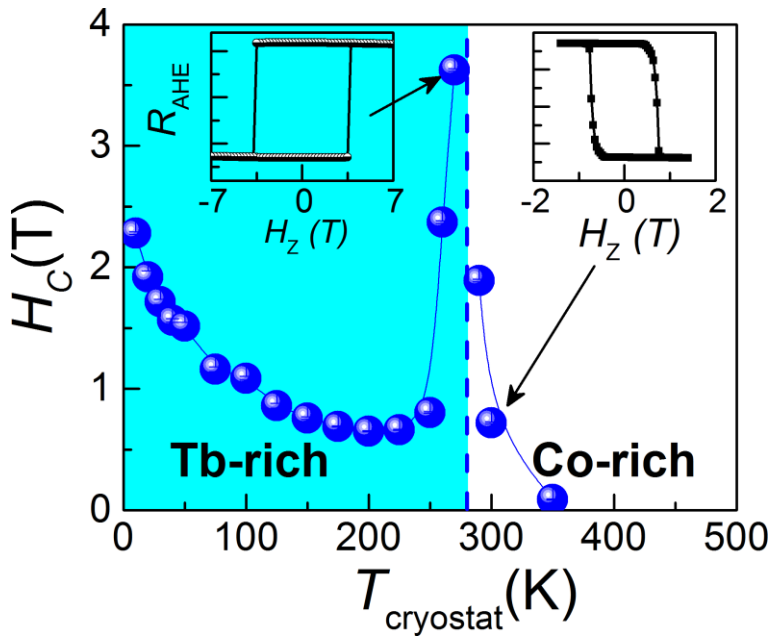

Figure 4.3: *Temperature dependence of coercivity field H_c on Hall bar W/$Co_{0.78}Tb_{0.22}$/Al. T_{Mcomp} ~ 280K. Insets show the Hall resistance cycle for a temperature below (left) and above (right) T_{Mcomp}. H_c at 350K is 90mT.*

4.2.3 Angular momentum compensation temperature T_{Acomp}

Besides the characteristic temperature where the net magnetization is zero, there is another one where the angular moment is zero, namely T_{Acomp}. This T_{Acomp} is different from T_{Mcomp} because of the different values of the gyromagnetic ratio for Co and Tb, $\gamma_{Co,Tb} = g_{Co,Tb}\mu_B/h_b$, where g_{Co}(or g_{Tb}) is the Landé g factor of Co (or Tb), μ_B is the Bohr magnetron and h_b is the reduced Planck constant. To figure out the correlation of the angular momentum compensation temperature T_A and the compensation temperature T_M, we follow the equation suggested by Yuushou Hirata *et al.* [13]:

$$T_A = T_M + T_C\left[1 - \left(\frac{g_{Co}}{g_{Tb}}\right)^{\frac{1}{(\beta_{Co}-\beta_{Tb})}}\right]\left(\frac{M_{Tb}(0)}{M_{Co}(0)}\right)^{\frac{1}{(\beta_{Co}-\beta_{Tb})}} \qquad (4.1)$$

where T_C is the Curie temperature, g_{Co}(or g_{Tb}) is the Landé g factor of Co (or Tb), β_{Co} (or β_{Tb}) is the critical exponent of Co (or Tb), and $M(0)$ is the saturation magnetization at 0K.

It is known that g_{Co} ~ 2.21 [14, p.123] and g_{Tb}~ 1.5, the saturation magnetization of Co and Tb near 0K is 1.72 μ_B/atom [14, p.139] (corresponds to $M_{Co}(0) = 1450$ emu/cm^3) and 7.5 μ_B/atom [15] (corresponds to $M_{Tb}(0) = 2170$ emu/cm^3), respectively. Previous work of Plessis et al. [16] reveals that β_{Tb} varies from 0.282 to 0.378, in this calculation we use the average

value of $\beta_{Tb} = 0.323$. The theoretical values for β_{Co} are $\beta_{Co} = 0.125$ (2D Ising models) [17] and $\beta_{Co} = 0.23$ (2D XY models) [18].

Using these values in equation (4.1) we have: $T_A \approx T_M + 0.112\, T_C$ in case $\beta_{Co} = 0.125$ or $T_A \approx T_M + 0.013\, T_C$ in case $\beta_{Co} = 0.23$.

Extracting the values of T_C in Hansen's paper [10], and our experimental values of T_M, we can roughly estimate T_A of the samples (Fig. 4.4).

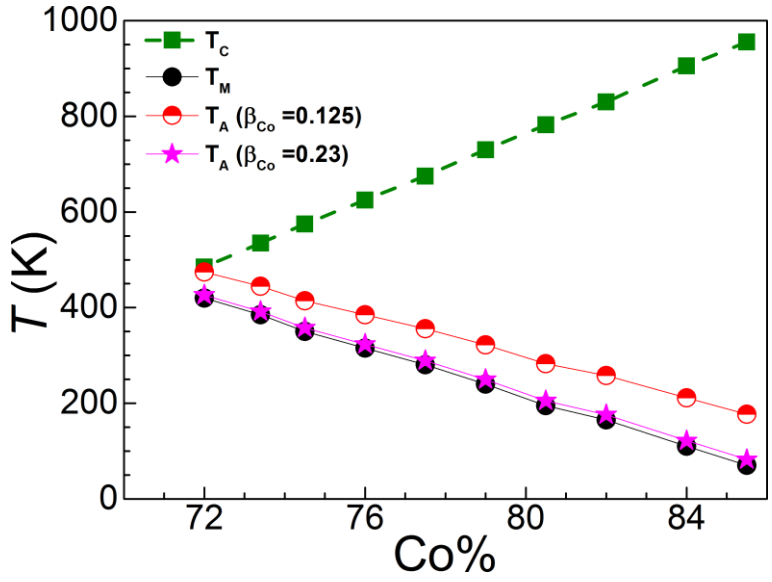

Figure 4.4: *The variation of T_C, T_M, and T_A of $W/Co_xTb_{1-x}/AlOx$ with Co concentration. T_{Mcomp} and T_{Acomp} decrease linearly when increasing the Co concentration in the alloys.*

Although we need more experimental parameters on real systems to achieve the exact values of T_A in our samples, these results confirm that T_A follows the trend of T_M with a small deviation. Thus, both decrease linearly when increasing Co-concentration, in opposite ways with respect to T_C.

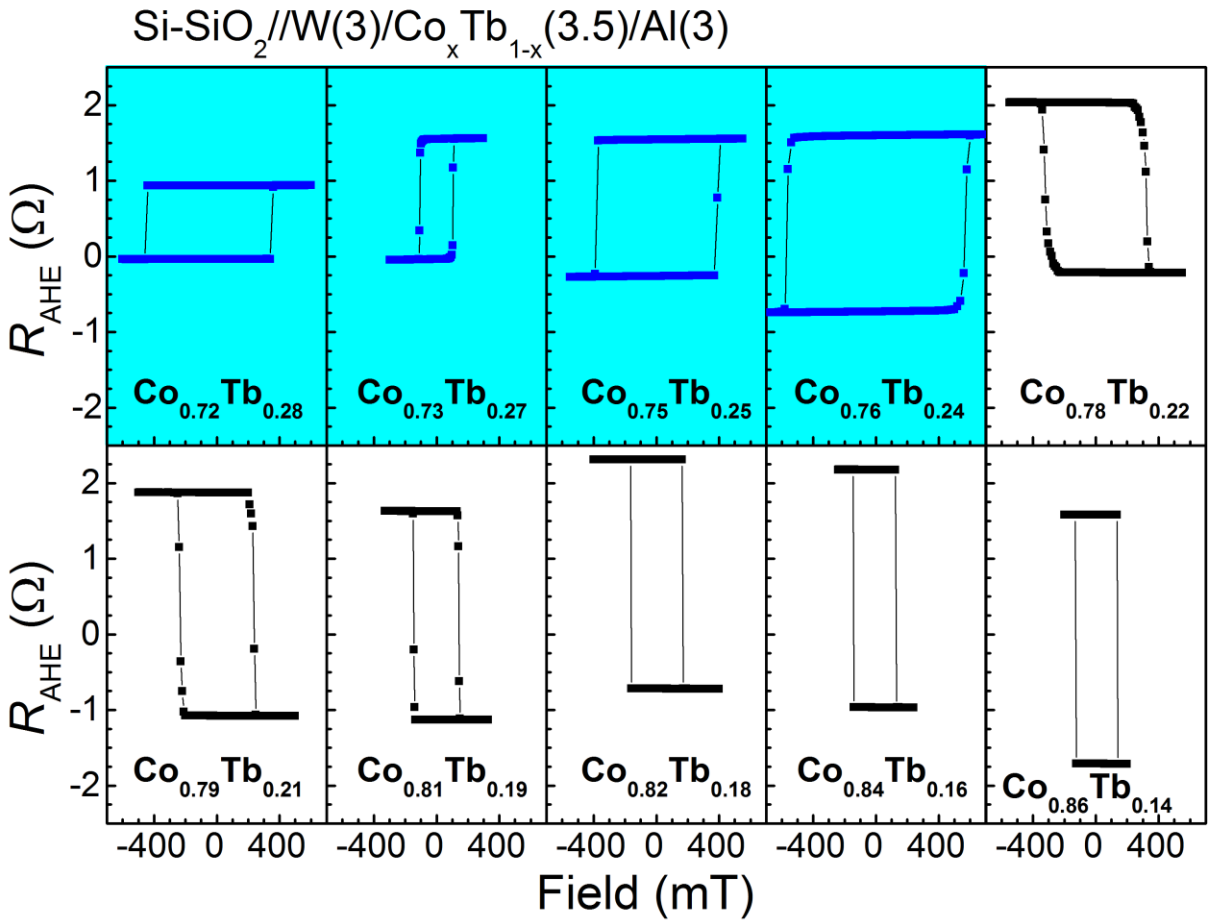

Figure 4.5: *Anomalous Hall resistance (R_{AHE}) as a function of perpendicular magnetic field at room temperature for Si-SiO_2//W(3)/Co_xTb_{1-x}(3.5)/Al(3) samples. Note that the AHE resistance displayed in the figure was not yet normalized by the current flowing in the CoTb layer but by the total current injected (400 uA).*

4.2.4 Field - induced magnetization switching

Before performing current-induced spin orbit torque switching, we checked the switching of the samples magnetization under perpendicular magnetic field. Figure 4.5 shows the results performed on the Hall crosses. As shown in the figure, all samples keep perpendicular magnetic anisotropy after lithography process. It should be noted that since Tb is sensitive to temperature, it is important to minimize the exposure of our samples to temperature during the lithography and lift-off processes, to ensure that we keep the PMA property. This would seem to be unfavorable for applications where the heat treatments are long (1 or 2 hours) and at higher temperatures (300°C) than those we use (115°C). However, we will show that in the case of W/CoTb our system is robust. In Figure 4.5 we show the change of field switching polarity between samples with Co composition *x* below and above 0.77. This

indicates that the magnetic compensation point $x_{Mcomp} \approx 0.77$ remains the same after lithography process for the series $Si - SiO_2/W(3\ nm)/Co_xTb_{1-x}(3.5\ nm)/Al(3\ nm)$. Note that it is not always the case, since we also studied a series of CoTb films in contact with a Pt layer ($Pt/Co_xTb_{1-x}/AlOx$) and for these samples we observed a shift of the magnetic compensation point after lithography process. Once again, the W/CoTb system shows advantages.

4.2.5 Determination of Hall angle θ_{AHE} in Co_xTb_{1-x} (3.5nm)

We can further analyze our results of Fig 4.5 and determine the Hall angle evolution in our W/Co_xTb_{1-x} systems. To do so, we need to know the longitudinal ρ_{xx} resistivity as well as the transversal or Hall resistivity ρ_{xy}. First, we have determined independently the resistivity of W(3nm) in a Si-SiO2//W(3)/MgO(5) structure by Van der Pauw methods. It yields 162 μΩ.cm. Then we can estimate the longitudinal resistivity as function of Co-concentration in our W/Co_xTb_{1-x} system. The result is displayed in Fig 4.6(c). The Hall angle θ_{AHE} is defined as the transversal electric field (due to Hall voltage) over the longitudinal electric field (due to the current injected).

Let's consider that the longitudinal channel has a length L and width W. For the case of a single layer the longitudinal voltage is $V_{xx}=E_{xx}L=\rho_{xx}j_{xx}L=\rho_{xx}IL/(Wt)$, where j_{xx}, I and *t* stand for the current density, injected current, and thickness of the layer, respectively. The transversal voltage is thus $V_{xy}=E_{xy}W=\rho_{xy}j_{xx}W=\theta_{AHE}\rho_{xx}I/t$. Then, for a single magnetic layer, the Hall angle can be determined as:

$$\theta_{AHE} = \frac{V_{xy}}{V_{xx}} \frac{L}{W} \tag{4.2}$$

which can be rewritten in the most well-known way:

$$\theta_{AHE} = \frac{R_{AHE}}{R_{xx}} \frac{L}{W} = \frac{R_{AHE}}{\rho_{xx}} t \tag{4.3}$$

In the case of multilayers, the relationship to determine θ_{AHE} is different. Let's consider a bilayer HM/FM (also useful to avoid confusion between tungsten and width). Once can consider the longitudinal electric field which generates longitudinal and transversal current

densities which in turns should be canceled by the current generated in each layer by the transversal field. Thus we arrive to:

$$\theta_{AHE} = \frac{V_{xy}}{V_{xx}} \frac{L}{W} \left[1 + \frac{\sigma_{NM} t_{NM}}{\sigma_{FM} t_{FM}} \right] \tag{4.4}$$

where σ_i stands for the longitudinal conductivity of each layer. This expression can be rewritten in terms of the Hall resistance, R_{AHE}, and the longitudinal resistivity of the FM layer, ρ_{FM}, as:

$$\theta_{AHE} = \frac{R_{AHE}}{\rho_{FM}} t_{FM} \left[1 + \frac{\sigma_{NM} t_{NM}}{\sigma_{FM} t_{FM}} \right]^2 = \frac{R_{AHE}}{\rho_{FM}} t_{FM} \frac{1}{\xi_{FM}^2} \tag{4.5}$$

It is worth to note that the factor in square brackets is the reciprocal of the shunting factor of the FM layer due to the presence of NM one, ξ_{FM}. Thus is, the ratio of the current flowing in FM over the total current injected in the bilayer is $\xi_{FM}=I_{FM}/I$.

We can then use the last equation to compute the Hall angle in our W/CoTb bilayers. The results are given in Figs. 4.6 (d). We can see that the Hall angle of CoTb increases when Co-composition increases. And those values are smaller than values reported for thick CoTb, 500 nm, about 2% (ref. 19).

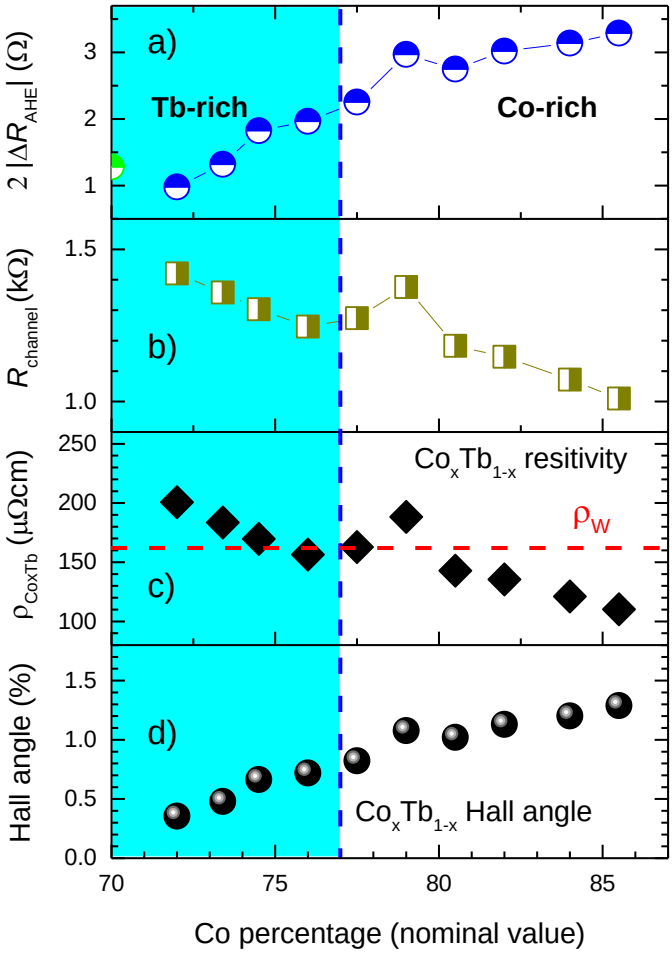

Figure 4.6: *Si-SiO₂//W(3)/Co_xTb_{1-x} (3.5) /Al(3): The change of Hall resistance amplitude $|\Delta R_{AHE}|$ (a), channel resistance $R_{channel}$ (b), Co_xTb_{1-x} resistivity (c), and Hall angle of CoTb as a function of the Cobalt concentration at room temperature. The vertical blue dashed line points correspond to the magnetic compensation point at room temperature. The horizontal red dashed line shows the value of W resistivity (ρ_W). The length and width of the longitudinal channel are L= 100 μm and width W= μm.*

4.3 Current - induced spin orbit torque switching

This section discusses the results of current - induced magnetization switching study by transport measurements. We performed experiments for all samples $0.72 \leq x \leq 0.86$ using a Keithley 6221 source coupled with a Keithley K2182 nano-voltmeter as described in Chapter II.

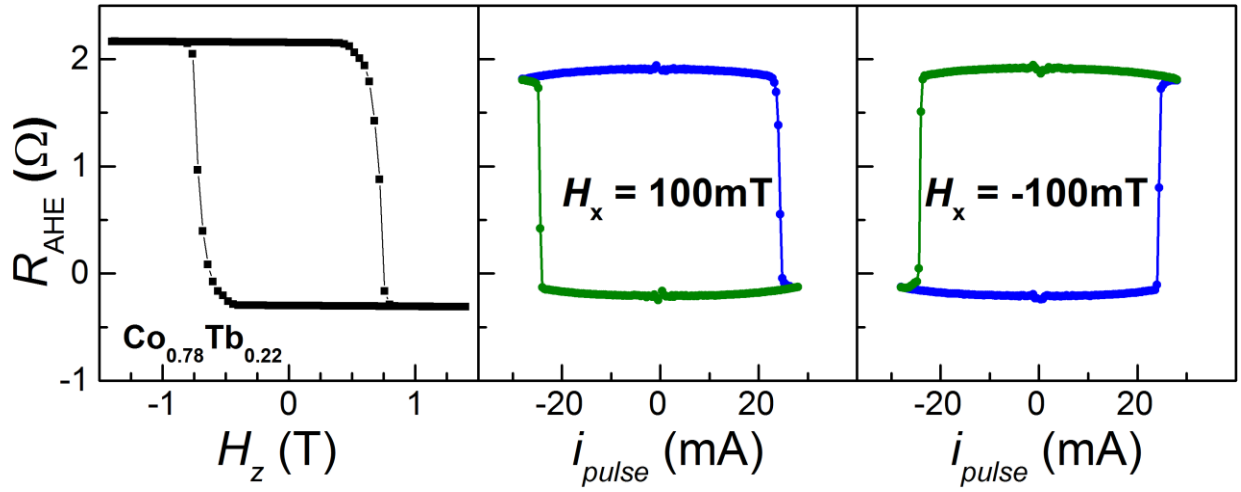

Figure 4.7: *(a) Field - induced magnetization switching, measured with AHE, $R_{AHE}(H_z)$ cycle and (b),(c) current-induced magnetization switching using ($H_x = \pm 100mT$) for sample Si-SiO_2//W(3)/$Co_{0.78}Tb_{0.22}$(3.5)/Al(3). This is a Co-rich sample at room temperature, close to the compensation point.*

For the sake of clarity, I will first describe typical results of the experiment on sample $W/Co_{0.78}Tb_{0.22}/AlOx$, which is Co-rich and close to the compensation point. Figure 4.7 (b)(c) show current - induced switching curves for this sample with an in-plane bias field of $H_x = 100mT$ and $-100mT$.

In this paticular measurement, we injected a series of pulse currents with different intensities between -30mA to +30mA into the system. The pulsed current duration was 100 μs. The Hall voltage is measured during the pulse. As described in Figure 4.7 (b) (for $H_x > 0$), at first when current is sweeping between -30mA to 23mA, the Hall resistance R_{AHE} remains the same, then the value of R_{AHE} suddenly drops to a new value, indicating a new magnetic state of the sample. When we injected the current in opposite direction, R_{AHE} remains at 2nd state until current reach -24mA, at which R_{AHE} jump back to the initial value. These "sudden jumps" of

R_{AHE} is the evidence of the magnetization switching. In this case the critical switching current is 24mA.

Fig. 4.7 (a) shows field-induced switching cycle $R_{AHE}(H_z)$ obtained at room temperature with a low in-plane dc current of 400 μA (charge current density of about 2.4 10^9A/m^2 flowing in each layer) for sample $W/Co_{0.78}Tb_{0.22}/AlOx$. Comparing Figure 4.7(b)(c) with the cycle in Figure 4.7(a), we observed that the amplitude of R_{AHE} is almost the same, indicating the full reversal is achieved. Actually, the amplitude of the current-induced switching cycle is a bit smaller than that obtained for field induced switching. The reason for that is for current-induced switching we used 100μs pulse with high intensity that brings much more thermal effect than in field switching experiment where we used only 400 μA DC current. So even though the experiment was performed at room temperature, the real temperature on the sample during the measurement is higher and ΔR_{AHE} has a trend to be smaller with higher T.

It should be noted that the in-plane field H_x play a role in the switching. Comparing Figure 4.7(b) and (c) we observe that the switching polarity changes sign while changing the sign of H_x. The role of the in-plane field can be understood as the field to overcome the DMI effective field thus allowing domain walls propagation and consequently the magnetization switching to happen [3,4]. This may be also understood within a macrospin model: the equilibrium position of the magnetization is either along +z or –z, but if we add an in-plane field H_x, then we break this symmetry favoring the *jump* from one position to another under a given direction of injected current. If the SOT depends on the Co moment, the SOT acts as an effective field $\boldsymbol{H}_{\mathbf{SHE}} \propto \boldsymbol{m}\times\boldsymbol{\sigma}$ [20,21] where $\boldsymbol{m}$ is the magnetic moment and $\boldsymbol{\sigma}$ the spin polarization of the spin current injected into the CoTb layer. $\boldsymbol{\sigma}$ is perpendicular to the current direction (in the same plane of the sample), and it has opposite signs when the direction of the current is inverted. $\boldsymbol{m}$ changes its sign upon the change of the in-plane field direction. Thus the sign of the Hall cycle is reversed when H_x is reversed as observed in Fig 4.7 (b)(c).

We observed current induced magnetization switching in all samples for $0.72 \leq x \leq 0.86$. The data of the full series are shown in Fig. 4.8. Interestingly, a full magnetization reversal is obtained even for an in-plane field H_x as low as 2 mT. This is a promising property of the system since reducing the use of external magnetic field in switching is one of the requirements for low power consumption applications.

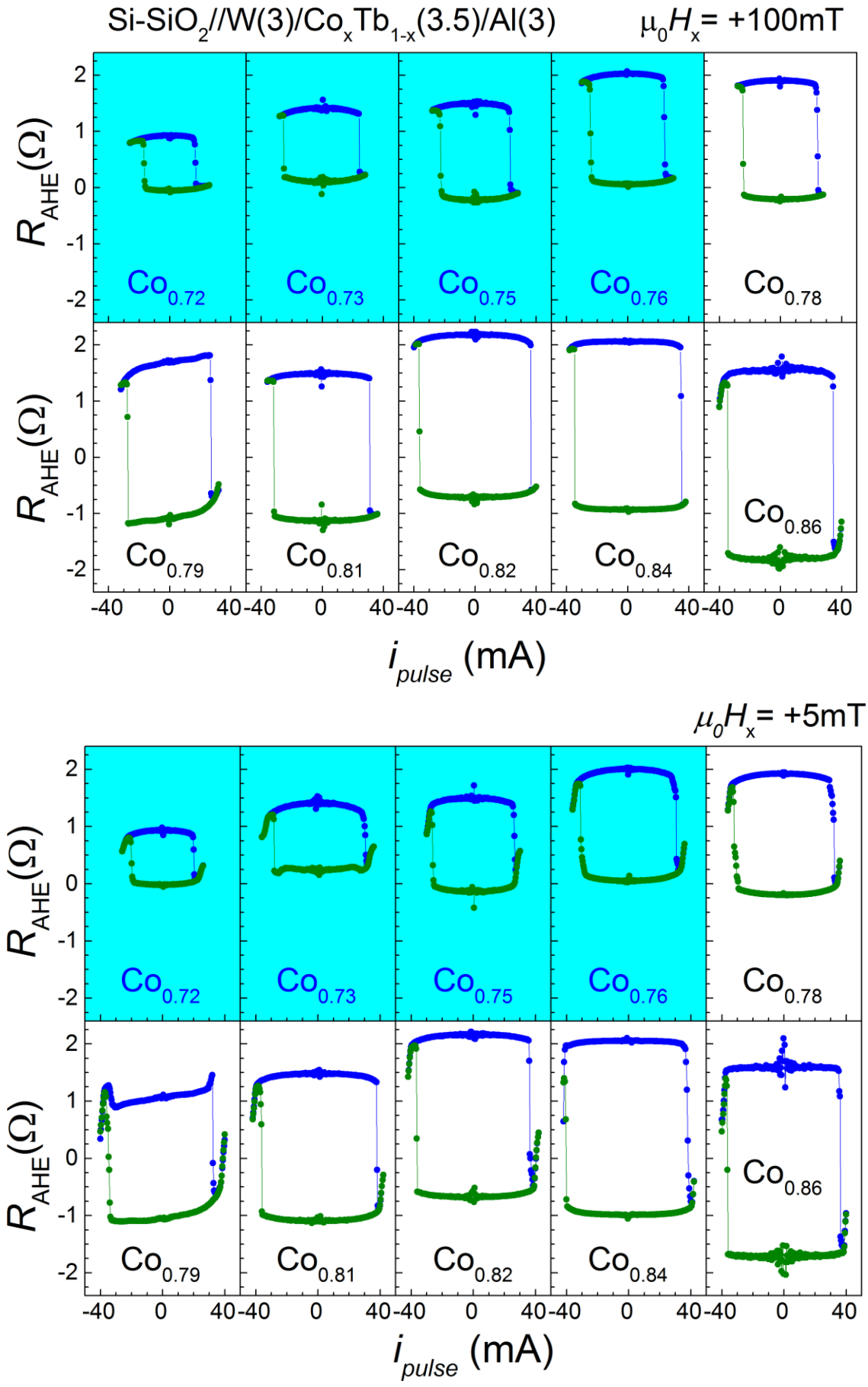

Figure 4.8: *Current-induced magnetization switching (H_x=100mT and H_x=5mT)*

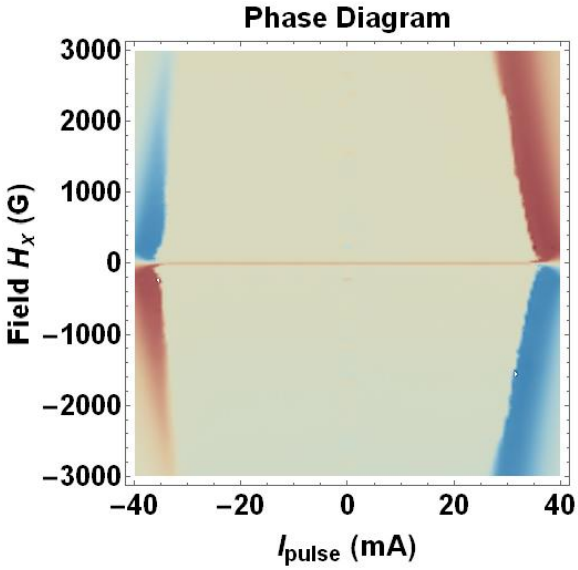

Figure 4.9: *2D-plot of current–switching cycles performed at room temperature on Si-SiO$_2$//W (3 nm)/Co$_{0.86}$Tb$_{0.14}$ (3.5 nm)/AlOx(3 nm). The R(I_{pulse}, H_x) cycles were carried out with different fields between –3 kG and +3 kG. The red (blue) color region stand for Up (Down) magnetic configuration.*

In order to examine the role of in-plane field H_x on the switching, we measured a series of current-switching cycles on one sample at different in-plane fields ranging from 0 to 300mT. Figure 4.9 shows a typical result that performed on sample W/Co$_{0.86}$Tb$_{0.14}$/Al. This diagram is obtained by analyzing collected data using Mathematica. The red (blue) color corresponds to Up (Down) magnetic configuration. The boundary between color region and white region marks the critical current for switching. As shown in figure 4.9, in our study range, the higher the in-plane field, the lower the current needed to obtain switching. This result confirms the role of in-plane field in supporting the switching, in agreement with the equation developed in chapter 3: $J_{sw} \approx \frac{2e}{\hbar}\frac{t}{\theta_{SH}^{eff}}\left(K_{eff} - \frac{\mu_0 H_x M}{\sqrt{2}}\right)$.

In ferrimagnetic alloys, the effective field H_{SHE} can be reversed if the compositions changes from Co-rich sample to Tb-rich one. Thus one might expect that at room temperature the switching polarity of Co-rich sample and Tb-rich sample should be opposite (in a similar way as it changes when we change the sign of the in-plane H_x). The fact that our experiment shows identical switching polarity of Co-rich and Tb-rich samples (figure 4.7, for same sign of H_x) is worth the attention. This contradiction behaviour can be attributed to the Joule heating effect during the measurement. Even though the experiments were performed at room temperature, the large amount of heat during the current injection increases the real sample temperature, making the so-called Tb-rich sample cross the magnetic compensation

temperature to become Co-rich. This leads to the change of the switching polarity. That makes all samples have Co-rich switching polarity, explaining why there was no diffence of switching polarity between samples as expected.

In order to confirm the above assumption of high contribution of thermal effect on the change of switching polarity, we measured $R_{AHE}(H_z)$ cycles for different applied current pulses on the "Tb-rich" sample $W/Co_{0.76}Tb_{0.24}/AlOx$ shown in Figure 4.10.

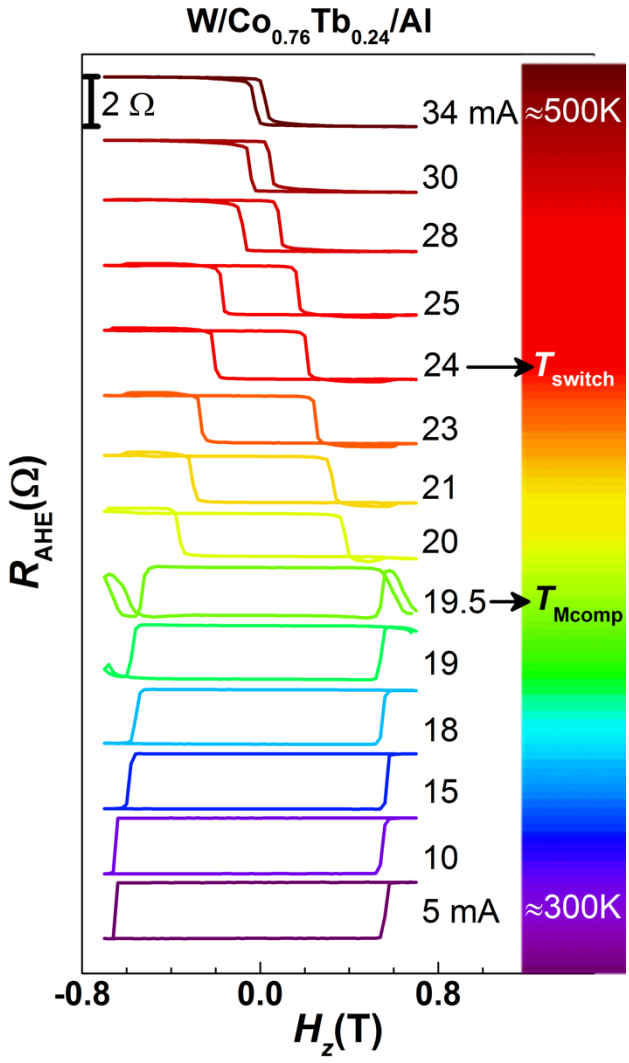

Figure 4.10. *$R_{AHE}(H_z, i_{pulse})$ cycles for Hall bar measured at room temperature.*

In this experiment, we performed field-induced switching measurements, using pulsed current with pulse duration of 100 µs (the same as in current-induced experiment). The cycle is measured with different current intensity from 5mA up to 34mA. As shown in Figure 4.10, the

$R_{AHE}(H_z)$ cycle has the expected sign for Tb-rich sample when current $i < 19.5$ mA. However, the sign of the cycle is reversed when crossing the point i ~ 19.5mA, then showing a "Co-rich"-like polarity for $i > 19.5$ mA. This indicates that for current close to 19.5 mA, the real temperature of the device is close to the sample compensation temperature (T_{Mcomp} ~320 K). This experiment is a clear evidence that the sample is strongly heated during the current-induced switching experiment and thus the thermal effect is responsible for the change of the switching polarity in our case.

In Figure 4.10, we use a color code that illustrates the increase of temperature on the device, corresponding to increasing current intensity. The temperature can be estimated from the resistance value of the Hall channel as will be explained in section 4.4. In this particular sample, the critical current for magnetization reversal is 24mA where the sample temperature is 460K, which is higher than the compensation temperature (T_{Mcomp} ~320 K). The current-induced switching happens at the temperature above T_{Mcomp}, that explains why the sign of the R_{AHE}(i) cycle is opposite to the expected sign for Tb-rich sample. It should be noted that at the switching, the sample temperature is higher than T_{Mcomp} and smaller than Curie temperature. It is shown in Figure 4.10 that even with intensity current pulse as high as 34 mA (~525 K), the device still show a ferromagnetic hysteresis loop and remain perpendicular. T_C is then higher than 525 K.

4.4 Characteristic temperatures of switching

In section 4.3, I pointed out the role of temperature on the switching polarity of the samples. The large amount of heat contributed to the system rises some more questions: How much does the device heat when the switching occurs? How does the system behave when performing the current-induced switching experiment at different temperature? How does the composition of the CoTb alloy affect the temperature enhancement of the system? In order to address these questions, we performed a series of temperature-dependent experiments for all the samples.

For each sample with a particular composition, we performed transport measurements at different cryostat temperature between 10K to 350K. For clarity, we use the term "cryostat temperature" for the initial temperature of the measurement set-up, in order to distinguish it from the "sample temperature" which is the real temperature of the device during measurement due to Joule heating effect.

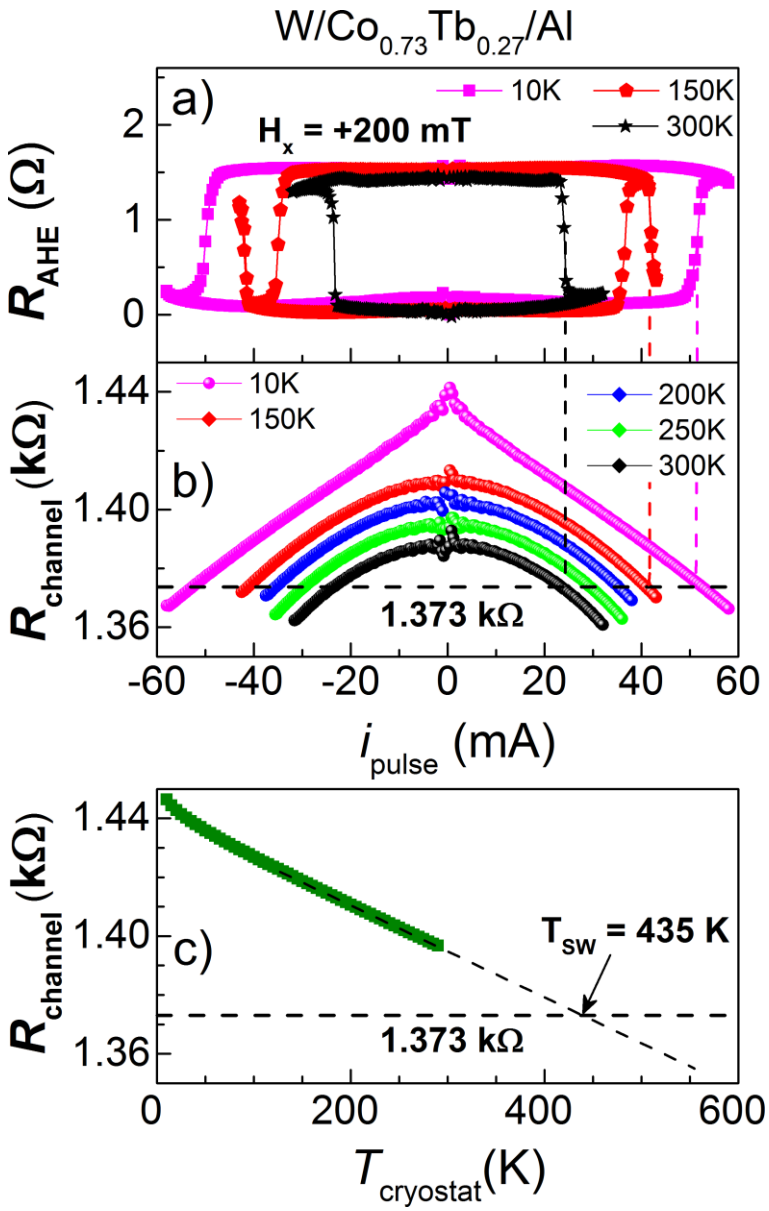

Figure 4.11: *(a) $R_{AHE}(i_{pulse})$ cycles for x=0.73. at different cryostat temperatures. (b) $R_{channel}(i_{pulse})$ and $R_{channel}(T)$ at different cryostat temperatures. It it observed that the device always reaches the same value of longitudinal resistance (1373Ω), which means it reach the same temperature. Such a temperature is defined as T_{switch}. In this case T_{switch} ~ 435K*

Fig. 4.11(a) shows the $R_{AHE}(i_{pulse})$ cycles for $H_x>0$ at different cryostat temperature for $W/Co_{0.73}Tb_{0.27}$ (Tb-rich at room temperature). At 300 K a Down-Up current-switching polarity is observed. For 150 K≤ $T_{cryostat}$ ≤ 250 K a double current switching loop is observed. This type of double current switching can be explained when the switching temperature is close to T_{Mcomp} and its origin will be discussed later. For 10 K ≤ T ≤100 K we observe only Down-Up current-switching polarity (we didn't increase too much the pulse current to avoid burning the device).

One can calibrate the real sample temperature for different pulse-current values performing the following protocol:

i) measuring the resistance of the current channel $R_{channel}(i_{pulse})$ as function of pulse current intensity as shown in Fig. 4.11(b) for different cryostat temperatures, and

ii) ii) measuring the temperature dependence of the current channel $R_{channel}(T)$ as shown in Fig 4.11c) (for which we use a very low DC bias current of only 400 μA).

Interestingly, we observe that for Co-rich current-switching polarity (Down-Up) the device reaches the same resistance (1.373 kΩ) and consequently the same switching temperature T_{switch} = 435 K ± 25 K for this W/$Co_{0.73}Tb_{0.27}$. We note that the resistance decreases when T increases (in opposite way as expected in metals), which is a feature and confirmation of amorphous materials [22].

We have performed the same protocol for various compositions and different devices. An example for Co-rich sample at room temperature is shown in Fig. 4.12 (W/$Co_{0.79}Tb_{0.21}$). Here we also observe that the critical current heats up the device to the same channel resistance (Fig. 4.12c), that means the device reachs the same T_{switch} (~485 K for this Co_xTb_{1-x} sample) irrespective of the initial cryostat temperature. Moreover, on this particular sample T_{Mcomp} is about 200 K and we observe no change of current switching polarity even for T as low as 10 K which is well below its T_{Mcomp}.

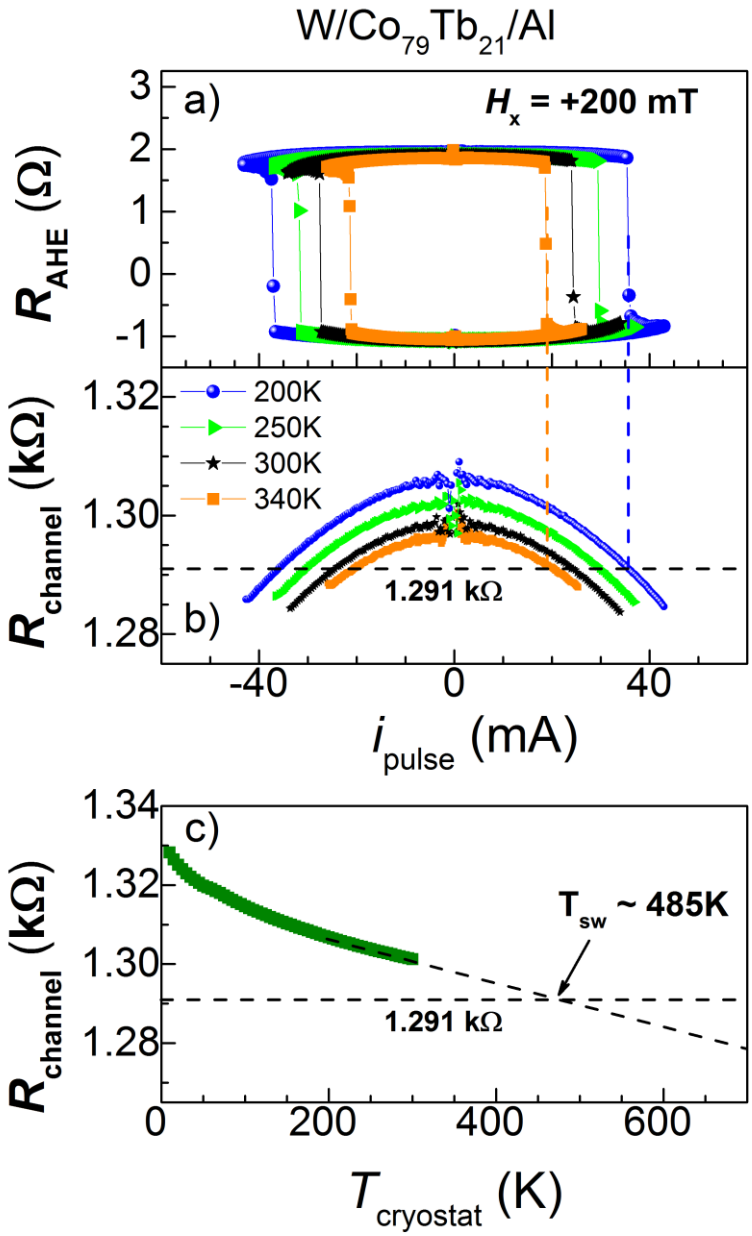

Figure 4.12: *(a)$R_{AHE}(i_{pulse})$ cycles for x=0.79. at different cryostat temperatures. (b) $R_{channel}(i_{pulse})$ and $R_{channel}(T)$ at different cryostat temperatures. For the sake of clarity we show only four different temperatures in (a) and (b). In (c) a small dc current, 400 uA, is used and we can neglect Joule heating effect.*

Additionally to the characteristic T_{switch} we have just discussed, one can also investigate the temperature dependence of the critical current as shown in Fig. 4.13(a) for a $Co_{0.79}Tb_{0.21}$ sample (Co-rich at room temperature). The extrapolation of the linear dependence to zero current is defined as T*. In Fig. 4.13(b) is found out that T*~490 K for W/ $Co_{0.79}Tb_{0.21}$ which is close to T_{switch} for the same composition.

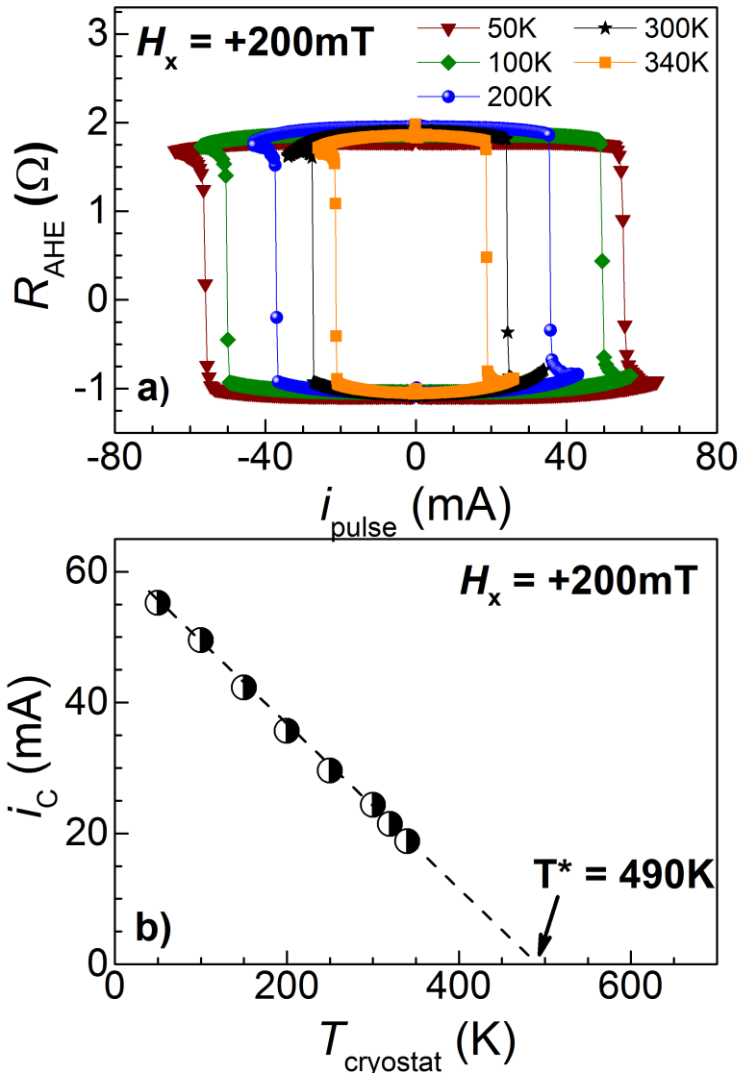

Figure 4.13: *(a) $R_{AHE}(i_{pulse})$ at different cryostat temperature. Cycles for x = 0.79. (b) The critical current to reverse M increases linearly when T decreases. The extrapolation of the linear behaviour for zero current is defined as T*.*

Another feature that is usually observed in these experiments is that we need to increase the critical current when we decrease the cryogenic or initial temperature. This agrees well with the expression for FM materials as well as for FiM, ($J_{sw} \approx \frac{2e}{\hbar}\frac{t}{\theta_{SH}^{eff}}\left(K_{eff} - \frac{\mu_0 H_x M}{\sqrt{2}}\right)$). When we decrease T, the magnetization migh increase slowly. However the magnetic anisotropies increase much faster when T decreases. Even though we don't know the behaviour of CoTb alloys, it has been reported for Fe that $K(T) \propto (M(T)/M(0))^{10}$ [23]; and for magnetic oxides that $K(T) \propto (M(T)/M(0))^{3}$ [24]. As a consequence, from the equation, we can see that if the difference between Ke_{ff} and $\mathbf{H_x \times M}$ increases (which happens at low T), then J_{sw} increases. This

also explains why we need higher in-plane field H_x at low temperature to get the SOT-switching. This is not incompatible with the fact that we heat up our devices during the SOT-switching experiments, on the contratry it agrees well. Moreover, this also explains why we do need just a very small in-plane field to induce switching in these W/CoTb systems, despite their huge perpendicular magnetic anisotropy: because of the strong heating contribution, M might decrease slowly but K_{eff} decreases much faster. This is not the case for other systems where heating effect on FM or FiM layer is smaller. For example in Pt/CoTb much of the current flows in Pt layer which is an advantage to produce more spin current. However the actual temperature rises to lower values, and despite the fact that perperndicular anisotropy is lower than in W/CoTb, higher in-plane fields will be needed to get the SOT-switching. This again is explained by the dependence of J_{sw} on K_{eff} and $\mathbf{H_x \times M_s}$.

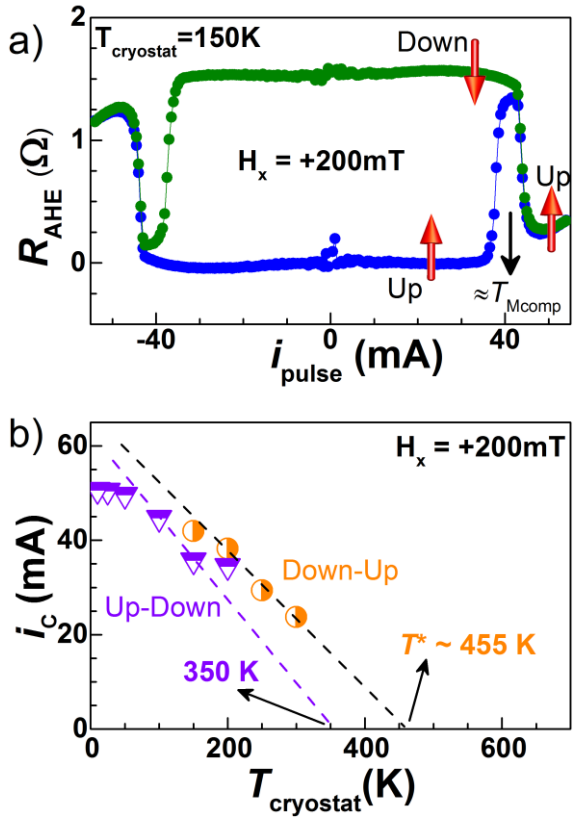

Figure 4.14: *a) $R_{AHE}(i_{pulse})$ at 150K for x=0.73 (Tb-rich at room temperature). There are two switchings: i) at lower current it agrees with a Tb-rich switching polarity (Up-Down). ii) The reversal with higher current agrees with a Co-rich switching polarity (Down-Up). b) Temperature dependence of the critical currents for this composition. T_{Mcomp} would be between 350 K and 455 K.*

Figure 4.14 shows $R_{AHE}(i_{pulse})$ for the $Co_{0.73}Tb_{0.27}$ sample performed for a cryostat temperature of 150 K to highlight the observation of the two switching events. At lower current (37.5 mA), i.e. lower Joule heating effects, we observe Up-Down current-induced switching polarity while the second one which occurs at higher current (43 mA) is Down-Up. This can be understood considering that to achieve the first switching the device reaches a temperature below its T_{Mcomp} so the sample is still Tb-rich and the Up-Down current-switching polarity observed is as expected. If we continue to increase the intensity of the applied in-plane current pulses we overcome T_{Mcomp} and then the perpendicular component of effective torque field $\mathbf{H_{SHE}}$ now changes its sign as discussed previously. Consequently, the second observed switching agrees well for Co-rich phase (Down-Up).

In Fig. 4.14(b) the temperature dependence of both switching currents is shown. As discussed, the first (second) switching is congruent with a Tb-rich (Co-rich) current-switching polarity and happens for $T<T_{Mcomp}$ ($T>T_{Mcomp}$). The linear extrapolation of both switching currents roughly tends to 350 K (Tb-rich switching) and T*~455 K (Co-rich switching). The value of T* seems to be slightly higher than T_{switch} (~435 K ± 25 K as determined in Fig 4.11c). We cannot discriminate whether T* is above or below T_{switch} due to limitations in the analysis. Thus we believe that our results open up new perspectives and motivate continued studies concerning these temperatures. So far T* and T_{switch} seem very similar. Nevertheless, the observation that the device always reaches the same temperature when the switching occurs, irrespective of the T_{cryo} even without the linear extrapolation, has significant implications on the functioning of these devices and we believe that future studies will have to consider SOT-switching experiments performed about T_{switch} or T*.

4.5 T-x switching phase diagram

In figure 4.15 the different characteristic temperatures of our W/CoTb systems can be plotted in the (T,x_{Co}) phase diagram. The determined T_{Mcomp} decreases linearly with the Co concentration as reported for bulk CoTb and thick CoGd films (300 nm) [10,25]. However T_{switch} and T* increase linearly with the Co-concentration and scale with the Curie temperature T_c thus depending on composition, and independent of initial temperature. It is remarkable that the T_{switch} and T* are nearly the same, indicating that, to achieve the switching, one has to reach a specific temperature. The three first questions formulated above are therefore answered.

These results may also encourage the study of other systems in which T_C could be tuned and very low critical currents may be obtained in case T_c is close to room temperature. Some examples of such a systems may be (Co/Pt) or (Co/Ni) multilayers or, even better, CoPt alloys.

Now let's discuss the physical meaning of these switching temperatures. It is clear that for Co current switching polarity, the temperature of switching is above T_{Mcomp} and below T_c. Figure 4.15(a) also shows T_c in bulk CoTb after Hansen *et al*. [10].

The angular compensation temperature, T_{Acomp}, scales with $T_{Mcomp.}$ (see section 4.2.3) Indeed, typically T_{Acomp} ~ (T_{Mcomp}+30 K) for $Co_{0.775}Gd_{0.225}$ thick films (300 nm) [25]. Therefore in Co_xTb_{1-x} we have seen that the trends of T_{Acomp} and T_{Mcomp} are similar and they decrease with increasing Co concentration (Figure 4.4) [13-18]. However T_{switch} increases with Co concentration which indicates that T_{switch} is not scaling with T_{Acomp} or T_{Mcomp} but with T_C. For sake of comparison in Figure 4.15(b) we plotted the switching-current for the experiment performed at room temperature together with the temperature increase $\Delta T = T_{switch} - T_{cryostat}$, due to Joule heating effect. We can observe that the temperature is increased between 100 K and 300 K. This variation will increase when we reduce $T_{cryostat}$.

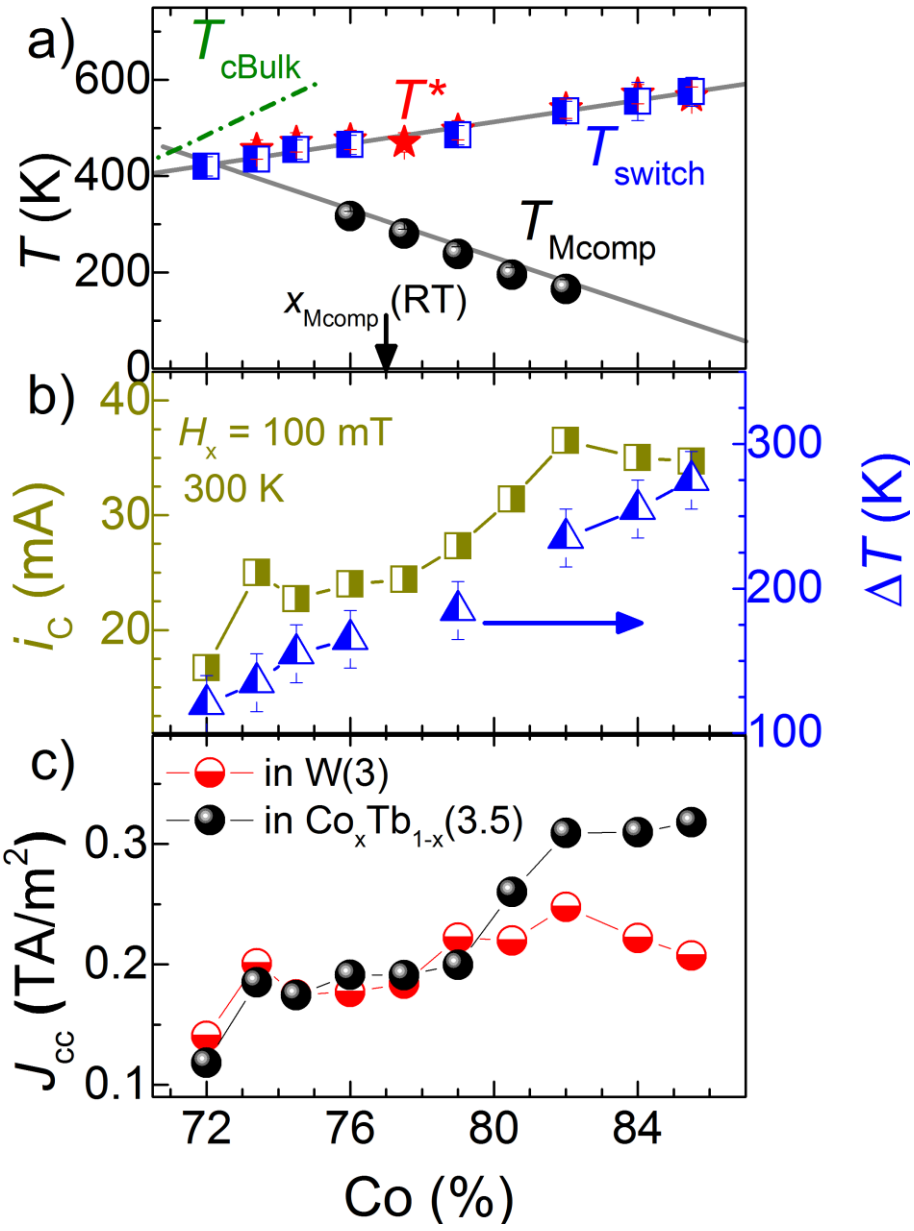

Figure 4.15: *(a) Characteristic temperature as function of Co concentration: T*, T_{switch} and T_{Mcomp}. (b) The critical current for switching when performing experiment at room temperature and the variation of temperature T_{switch} - $T_{cryostat}$. (c) The critical current density, calculated from (b), flowing in W and CoTb layers, respectively.*

Considering that the resistivity of Co_xTb_{1-x} and W layers change similarly with temperature and using the resistivity measured at room temperature, we can estimate the critical current density J_{CC} flowing on each layer, as displayed in Fig. 4.15c.

We observe that:

- J_{cc} on W is reduced by a factor of ~2 while varying the composition of CoTb.

- We observe the minimum of J_{cc} at the lower measured Co concentration. This can be explained by the fact that T_C and T_{switch} decrease with decreasing the Co-concentration.
- Furthermore, the switching temperature may be understood from thermally-excited magnon accumulation in ferrimagnets, which vanishes when $\partial m/\partial T=0$ as explained by Ritzmann et al. [26] Thus T_{switch} would be the critical temperature at which the magnon accumulation signal vanishes, but this correlation needs additional studies.

Concerning the last point, it is not so simple to measure M(T) experimentally in FiM and even more complicated in just 3.5 nm due to the very weak magnetic signal. Nevertheless, it should be tried in future works.

4.6 Conclusions

In this chapter we have fully characterized current-induced switching experiments in a series of //W(3nm)/Co_xTb_{1-x}(3.5nm)/AlO_x(3nm) samples. In addition to the SOT effect we demonstrate a strong thermal contribution to achieve the magnetization reversal.

- For the Co-rich current-switching polarity the device needs to reach the same temperature T_{switch} to achieve the switching.
- This T_{switch} increases with Co-concentration which then scales with Curie temperature T_c. It is then unlikely that T_{switch} corresponds to angular momentum compensation temperature (which scales with T_{Mcomp} decreasing with Co-concentration).
- These results highlight the importance of considering thermal contributions in SOT switching experiments and the fact that the spin Hall angle determination might be overestimated when thermal contributions are neglected.
- The use of resistive W layer increases the heating of the device, reducing strongly the external in-plane needed to assist the SOT (which is not the case for Pt/CoTb samples).
- These results are important for the full understanding of current-induced magnetization switching and may lead the way to new technological applications taking advantage of the rather strong heating waste in devices.

- It turned out that the W/CoTb system is a very robust one. The SOT-switching is very reversible despite the strong heating contribution. This could also lead to applications in harsh environments.
- There is also room to reduce strongly the current density considering the beta phase of W.

References

[1] I. M. Miron, K. Garello, G. Gaudin, P.-J. Zermatten, M. V Costache, S. Auffret, S. Bandiera, B. Rodmacq, A. Schuhl, and P. Gambardella, “Perpendicular switching of a single ferromagnetic layer induced by in-plane current injection.” Nature **476**, 189 (2011).

[2] L. Liu, O. J. Lee, T. J. Gudmundsen, D. C. Ralph, and R. a. Buhrman, “Current-induced switching of perpendicularly magnetized magnetic layers using spin torque from the spin hall effect” Phys. Rev. Lett. **109**, 096602 (2012).

[3] J. C. Rojas-Sánchez, P. Laczkowski, J. Sampaio, S. Collin, K. Bouzehouane, N. Reyren, H. Jaffrès, A. Mougin, and J. M. George, “Perpendicular magnetization reversal in Pt/$[Co/Ni]_3$/Al multilayers via the spin Hall effect of Pt” Appl. Phys. Lett. **108**, 082406 (2016).

[4] K.-S. Lee, S.-W. Lee, B.-C. Min, and K.-J. Lee, “Threshold current for switching of a perpendicular magnetic layer induced by spin Hall effect” Appl. Phys. Lett. **102**, 112410 (2013).

[5] S. Mangin, T. Hauet, P. Fischer, D. H. Kim, J. B. Kortright, K. Chesnel, E. Arenholz, and E. E. Fullerton, “Influence of interface exchange coupling in perpendicular anisotropy $[Pt/Co]_{50}$/TbFe bilayers” Phys. Rev. B **78**, 024424 (2008).

[6] C. D. Stanciu, A. V. Kimel, F. Hansteen, A. Tsukamoto, A. Itoh, A. Kirilyuk, and Th. Rasing, “Ultrafast spin dynamics across compensation points in ferrimagnetic GdFeCo: The role of angular momentum compensation”, Phys. Rev. B **73**(22), 220402(R) (2006).

[7] X. Jiang, L. Gao, J. Z. Sun, and S. S. P. Parkin, “Temperature dependence of current-induced magnetization switching in spin valves with a ferrimagnetic CoGd free layer”, Phys. Rev. Lett. **97**(21), 217202 (2006).

[8] D. Bang, J. Yu, X. Qiu, Y. Wang, H. Awano, A. Manchon, and H. Yang, “Enhancement of spin Hall effect induced torques for current-driven magnetic domain wall motion: Inner interface effect”, Phys. Rev. B **93**(17), 174424 (2016).

[9] Thai Ha Pham, S.-G. Je, P. Vallobra, T. Fache, D. Lacour, G. Malinowski, M.C. Cyrille, G. Gaudin, O. Boulle, M. Hehn, J.-C Rojas-Sánchez, and S. Mangin, "Thermal Contribution to the Spin-Orbit Torque in Metallic-Ferrimagnetic Systems" Physical Review Applied **9**, no. 6, 064032 (2018).

[10] P. Hansen, C. Clausen, G. Much, M. Rosenkranz, and K. Witter, “Magnetic and magneto-optical properties of rare-earth transition-metal alloys containing Gd, Tb, Fe, Co”, J. Appl. Phys. **66**, 756 (1989).

[11] S. Alebrand, U. Bierbrauer, M. Hehn, M. Gottwald, O. Schmitt, D. Steil, E. E. Fullerton, S. Mangin, M. Cinchetti, and M. Aeschlimann, “Subpicosecond magnetization dynamics in TbCo alloys” Phys. Rev. B **89**, 144404 (2014).

[12] M. Gottwald, M. Hehn, F. Montaigne, D. Lacour, G. Lengaigne, S. Suire, and S. Mangin, “Magnetoresistive effects in perpendicularly magnetized Tb-Co alloy based thin films and spin valves” J. Appl. Phys. **111**, 083904 (2012).

[13] Y. Hirata, D. Kim, T. Okuno, T. Nishimura, D. Kim, Y. Futakawa, H. Yoshikawa, A. Tsukamoto, K.-J. Kim, S.-B. Choe, and T. Ono, “Correlation between Compensation Temperatures of Magnetization and Angular Momentum in GdFeCo Ferrimagnets” Physical Review B, **97**(22), 220403 (2018).

[14] B. D. Cullity, C. D. Graham, Introduction to Magnetic Material (John Wiley & Sons, Inc., Hoboken, New Jersey, 2009) 2nd ed.

[15] W. E. Henry, “Saturation Magnetization and Ferromagnetic Interaction in Terbium Metal” J. Appl. Phys. **30**, S99 (1959).

[16] P. de V. du Plessis, C. F. van Doorn, and D. C. van Delden, “Critical behaviour of helical ordered Dysprosium and Terbium” J. Magn. Magn. Mater. **40**, 91 (1983).

[17] L. Onsager, “A two-dimensional model with an order-disorder transition” Phys. Rev. **65**, 117 (1944).

[18] S. T. Bramwell and P. C. W. Holdsworth, “Magnetization and universal sub-critical behaviour in two-dimensional XY magnets” J. Phys. Condens. Matter **5**, L53 (1993).

[19] W. Kim and R. J. Gambino, J. Appl. Phys. 87, 1869 (2000).

[20] A. Thiaville, S. Rohart, É. Jué, V. Cros, and A. Fert, “Dynamics of Dzyaloshinskii domain walls in ultrathin magnetic films” EPL (Europhysics Lett. **100**, 57002 (2012).

[21] A. V. Khvalkovskiy, V. Cros, D. Apalkov, V. Nikitin, M. Krounbi, K. a. Zvezdin, A. Anane, J. Grollier, and A. Fert, “Matching domain-wall configuration and spin-orbit torques for efficient domain-wall motion” Phys. Rev. B **87**, 020402 (2013).

[22] A. Fert and R. Asomoza, “Transport properties of magnetic amorphous alloys Transport properties of magnetic amorphous alloys” J. Appl. Phys. **50**, 1886 (1979).

[23] C. Zener, “Classical theory of the temperature dependence of magnetic anisotropy energy”, Physical Review, 96(5), 1335 (1954).

[24] Belmeguenai *et al.*, “Temperature dependence of magnetic properties of $La_{0.7}Sr_{0.3}$ MnO_3/$SrTiO_3$ thin films on silicon substrates”, Physical Review B 81(5), 054410 (2010).

[25] M. Binder, a. Weber, O. Mosendz, G. Woltersdorf, M. Izquierdo, I. Neudecker, J. Dahn, T. Hatchard, J.-U. Thiele, C. Back, and M. Scheinfein, “Magnetization dynamics of the ferrimagnet CoGd near the compensation of magnetization and angular momentum” Phys. Rev. B **74**, 134404 (2006).

[26] U. Ritzmann, D. Hinzke, and U. Nowak, “Thermally induced magnon accumulation in two-sublattice magnets” Phys. Rev. B **95**, 054411 (2017).

Conclusions

This work provides some new insights into the SOT - induced switching phenomena in both practical and theoretical terms.

A series of RE-TM ferrimagnetic Co_xTb_{1-x} alloys in contact with a heavy metal W layer with wide range of compositions were successfully made by DC magnetron sputtering. All samples show perpendicular magnetic anisotropy. We have fully characterized current-induced switching experiments in all different compositions samples at a large scale of temperature ranging from 10K to 350K. The SOT induced switching is achieved in all samples. Even for sample close to compensation point, the switching is obtained by a moderate current density (~ 10^{11} A/m^2) despite very large coercive field, suggesting a promising characteristic for memory applications.

We observed no reduction of switching current density at the magnetic compensation point. A simple model based on antiferromagnetically coupled LLG equations is developed to explained these experimental results. We pointed out that the switching current density scales with the effective anisotropy, which is not minimum at the magnetic compensation point. We also note that conventional SOT effective field measurement cannot resolve the debate of whether the spin currents are absorbed into one particular magnetization sublattice or into the net magnetization.

In addition to the SOT effect, we explore a strong thermal contribution in the magnetization reversal process. In our particular system where the resistivities of ferrimagnetic layer and W layer are at the same order of magnitude, which leads to strong heating on the devices, we demonstrated that each sample with a certain composition need to reach a certain temperature T_{switch} to achieve the switching. This T_{switch} increases with Co concentration which then scales with Curie temperature T_c. These results highlight the importance of considering thermal contributions in SOT as one of research perspective to understand current - induced magnetization switching. We note that the W/CoTb system is a robust system in which the SOT switching is consistently reproducible despite the strong heating contribution. This may lead the way to new applications taking advantage of rather strong heating waste in devices and also applications in harsh environments.

Overall, W/CoTb/AlOx is an attractive model system to get insights into the SOT related phenonmena. There is also room for further investigation on this system. For example, the current density could be reduced considering the beta phase of W. Also, it will be worth

implementing the current induced switching experiments using wide range of pulses widths from nanoseconds to miliseconds in order to fully understand the role of temperature in the switching process. Another interesting research direction would be to combine the all optical switching (AOS) and spin orbit torque switching on ferrimagnetic based system. Indeed, we have started some first experiments of the spin orbit torque under the influence of laser. So far, we observed the clearly reduction of the critical current density for SOT switching with support of laser, probably due to the heating effect. A lot more systematic work would be required to enable the potential of AOS - SOT combination.

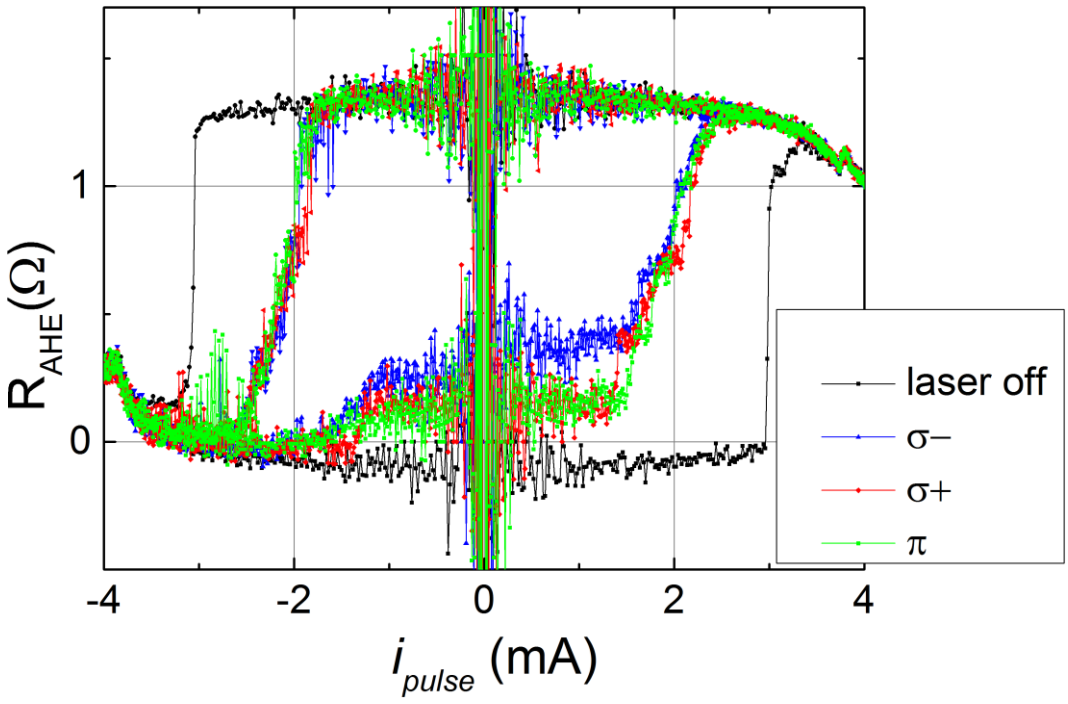

Figure 5.1: First observation of the SOT - induced magnetization switching under the influence of laser. Sample: Si-SiO_2/W(3)/$Co_{76}Tb_{24}$(3.5)/Al(3). The black curve is the reference - the original SOT switching (laser off). The blue/red/green curve represents the SOT switching under the influence of laser with polarization σ-/σ+/π, respectively.

Résumé en Français

Un fort intérêt se porte actuellement sur l'influence du couplage spin-orbite sur les propriétés de transport. Notamment la possibilité de retourner l'aimantation grâce au couple spin-orbite (SOT).
Afin d'envisager l'utilisation du SOT pour des applications dans le domaine de l'électronique de spin il est nécessaire de réduire le courant critique nécessaire au retournement et diminuer ou éliminer le champ magnétique externe planaire appliqué. Mon travail de thèse concerne l'étude expérimentale de systèmes bicouches métaux lourds/ ferrimagnétique (W/ Co_xTb_{1-x} ou Pt / Co_xTb_{1-x}). Dans les alliages ferrimagnétiques, l'aimantation du sous réseau du Cobalt est couplé antiparallelement à l'aimantation du sous réseau de Terbium. Ces alliages sont particulièrement intéressantes car pour une certaine concentration, il existe une température pour laquelle l'aimantation des deux sous réseaux sont égales et donc que l'aimantation résultante est nulle. Dans un premier temps j'ai caractérisé ces systèmes par magnétométrie et par mesures de résistance Hall anomale pour des températures allant de 10 à 350 K. Les expériences de renversement d'aimantation induite par le courant ont été effectuées dans une géométrie « couple Spin-orbite » (SOT) où les impulsions de courant sont injectées dans le plan et le retournement de l'aimantation est détectée par la mesure de la résistance de Hall. Le retournement complet de l'aimantation a été observée dans tous les échantillons. Le courant de retournement varie de façon continue avec la composition de l'alliage et nous n'avons pas observé une réduction de celui-ci au point de compensation malgré la forte augmentation de l'efficacité du SOT. Un modèle basé sur les équations de Landau-Lifschitz-Gilbert couplées montre que la densité du courant de retournement est proportionnelle à l'anisotropie perpendiculaire effective, qui ne diminue pas au point de compensation. Bien que le TbCo possède une forte anisotropie magnétique perpendiculaire, le retournement se produit pour un champ magnétique planaire faible. Nous avons pu montrer que le chauffage provoqué par le courant joue un rôle important. En effet le retournement semble se produire à une température de commutation caractéristique T_{switch} induite par le chauffage Joule qui est supérieure aux températures de compensation magnétique et angulaire mais inférieure à sa température de Curie (T_C). Tout se passe comme s'il fallait atteindre une température proche de T_C pour que le retournement ait lieu.

Summary in English

The influence of spin-orbit coupling on transport properties has been a topic of strong and growing interest in the last ten years .
In order to use of spin-orbit torque for applications in the field of spin electronics, it is necessary to reduce the critical current necessary for the reversal and to decrease or eliminate the planar external magnetic field applied. My thesis work concerns the experimental study of heavy metal / ferrimagnetic bilayer model systems (W / Co_xTb_{1-x} or Pt / Co_xTb_{1-x}). In such ferrimagnetic alloys, the magnetization of the Cobalt sub-lattice is coupled antiparallel to the magnetization of the Terbium sub-lattice. These alloys are particularly interesting because for certain concentration, there is a temperature for which the magnetization of the two sub-networks are equal resulting in zero magnetization. This is the magnetization compensation temperature. At first I characterized these systems using magnetometry and Hall cross measurements for temperatures ranging from 10 to 350 K. The experiments of magnetization reversal of magnetization induced by the current were carried out in a "Spin- orbit torque" (SOT) geometry where the current pulses are injected into the plane and the reversal of the magnetization is detected by measuring the Hall resistance. The complete magnetization reversal was observed in all the samples. The current reversal was found to vary continuously with the alloy composition and we did not observe any reduction at the compensation point despite the large increase in the SOT efficiency. A model based on the coupled Landau-Lifschitz-Gilbert equations shows that the reversal current density is proportional to the effective perpendicular anisotropy, which does not decrease at the compensation point.
Although TbCo has a strong perpendicular magnetic anisotropy, the reversal occurs for a weak planar magnetic field. We were able to show that the heating caused by the current plays an important role in the switching. Indeed the reversal seems to occur at a characteristic switching temperature (T_{switch}) induced by Joule heating. T_{switch} is larger than the magnetic and angular compensation temperatures, but lower than the Curie temperature. Everything happens as if it was necessary to reach a temperature close to the order temperature for the reversal to take place.